

PRODUCTION OF NUCLEI NEAR THE NEUTRON  
DRIP-LINE BY PROJECTILE FRAGMENTATION

By

Elaine Kwan

A DISSERTATION

Submitted to  
Michigan State University  
in partial fulfillment of the requirements  
for the degree of

DOCTOR OF PHILOSOPHY

Department of Physics and Astronomy

2006

## ABSTRACT

### PRODUCTION OF NUCLEI NEAR THE NEUTRON DRIP-LINE BY PROJECTILE FRAGMENTATION

By

Elaine Kwan

One of the most fundamental questions in nuclear physics is related to the existence of nuclei. Nuclei at the limits of the neutron (or proton) drip-line can no longer bind additional neutrons (or protons) and may have very different physical and structural properties compared to nuclei near stability. The neutron drip-line is experimentally known up to oxygen ( $Z=8$ ). The discovery of  $^{31}\text{F}$  extended the boundaries of existence in this region by an additional six neutrons. This large increase in the number of bound neutrons with the addition of a single proton is not seen anywhere else in the chart of nuclides. Many theoretical models make different predictions of the exact locations of the neutron drip-line in this region. Most of these models are unreliable in their precision because they predict  $^{31}\text{F}$  to be unbound. Those that do predict  $^{31}\text{F}$  to be bound suggest that this nucleus is located at the drip-line. It has yet be shown experimental that  $^{31}\text{F}$  is the last bound fluorine isotope.

Two experiments were performed using the coupled cyclotron facility at the National Superconducting Cyclotron Laboratory to produce nuclei near the neutron drip-line of  $Z = 8$ . Nuclei were produced from the fragmentation of an  $^{40}\text{Ar}$  projectile with a  $^9\text{Be}$ , a  $^{nat}\text{Ni}$ , and a  $^{181}\text{Ta}$  target and a  $^{48}\text{Ca}$  beam with a  $^{181}\text{Ta}$  target. The production yields from each reaction were measured to determine the effect of the neutron excess of the target at intermediate energies and in an attempt to determine the location of the drip-line above oxygen. The cross sections of the most neutron-rich nuclei at intermediate energies of  $\sim 127$  MeV/nucleon were found to be enhanced by the target's neutron excess. The momentum distributions and momentum transfers

of the produced neutron-rich nuclei were measured and compared to theoretical predictions. Simulations from an intranuclear cascade code developed for slightly higher bombarding energies ( $E/A > 200$  MeV/nucleons) and a deep inelastic transfer code developed for low energies (i.e. energies where the De Broglie wavelength  $\gg$  distance between nucleons) have been compared with experimental results from the present work in an attempt to gain an understanding of reaction mechanism. In addition, the cross sections were compared with the predictions from a semi-empirical parameterization formula developed for high-energy reactions and to experimental results from RIKEN. The cross sections were found to be energy independent for the projectile energies ranging from 90-130 MeV/nucleon. The widths of the momentum distributions were consistent with widths resulting from the statistical emission of a single cluster and the fragment velocities were similar to the velocities resulting from low energy transfer mechanism.

*To  
my family*

## ACKNOWLEDGMENTS

I would like to thank my advisor professor Dave Morrissey for his guidance and patience as I learned my profession. I appreciate the opportunity that he gave to me to participate in other types of experiments. I would also like to express my sincere appreciation to the A1900 group, especially Tom Ginter, Mathias Steiner, Andreas Stolz, for all their help, their hard work to insuring proper delivery of the beam and maintaining the A1900 and their willingness to take time out of their busy schedule to answer questions. It was because of the caliber of people that works at the NSCL, that made it an enjoyable and fulfilling experience. I also like to thank the faculty and staff at the NSCL for their willingness to help and to answer any questions that I had.

I am grateful for professor Paul Mantica for his suggestions and advise about careers in nuclear science and the members of my committee, professors Tim Beers, Filomena Nunes, Wayne Repko and Brad Sherrill, for their guidance and suggestions. In addition, I would like to thank George Souliotis for his assistance with the DIT+Gemini simulations.

It has been fun teasing the chemistry graduate students, Debbie Davies, Sean Liddick, Bryan Tomlin, and Chandana Sumithrarachchi over the years. They were great friends and make my experiences here very enlightening and interesting even though they are chemist. If it was not for the aid of Chandana “no one can pronounce my name properly”, Debbie and our post-doc Leo Weissman and their willingness take a shift every day that my experiment ran, I would not of been able to complete part of my dissertation. I would also like to thank Chandana for our discussions on everything from beta-delayed neutrons to basic principles, and my lunch companion Susan Musser for her friendship and conservations.

I would also like to thank my undergraduate professor Aruna Nadasen. He was the one that gave me my first real glimpse of current research at this facility and based

on his advice that I chose to attend this university. I am grateful for the Physics and Astronomy Department for supporting me in this long journey, especially for the graduate secretary Debbie Simmons and Professor Manhanti for their help with the physics graduation requirements. I have been fortunate to meet many interesting people through the department, such as Carlos Maidana. I am so thankful that I have met him and for his love, support, and encouragement during these last couple of months.

Finally, I would like to thank my parents, Ming and Sue, and my brother Radley for allowing me to chase after my dreams. Without them, I would of been unable to complete this journey.

# Contents

<b>1</b>	<b>Introduction</b>	<b>1</b>
<b>2</b>	<b>Fragmentation Models</b>	<b>6</b>
2.1	Empirical Parameterization (EPAX) . . . . .	8
2.2	Abrasion-Ablation Model . . . . .	14
2.3	Internuclear Cascade (INC) Model . . . . .	17
2.4	Deep Inelastic Transfer (DIT) Model . . . . .	23
2.5	De-excitation and evaporation of prefragments . . . . .	26
<b>3</b>	<b>Nuclei Near the Neutron Drip-Line</b>	<b>31</b>
3.1	Motivation . . . . .	31
3.2	Experimental Setup . . . . .	36
3.3	Electronic System . . . . .	40
3.4	Particle Identification . . . . .	43
<b>4</b>	<b>Discussion and Experimental Results</b>	<b>58</b>
4.1	Energy Loss . . . . .	58
4.2	Parallel Momentum Widths . . . . .	63
4.3	Parallel Momentum Transfer . . . . .	67
4.4	Cross sections . . . . .	73
<b>5</b>	<b>Summary</b>	<b>85</b>
<b>A</b>	<b>Input Parameters for ISABEL and GEMINI</b>	<b>89</b>
<b>B</b>	<b>Derivations</b>	<b>92</b>
B.1	Calculating uncertainties in the cross-sections . . . . .	92
<b>C</b>	<b>Data from the Fragmentation of <math>^{40}\text{Ar}</math></b>	<b>94</b>
C.1	Fragments produced from the fragmentation of $^{40}\text{Ar} + ^9\text{Be}$ . . . . .	94
C.1.1	Cross Section . . . . .	94
C.1.2	Parallel Momentum Widths . . . . .	96
C.1.3	Parallel Momentum Transfer . . . . .	98
C.1.4	Asymmetric factor . . . . .	100
C.2	Fragments produced from the fragmentation of $^{40}\text{Ar} + ^{nat}\text{Ni}$ . . . . .	101
C.2.1	Cross Section . . . . .	101
C.2.2	Parallel Momentum Width . . . . .	103

C.2.3	Parallel Momentum Transfer . . . . .	105
C.2.4	Asymmetric factor . . . . .	107
C.3	Fragments produced from the fragmentation of $^{40}\text{Ar} + ^{181}\text{Ta}$ . . . . .	108
C.3.1	Cross Section . . . . .	108
C.3.2	Parallel Momentum Widths . . . . .	109
C.3.3	Parallel Momentum Transfer . . . . .	111
C.3.4	Asymmetric factor . . . . .	114
C.3.5	Angular Transmission . . . . .	115
<b>D</b>	<b>Data from the Fragmenation <math>^{48}\text{Ca}</math> with <math>^{181}\text{Ta}</math></b>	<b>116</b>
D.1	Fragments produced from the fragmentation of $^{48}\text{Ca} + ^{181}\text{Ta}$ . . . . .	116
D.1.1	Cross Section . . . . .	116
D.1.2	Parallel Momentum Widths . . . . .	118
D.1.3	Parallel Momentum Transfer . . . . .	119
D.1.4	Asymmetric factor . . . . .	121
D.1.5	Angular Transmission . . . . .	122
<i>Bibliography</i>		<b>124</b>

# List of Figures

1.1	Chart of the Nuclide . . . . .	2
1.2	cross sections of nuclei produced by projectile fragmentation of $^{48}\text{Ca}$ with a $^{181}\text{Ta}$ target. . . . .	3
2.1	The N-N cross sections as a function of projectile energy . . . . .	7
2.2	EPAX comparison . . . . .	13
2.3	Overview of the Projectile Fragmentation Process . . . . .	16
2.4	Nuclear Density . . . . .	19
2.5	Excitation energy of prefragments from the reaction of $^{40}\text{Ar}$ with $^{12}\text{C}$ . . . . .	20
2.6	Comparison of prefragment distributions from the ablation-abrasion model in LISE and ISABEL . . . . .	22
2.7	Comparison of the prefragment excitation energies from ISABEL for the reaction of $^{40}\text{Ar}$ with three N/Z targets . . . . .	23
2.8	Cross section comparison . . . . .	30
3.1	The neutron single particle energy levels . . . . .	32
3.2	Disappearance of magic numbers . . . . .	33
3.3	Chart of the Nuclides: $Z \leq 20$ . . . . .	34
3.4	Nuclei along the neutron drip-line . . . . .	35
3.5	One- and two neutron separation energies of fluorine . . . . .	36
3.6	Schematics of the A1900 fragment separator . . . . .	39
3.7	Schematic diagram of the focal plane detectors . . . . .	40
3.8	Angular acceptance of fragments at the focal plane . . . . .	41
3.9	Schematic electronics diagram of the A1900 . . . . .	42
3.10	Walk due to the CFD . . . . .	43
3.11	CFD correction . . . . .	44
3.12	A PID of Neutron-Rich Nuclei . . . . .	45
3.13	Energy resolution of the Si PIN detectors . . . . .	47
3.14	Mass resolution . . . . .	49
3.15	Angular acceptance . . . . .	51
3.16	Angular acceptance: Mocadi simulations . . . . .	52
3.17	Efficiency of the PPAC . . . . .	53
3.18	Current calibration . . . . .	54
3.19	Yield distribution of $^{20}\text{N}$ produced from the reaction of $^{40}\text{Ar}$ with $^{9}\text{Be}$ . . . . .	55
3.20	Momentum distribution of the fluorine isotopes from the reaction of $^{40}\text{Ar}$ with $^{9}\text{Be}$ , $^{nat}\text{Ni}$ , and $^{181}\text{Ta}$ . . . . .	56

4.1	Secondary reactions . . . . .	59
4.2	Broadening of parallel momentum width . . . . .	62
4.3	Determination of the target constant . . . . .	63
4.4	Experimental reduced widths . . . . .	65
4.5	Parallel momentum widths (high momentum side) . . . . .	67
4.6	Momentum transfer of fragments produced in the reaction of $^{238}\text{U}$ with Ti and Pb . . . . .	69
4.7	Average momentum transfer . . . . .	71
4.8	Momentum transfer comparisons . . . . .	73
4.9	Average fragment velocities . . . . .	74
4.10	Cross sections from the reaction of $^{40}\text{Ar}$ with $^9\text{Be}$ . . . . .	76
4.11	Cross sections from the reaction of $^{40}\text{Ar}$ with $^{nat}\text{Ni}$ . . . . .	77
4.12	Cross sections from the reaction of $^{40}\text{Ar}$ with $^{181}\text{Ta}$ . . . . .	78
4.13	Cross sections from the reaction of $^{48}\text{Ca}$ with $^{181}\text{Ta}$ . . . . .	79
4.14	Cross section comparisons of nuclei produced in the reaction of $^{40}\text{Ar}$ with $^9\text{Be}$ and $^{nat}\text{Ni}$ . . . . .	80
4.15	Cross section comparisons of nuclei produced in the reaction of $^{40}\text{Ar}$ and $^{48}\text{Ca}$ with $^{181}\text{Ta}$ . . . . .	81
4.16	Nuclear binding energy . . . . .	82
4.17	Effect of neutron excess on cross sections . . . . .	83
4.18	Particle Identification of $^{31}\text{F}$ . . . . .	84
4.19	Cross sections for producing $^{31}\text{F}$ . . . . .	84

# List of Tables

2.1	Summary of the reaction models . . . . .	9
3.1	Theoretical Neutron Separation Energies of Neutron-rich Fluorine . . . . .	35
3.2	Effective thickness of targets . . . . .	37
3.3	Resolution of Si PIN detectors . . . . .	47
3.4	Coefficients for the angular transmission . . . . .	51
3.5	Corrections to beam current at low intensities . . . . .	55
4.1	Coefficients of the range . . . . .	61
4.2	Target constants . . . . .	62
4.3	Contributions due to energy straggling in the momentum width of $^{22}\text{O}$ . . . . .	64
4.4	Reduced width . . . . .	68
4.5	Longitudinal momentum parameters . . . . .	68
4.6	The slopes of the average parallel momentum transferred . . . . .	70
A.1	ISABEL Input Parameters . . . . .	90
A.2	GEMINI Input Parameters . . . . .	91
C.1	Reaction Cross Sections of $^{40}\text{Ar} + ^9\text{Be}$ for Neutron-Rich Nuclei . . . . .	94
C.2	Parallel momentum width from the reaction of $^{40}\text{Ar} + ^9\text{Be}$ . . . . .	96
C.3	Parallel momentum transferred from the reaction of $^{40}\text{Ar} + ^9\text{Be}$ . . . . .	98
C.4	Asymmetric factor. . . . .	100
C.5	Reaction Cross Sections of $^{40}\text{Ar} + ^{nat}\text{Ni}$ for Neutron-Rich Nuclei . . . . .	101
C.6	Parallel momentum width from the reaction of $^{40}\text{Ar} + ^{nat}\text{Ni}$ . . . . .	103
C.8	Asymmetric factor. . . . .	107
C.9	Reaction Cross Sections of $^{40}\text{Ar} + ^{181}\text{Ta}$ for Neutron-Rich Nuclei . . . . .	108
C.10	Parallel momentum widths from the reaction of $^{40}\text{Ar} + ^{181}\text{Ta}$ . . . . .	110
C.11	Parallel momentum transferred from the reaction of $^{40}\text{Ar} + ^{181}\text{Ta}$ . . . . .	111
C.12	Asymmetric factor. . . . .	114
C.13	Angular transmission of fragments . . . . .	115
D.1	Reaction Cross Sections of $^{48}\text{Ca} + ^{181}\text{Ta}$ for Neutron-Rich Nuclei . . . . .	116
D.2	Parallel momentum widths from the reaction of $^{48}\text{Ca} + ^{181}\text{Ta}$ . . . . .	118
D.3	Parallel momentum transferred from the reaction of $^{48}\text{Ca} + ^{181}\text{Ta}$ . . . . .	119
D.4	Asymmetric factor. . . . .	121
D.5	Angular transmission of fragments . . . . .	122

# Chapter 1

## Introduction

The completion of the coupled cyclotron facility (CCF) in 2001 permitted the National Superconducting Cyclotron Laboratory (NSCL) to accelerate stable nuclei to energies well above 100 MeV/nucleon at high intensities [1]. As a result, more exotic regions of the chart of nuclide may be explored than in the past. Nuclei in these exotic regions typically have very short half-lives, on the order of a few hundred milliseconds or less, and they can have significantly different structural properties than those nuclei located near the valley of  $\beta$ -stability. As shown in Figure 1.1, presently about 2500 nuclei (dark gray squares), including the  $\sim$ 270 stable isotopes (black squares) that are present in nature, have been observed out of the perhaps  $\sim$ 7500 nuclei (light gray squares) that are predicted to be particle bound. Nuclei located near the limits of stability are extremely useful in testing nuclear theories due to the higher sensitivity to the input parameters of the nuclear potential [2]. Extrapolations of nuclear properties of nuclei near  $\beta$ -stability to predict the location of the drip-line have been undependable [3,4]. Unique features such as halo structures and nuclear deformations that lead to shell quenching have been observed in some of these nuclei near the drip-line [5].

Radioactive isotopes have been produced by a variety of different techniques such as Coulomb dissociation, direct reactions, fission, fusion, and other processes. To observe short-lived nuclei such as those located at drip-lines, a technique known as

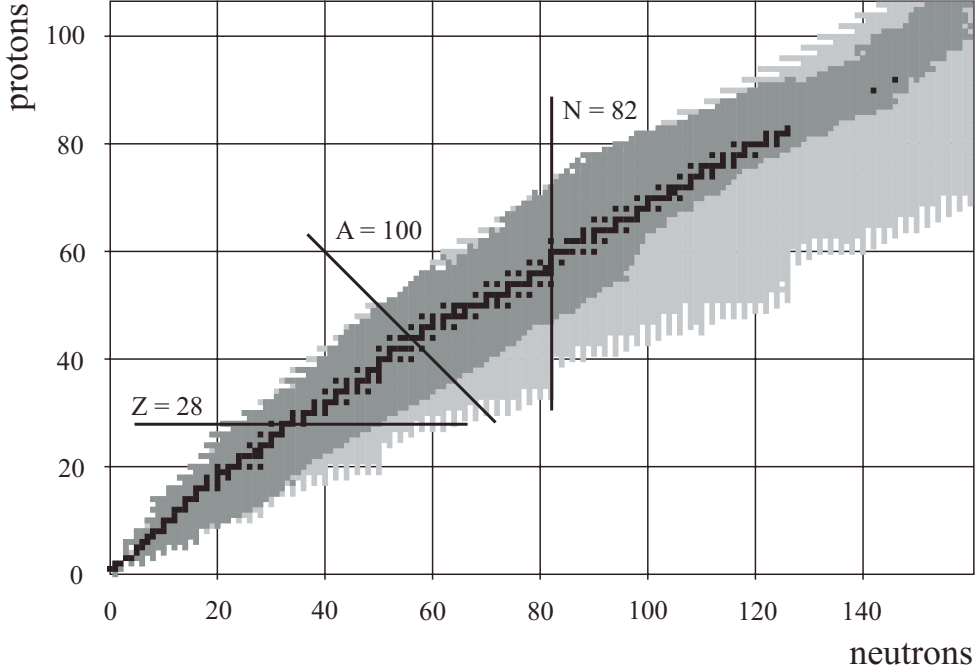


Figure 1.1: The terra incognita or unexplored region of the chart of nuclide as predicted by Tachibana is shown in light gray, the valley of stability is depicted by the black squares, and the observed nuclei are shown in dark gray. The figure is from reference [3].

projectile fragmentation was developed to quickly produce, separate and identify the nuclei of interest in-flight before they are able to decay. Projectile fragmentation has been widely used to produce nuclei along the proton and neutron drip-lines (regions where an additional nucleon can no longer be bound because the proton or neutron separation energy approaches zero). A large number of nuclei lighter than the projectile (or target in the case of target fragmentation) are produced in a pure fragmentation process. Shown in Figure 1.2 are the nuclei expected to be produced by the fragmentation of  $^{48}\text{Ca}$  with  $^{181}\text{Ta}$  and their distributions made by the empirical formula EPAX [6, 7] (see section 2.1) in LISE [8]. The fragments created in the fragmentation process may be used as secondary beams to produce very exotic nuclei that may be important in astrophysical processes or in the study of nuclear structure and reaction properties.

The CCF located on the campus of Michigan State University produces radioactive ions by such a method. This technique has been proven useful in observing the

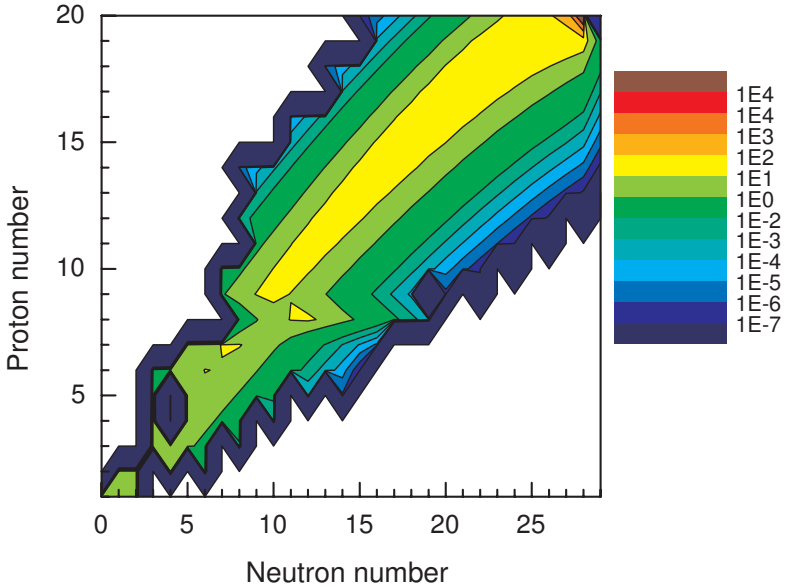


Figure 1.2: The predicted cross sections from EPAX of nuclei (in mb) produced by projectile fragmentation of  $^{48}\text{Ca}$  with a  $^{181}\text{Ta}$  target.

shortest-lived particles near the drip-lines for the first time [3, 9, 10, 11]. Facilities such as Rikagaku Kenkyusho (RIKEN) in Japan, Gesellschaft für Schwerionenforschung mbH (GSI) in Darmstadt, Germany, Grand Accelerateur National d’Ions Lourds (GANIL) in Caen, France and the NSCL in the United States are at the forefront of producing these rare and exotic nuclei. The use of synchrotron facilities such as the Heavy Ion Synchrotron (SIS) at GSI allows projectiles to be accelerated to very high energies ( $\sim 90\%$  the speed of light) [12]. Current cyclotrons are unable to produce such high-energy projectiles due to the large radii required in the magnets, yet they remain useful because of their ability to produce continuous beams at higher intensities than synchrotrons [13]. Measurements of the systematic trends in the observables from fragmentation products (i.e. the momentum width, the momentum centroid, and the production yields) at a number of bombarding energies are necessary in order to improve on the accuracy of predicting the intensity of fragments away from  $\beta$ -stability and towards the drip-lines. The intensities of these fragments will determine the fea-

sibility of observing rare particles near the drip-lines in a reasonable amount of time at the existing facilities.

Early work done in the late 1970's at Lawrence Berkley Laboratory (LBL) demonstrated the usefulness of projectile fragmentation in creating radioactive nuclei [14]. The fragmentation process creates radioactive nuclei through peripheral collisions of a projectile nucleus with a target nucleus (impact parameter ( $b$ ) >  $R_1 - R_2$ , where  $R_1$  and  $R_2$  are the radii of the interacting nuclei). The fragments are emitted in a narrow forward facing cone with velocities approximately equal to those of the projectiles. Devices placed at zero degrees in the reaction plane such as fragment separators were developed to capitalize on this property of the fragments and can be used to separate and isolate specific groups of nuclei for further study. Central collisions ( $b < R_1 - R_2$ ) at intermediate and high energies lead to the annihilation of the nucleus through multi-fragmentation. These violent collisions tend to have large multiplicities and typically occur only about 10% of the time for  $A_1/A_2 \geq 0.2$ . Fragments produced in this type of collision are thought to be emitted isotropically in space in the moving reference frame [15]. Devices such as the  $4\pi$  arrays are well suited to study such reactions while fragment separators such as the A1900 and RIPS are more appropriate in studying nuclei produced in peripheral collisions. The rest of this dissertation will be restricted to examining the fragments produced in peripheral collisions.

The probability of a projectile nucleus to collide with a target with an areal density ( $n$ ) can be described using Beers' law:

$$\frac{I}{I_o} = e^{-n\sigma x}. \quad (1.1)$$

Given this dependence, it is easy to see that the intensity of the projectile ( $I$ ) will be attenuated from its initial value ( $I_o$ ) as it travels a distance  $x$  through the absorbing material or target. The attenuation coefficient ( $n\sigma$ ) of the absorber determines the likelihood with which the projectile will collide with a target nucleus. In most cases,

the projectile will not interact with a target nucleus by the short-range nuclear force, but will always interact with the target atoms via the long range Coulomb force. This Coulomb interaction will cause the projectile to deposit part of its kinetic energy in the target as it travels through the absorbing material. Thus, the final products from a nuclear interaction will also have atomic energy-losses. This effect on the observed momentum distributions will be discussed in detail in Chapter 4.

The reaction mechanism that describes the fragmentation of a nucleus has been studied in detail by many authors using various models such as an incoherent droplet model [16], the abrasion ablation model [17, 18], the internuclear cascade model [19, 20, 21], and a deep inelastic transfer model [22, 23]. The latter three models will be presented in details in the following chapter. The experimental objectives and motivations along with a description of the experiments conducted at the NSCL will be presented in Chapter 3 with the experimental results presented in Chapter 4 and summarized in Appendices C and D. An overview of several theoretical models that attempt to explain the mechanism(s) that produces the observables of the projectile fragmentation process will also be discussed in Chapter 4, along with comparisons to the internuclear cascade and deep inelastic transfer models and other experiments will be made. Finally in Chapter 5, conclusions from the present work will be drawn and summarized.

# Chapter 2

## Fragmentation Models

The products of the projectile fragmentation process can be used to determine the existence of rare nuclei along the drip-lines or they can be used to create short-lived radioactive beams for a variety of other reactions. The intensity of these secondary beams is crucial in determining the feasibility in studying properties of rare radioactive nuclei. From Equation 1.1, it can be seen that the production rate is related to the reaction cross section ( $\sigma$ ). The cross sections of heavy-ion reactions are often approximated using a empirical formula EPAX [6, 7] in simulation programs like INTENSITY [24] and LISE [8] where the user seeks to quickly calculate the expected production yields. The disadvantage of using a parameterization of the yields is that it gives no insight into the mechanism that produces the observed nuclei. More computer-intensive codes that typically involve Monte Carlo calculations have been developed in an attempt to understand the reaction process that produces the observed fragments [25, 26]. Characteristics of the “prefragment” distributions predicted by these codes are not directly measurable by experimental means but are important in the determination of the final fragments. These properties can only be tested indirectly through the observables of the final fragments. Thus, it is important to test the validity of these codes against experimental data.

The reaction mechanism that produces the observed fragments is known to change

with the interaction time and particle momenta and hence is energy dependent [29]. At high energies, where the projectile's de Broglie wavelength ( $\lambda_D$ ) is much smaller than the average distance between nucleons in the target (d), the nucleons in the projectile can interact with those in the target through nucleon-nucleon interactions. Gaussian momentum distributions of the reaction products, whose widths are governed by the Fermi motion of the projectile nucleons, are observed because of the statistical nature of the process. Asymmetries in the distributions occur at lower projectile energies where the diffusion process starts to become important. At low projectile energies (i.e.  $\lambda_D \gg d$ ), the projectile interacts with the whole target nucleus and at Coulomb barrier energies can form a compound nucleus in which nucleon-nucleon interactions are suppressed due to strong Pauli blocking [29]. The time of interaction for these low-energy reactions can be as much as  $10^6$  times longer than that for

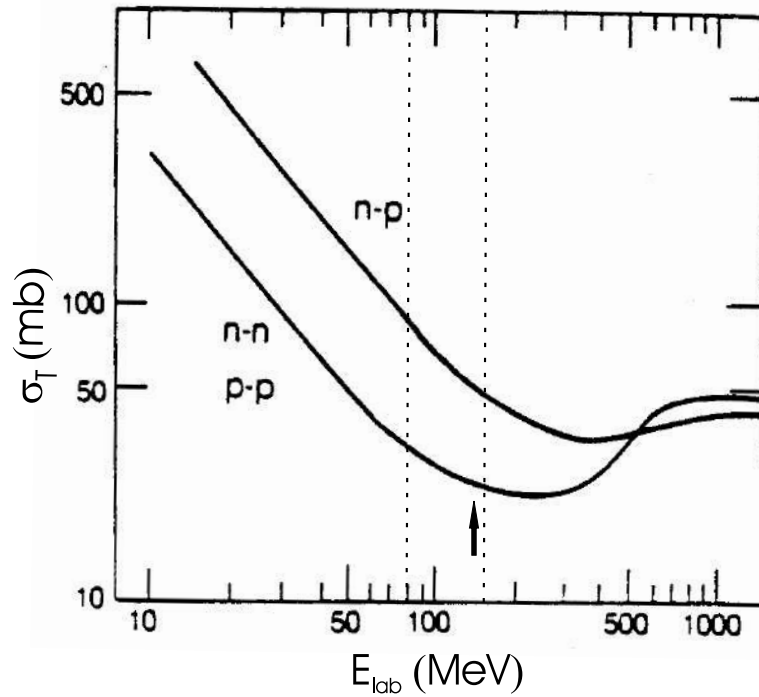


Figure 2.1: The free neutron-proton (n-p), neutron-neutron (n-n) and proton-proton (p-p) cross sections are shown as a function of projectile energy. The figure is from reference [27]. The region between the two vertical lines are the projectile energies of primary beams produced at the NSCL, see [28]. The arrow indicates the bombarding energies of the two projectiles used in the current work.

reactions at high energies. Central collisions at these energies result in fusion of the nuclei while deep inelastic transfers dominate in collisions that are more peripheral. The reaction mechanisms at the two energy extremes have been studied for many years [30, 31]. More complete studies of fragmentation at the intermediate energy domain ( $\lambda_D \sim d$ ) are needed to determine whether the known reaction mechanisms relevant at high and low projectile energies persist. At these energies, it is well known that the free nucleon-nucleon cross sections are reduced (see Figure 2.1), the transfer mechanism that leads to nuclei that are heavier than the projectile is suppressed and the momentum distributions are more symmetric. Studies at this energy range near the Fermi energy ( $E_F \sim$  from 20 to 50 MeV/nucleon [32] in the center of mass) are important to better understand how the reaction mechanisms transitions from one to the other. The current CCF can accelerate stable beams, such as  $^{78,86}\text{Kr}$  and  $^{58,64}\text{Ni}$ , to the intermediate energy regime. Four projectile fragmentation reactions from beams produced at the CCF were used to test the predictions of the internuclear cascade model (valid at relativistic energies) and a deep inelastic transfer model (valid at non-relativistic low projectile energies) to determine whether these mechanisms can describe the distribution of products at intermediate bombarding energies ( $\sim 130$  MeV/nucleon). These models along with the abrasion-ablation model, and EPAX and will be discussed further in the following subsections. The four models discussed above are summarized in Table 2.1.

## 2.1 Empirical Parameterization (EPAX)

As mentioned above, EPAX is an empirical formulation fitted to known cross sections of heavy-ion reactions in the limiting fragmentation regime. Currently there are two versions of EPAX available, EPAX 1.0 [6] and EPAX 2.15 [7]. The parameterization obtained for the first version of EPAX (EPAX 1.0) relied primarily on proton-induced spallation cross sections. Modifications were necessary to be able to describe more

Table 2.1: Comparison of the four reaction models discussed in the text.

EPAX [6, 7]		Abrasion-Abrasion	
type	parameterization	type	macroscopic
number of stages	-	number of stages	2
energy regime	relativistic (limiting fragmentation)	energy regime	relativistic ( $\lambda \ll d$ )
interaction excitation energy	-	interaction	geometric <sup>1,2</sup> , geometric + friction <sup>2</sup> , diabatic <sup>3</sup>
		excitation energy	$\Delta S \cdot E_s^{1,4}$ , $E_{surf} + m_{FSI} \langle E_{FSI} \rangle^{2,5}$ , constant $\cdot \Delta A^3$
INC [19, 20, 25]		DIT [23]	
type	microscopic	type	microscopic
number of stages	2	number of stages	2
energy regime	relativistic ( $\lambda \ll d$ )	energy regime	non-relativistic ( $\lambda \gg d$ )
interaction excitation energy	nucleon-nucleon $\sum E_{particle} + \sum E_{hole}$	interaction	nucleon transfer
		excitation energy	$\int P \Delta E_p dt + \int P \Delta E_h dt$

<sup>1</sup>From reference [17].

<sup>2</sup>From reference [18].

<sup>3</sup>From reference [33].

<sup>4</sup> $\Delta S = 4\pi R \cdot (1 + P - (1 - F)^{2/3})$ , where F and P are functions of the impact parameter and nuclear radii (see reference [34]).  $E_s$  is the nuclear surface energy coefficient. This is a lower limit to the excitation energy.

<sup>5</sup> $E_{surf}$  is the extra surface energy,  $m_{FSI}$  is the number of final state interactions and  $\langle E_{FSI} \rangle$  is the average energy deposited due to friction.

complete and recent data from relativistic heavy-ion reactions produced by projectile fragmentation. The more recent work showed that the cross section distributions were more neutron-rich and broader than the previous measurements of lighter nuclei. The parameterizations made in EPAX are valid in the case where the reaction yields are energy independent (i.e. in the regime of “limiting fragmentation”) and does not describe products produced from fission or nucleon pickup.

For proton induced reactions at energies well above the Fermi energy, Rudstam [35] suggested some time ago that the fragment yield  $\sigma(Z, A)$  for a projectile of mass  $A_p$  and charge  $Z_p$  incident on a  $^{A_t}Z_t$  target in the case of projectile fragmentation can be written as

$$\sigma(Z, A) = Y(A) \cdot \sigma(Z_{prob} - Z) \quad (2.1)$$

where the first term in Equation 2.1 is the isobaric mass yield (total isobaric cross section). The second term describes the charge dispersion centered about the most probable charge number ( $Z_{prob}$ ) for a given mass number ( $A$ ) and is written in terms of an exponential

$$\sigma(Z_{prob} - Z) = n e^{-R|Z_{prob} - Z|^U}. \quad (2.2)$$

Sümmerer et al. found the simplicity of Equation 2.1 convenient and with small modifications to Equation 2.2, data from a variety of relativistic reactions could be reproduced. They parameterized the isobaric mass yield as

$$Y(A) = \sigma_R P(A_p) e^{-P(A_p) \cdot (A_p - A)} \begin{cases} 1 + y_1 \cdot (\frac{A}{A_p} - y_2)^2 & \frac{A}{A_p} \geq y_2 \\ 1 & \text{otherwise} \end{cases} \quad (2.3)$$

where the slope of the exponential is defined as

$$P(A_p) = e^{P_2 A_p + P_1} \quad (2.4)$$

and the scaling factor in barns is written as

$$\sigma_R = \sigma_2 \cdot (A_P^{1/3} + A_t^{1/3} + \sigma_1). \quad (2.5)$$

Sümmerer et al. redefined the second term for the charge dispersion in Rudstam's formula (2.1) by the following Equation

$$\sigma(Z_{prob} - Z) = n \cdot e^{-R|Z_\beta + \Delta + \Delta m - Z|^U} \quad (2.6)$$

were the  $\beta$  stable charge ( $Z_\beta$ ) is approximated by the liquid drop expression

$$Z_\beta = \frac{A}{1.98 + 0.0155A^{2/3}} \quad (2.7)$$

and the difference between the experimental values of  $Z_p$  and  $Z_\beta$  is parameterized as

$$\Delta = \Delta_A \begin{cases} \Delta_2 A + \Delta_1 & A \geq \Delta_4 \\ \Delta_3 A^2 & \text{otherwise} \end{cases} \quad (2.8)$$

where  $\Delta_A$  is defined as

$$\Delta_A = \begin{cases} 1 + d_1 \cdot (\frac{A}{A_P} - d_2)^2 & \frac{A}{A_p} \geq r_2 \\ 1 & A \text{ near } \beta\text{-stability.} \end{cases} \quad (2.9)$$

The three parameters  $n$ ,  $R$ , and  $U$  in Equation 2.6 are defined by

$$\text{normalization term } n = \sqrt{\frac{R}{\Pi}} \quad (2.10)$$

width parameter

$$R = e^{R_2 A + R_1} \begin{cases} 1 + r_1 A_p \cdot (\frac{A}{A_p} - r_2)^4 & \frac{A}{A_p} \geq r_2 \\ 1 & \text{A near } \beta\text{-stability} \end{cases} \quad (2.11)$$

and

$$U = \begin{cases} U_1 + U_2 A + U_3 A^2 & \text{proton-rich exponent} \\ U_n & \text{neutron-rich exponent} \end{cases} \quad (2.12)$$

are used to control the shape of the distributions. The value of  $Z_{prob}$  was found to lie on the neutron-rich side of the valley of stability and in the case of target fragmentation  $Z_{prob}$  was dependent on the neutron/proton excess of the target relative to  $\beta$ -stability. For targets close to  $\beta$  stability,  $Z_{prob}$  was found to depend only on the fragment mass while neutron-rich and neutron-deficient fragments were found to retain some memory of the neutron/proton excess of the target. The parameter

$$\Delta_m = (Z - Z_\beta) e^{p_1 + (p_2 A)/A_p} \quad (2.13)$$

is necessary in Equation 2.6 to account for this “memory effect”. The resulting set of twenty parameters  $y_1, y_2, d_1, d_2, P_1, P_2, \sigma_1, \sigma_2, R_1, R_2, r_1, r_2, U_1, U_2, U_3, p_1, p_2, \Delta_1, \Delta_2$  and  $\Delta_3$  in Equations 2.3-2.13 were determined by fitting the available experimental data and their fitted values can be found in reference [7]. The values of the constants obtained from target fragmentation are also valid for predicting fragment cross sections produced by projectile fragmentation because the same laws must govern both reactions. No effects from the use of different projectiles were included into the parameterization aside from the cross section normalization in Equation 2.5.

The parameterization obtained in the second version of EPAX (EPAX 2.15) has been found to be a good approximation for calculating cross sections of many nuclei near and far from  $\beta$ -stability. For example, a comparison of experimental cross sections from the reactions of  $^{48}\text{Ca}$  with Be (panels a and b) and  $^{86}\text{Kr}$  with Be (panels c

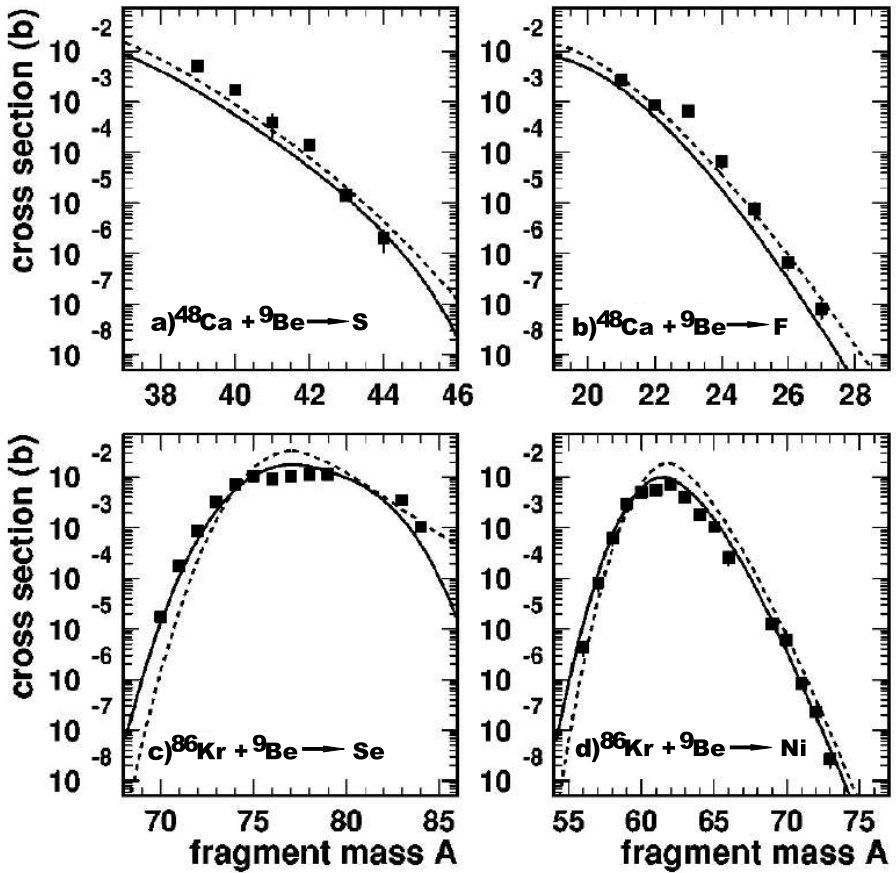


Figure 2.2: Comparison of the cross sections from EPAX with data from the reactions of  $^{48}\text{Ca}$  with  $^9\text{Be}$  to produce a) sulfur and b) fluorine isotopes and  $^{86}\text{Kr}$  with  $^9\text{Be}$  to produce c) Selenium and d) Nickel. The dashed curves are predictions from the first version of EPAX and the solid curves are from the second version. The figure is from reference [7] and the data are from references [36, 37].

and d) with the two versions of EPAX are shown in Figure 2.2. The data from the fragmentation of  $^{48}\text{Ca}$  and  $^{86}\text{Kr}$  were obtained from references [36] and [37]. The  $^{86}\text{Kr}$  data appears to be better described by the second version of EPAX (solid curve), while the original version (dashed curve) describes the  $^{48}\text{Ca}$  data better. The cross sections predicted by EPAX 2.15 will be compared with data from this work in order to establish the validity of the EPAX predictions for nuclei near the neutron drip-line and to determine whether EPAX can reproduce the cross sections of fragments produced in projectile fragmentation on different targets.

## 2.2 Abrasion-Ablation Model

One of the earliest models that attempted to describe fragmentation of heavy-ion beams at high bombarding energies, known as the geometric abrasion-ablation model, was developed in 1973 at LBL by Bowman et al. [17]. The geometric abrasion-ablation model is a macroscopic model applied to heavy-ion reactions at relativistic energies ( $E > 200$  MeV/nucleon). Bowman et al. speculated that at extremely high energies, the interacting nucleons have such large momenta that they continue along straight lines during the nucleon-nucleon collisions. Residues resulting from peripheral collisions are thus emitted in the forward direction with velocities near that of the projectile. The geometric abrasion-ablation model elaborated on a concept first proposed by Serber in 1947. Serber suggested that the process for high energy proton collisions occurs in two distinct stages: a quick abrasion stage and a slower ablation stage [38]. The interactions between the projectile and target nucleons during the abrasion stage will typically last on the order of  $10^{-23}$  s during which time the nucleons in the region of interaction (the participants) are removed or “abraded” from the projectile leaving the remaining nucleons in the projectile and target (the spectators or prefragment) in an excited state. The collisions between two sharp well defined spheres of the projectile and target nuclei with radii  $r_o A^{1/3}$  ( $r_o \sim 1.2$  fm) will gouge out concave cylindrical surfaces from each sphere exposing larger surface areas. The number of nucleons removed during this process is dependant on the impact parameter  $b(A)$  and the nuclear radii. Geometric formulas that determine the number of removed nucleons are available, see reference [15] for an example. From the integration of the volume of overlap between a cylinder and a sphere, it can be shown that the cross section of the residual mass ( $\sigma(A)$ ) can be represented as a function a function of  $b(A \pm 0.5)$  only [17, 34]:

$$\sigma(A) = \pi \cdot b^2(A + 0.5) - b^2(A - 0.5). \quad (2.14)$$

The neutron-to-proton ratio (N/Z) remains undetermined from geometric consid-

erations alone. Other assumptions must be made to determine the number of each constituent in the prefragment. These assumptions range from having a fixed or correlated proton-to-neutron ratio (i.e.  $N_{PF}/Z_{PF} = N/Z$ ) to an uncorrelated or statistical probability of removing a nucleon [34]. In the statistical model, the probability  $P(A_{PF}, Z_{PF})$  of obtaining a prefragment with  $N_{PF}$  neutrons and  $Z_{PF}$  protons from a  $^A Z_N$  projectile can be described using the hypergeometric distribution:

$$P(A_{PF}, Z_{PF}) = \frac{\binom{Z}{Z - Z_{PF}} \binom{N}{N - N_{PF}}}{\binom{A}{A - N_{PF} - Z_{PF}}} \quad (2.15)$$

where the terms within the parenthesis represents binomial coefficients. The distribution function described in Equation 2.15 has no correlations and tends to be very broad. An alternative method of determining the neutron-to-proton ratio proposed by Morrissey et al. [34] yields a much narrower distribution. They suggested that fluctuations in the neutron-to-proton ratio are due to zero-point vibrations of the giant dipole resonance (GDR) that can arise due to the collective motion of the nucleons. The distribution of nucleons from the GDR about the primary charge  $Z$  can be described by a Gaussian of the form:

$$P(A, Z) = \frac{1}{\sqrt{2\pi\Delta A\sigma_Z^2}} e^{-\frac{(Z - \Delta A \cdot (Z_{PF}/A_{PF}))^2}{2\sigma_Z^2}}, \quad (2.16)$$

where  $\sigma_Z$  is a width parameter that depends on the relative motion of the nucleons in the giant dipole resonance. The width of this distribution can be obtained by determining the expectation value of the displacement of the neutrons relative to the protons using harmonic oscillator wave functions. Even though these two distributions are very different, they can lead to similar final products through statistical de-excitation

(ablation) [39].

After nucleons are removed by the abrasion process, the nucleons remaining in the prefragment are left in an excited state. The excited prefragment will de-excite through the emission of nucleons (protons and neutrons), light particles such as  $\alpha$  particles, and  $\gamma$ -rays. This secondary stage can last more than  $10^6$  times longer than the abrasion process and “washes out” the primary distribution. A schematic overview of the abrasion-ablation process is depicted in Figure 2.3.

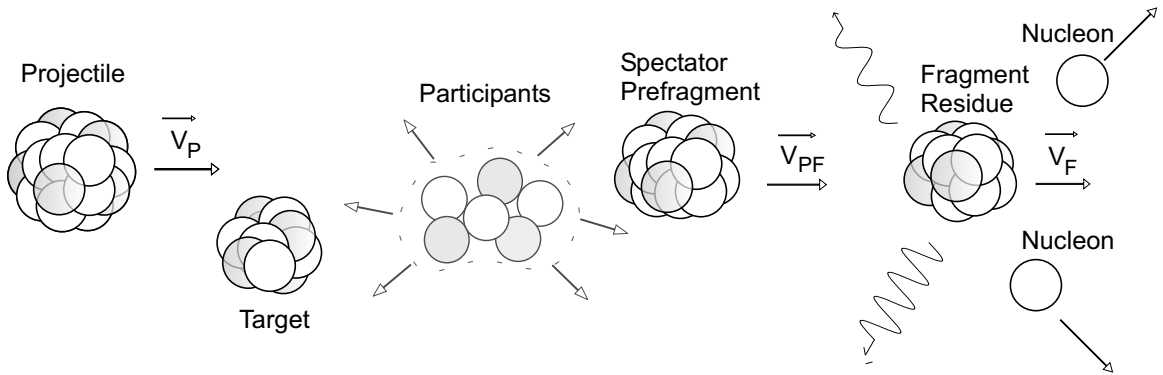


Figure 2.3: An illustration of the projectile fragmentation process.

The number of nucleons emitted during the ablation stage is strongly dependent on the excitation energy ( $E^*$ ) of the prefragment. In Bowman et al.’s geometrical picture, the excitation energy arises from the excess surface area of the deformed nucleus with a concave cylindrical surface gouged out compared to a sphere of equal volume. The cross section distributions calculated from the excitation energy obtained from this method were found to be too broad. Modifications were necessary to increase the magnitude of the excitation energy. Additions to the excitation energy can arise from interactions between the spectators and participants near the boundary of overlap during the time of collision. For example, these interactions will result in the transfer of kinetic energy to the spectators through scattering [18]. The addition of the frictional spectator interaction to the excitation energy has been shown to give a better description of the final cross sections.

Gaimard and Schmidt suggested an alternative approach to calculate the excita-

tion energy based on the probability that a nucleon will be in the participant zone during the projectile-target interaction [33]. This approach is known as the diabatic model. Nucleons within the nucleus are assumed to occupy single-particle energy levels within a nuclear potential that is approximated using the liquid droplet model. Nucleon-nucleon interactions will remove some nucleons from their energy levels during the collision creating holes within the potential well. An equal probability of removing a nucleon from any energy level is assumed. The total excitation energy of the prefragment after all interactions have occurred is then determined by the summation of the energies of these single particle holes relative to the Fermi Energy.

The geometric abrasion-ablation model (including friction) of Wilson et al [40] and the hole excitation model of Gaimard and Schmidt have been implemented in the simulation program LISE [8] in order to calculate the excitation energies of the prefragments. The input parameters used in LISE to determine the excitation energy can be constrained by comparing to a second model, the internuclear cascade (INC). The INC will be described in detail in the following section.

## 2.3 Internuclear Cascade (INC) Model

The nucleon-nucleon collisions during the fragmentation process at relativistic and intermediate energies have been described in a microscopic framework using internuclear cascade models. These classical microscopic models use few free parameters. The basic concept of all INC codes is that the incoming nucleons of the projectile undergo a series of nucleon-nucleon collisions within the target and projectile until they escape or fall below the binding energy of the nucleus. There are several versions of INC that differ on the treatment of nucleon-nucleon interactions. For the purposes of this dissertation, only the assumptions made by the two codes VEGAS [25] and ISABEL [19, 20] will be discussed. The INC codes called VEGAS (proton induced reactions) and ISABEL (generalized VEGAS code) assume time-dependent two-body

collisions between bound or cascading nucleons with other cascading nucleons and nucleons within the Fermi seas. The Fermi energy of the  $i^{th}$  type of nucleon (i.e. proton or neutron) in each projectile and target nuclei is given by the usual expression:

$$E_{Fi} = \frac{\hbar^2}{2m}(2\pi^2\rho_i)^{2/3}, \quad (2.17)$$

where  $\rho_i$  is the nuclear density of the nucleon of mass m. Collisions of nucleons within the two Fermi seas are also considered. The only restriction made in ISABEL is that the cascading nucleons may not sequentially collide with the same cascading nucleon without first interacting with another nucleon.

The projectile and target are assumed to move along classical trajectories in the center of mass frame until the two nuclei collide with each other allowing nucleons to interact. The nuclear densities of the projectile and target potentials are calculated in ISABEL using 16 step-functions (histograms) that approximates a folded-Yukawa-sharp-cutoff distribution with cutoff radius  $R_s = 1.18 \text{ A}^{1/3}$  (dashed curve), see Figure 2.4. The older code VEGAS uses one of three models to calculate the nuclear densities: a constant density, a trapezoidal distribution or a simple step function. The nucleons within the target and projectile nuclei are assumed to be cold degenerate Fermi gases trapped within their perspective potential wells. All quantum mechanical effects except for the Pauli exclusion principle are neglected. These classical approximations are valid in the regime where  $\lambda_D \ll d$ .

The cascading nucleons generally traverse a small distance within the nuclear medium before interacting with another nucleon. The mean free path between collisions is determined using the free nucleon-nucleon and nucleon-pion cross sections. Pions ( $\pi$ ) are created and absorbed as the result of the nucleon-nucleon (N-N) inter-

actions. The  $\pi$  modes of interactions can be described using the  $\Delta$  resonance:



The cascading nucleons will deplete the Fermi sea of its collision partner through the creation of holes with a volume of  $1/\rho$  in the density distributions. It is assumed that no other interactions can occur at the site of these holes. The incoming and cascading nucleons are tracked in small intervals of time until they escape the region of overlap, the volume defined by the nuclei (for nucleons outside the overlapping region) or until their total energy falls below the proton or neutron cutoff energy, where the nucleon will become captured. The cutoff energies of the nucleons are defined as

$$E_{cutoff}^{neutron} = E_F + 2 < BE > \quad (2.20)$$

$$E_{cutoff}^{proton} = \max \begin{cases} E_F + 2 < BE > \\ E_F + < BE > + E_{Coul} \end{cases} \quad (2.21)$$

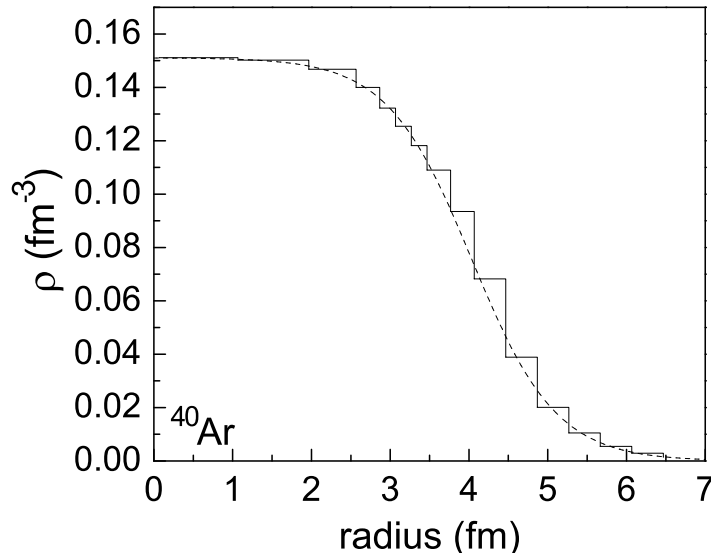


Figure 2.4: The density of  ${}^{40}\text{Ar}$  as a function of the nuclear radius is shown. The histogram is the estimation made in ISABEL to approximate a folded-Yukawa-sharp-cutoff distribution (dashed curve).

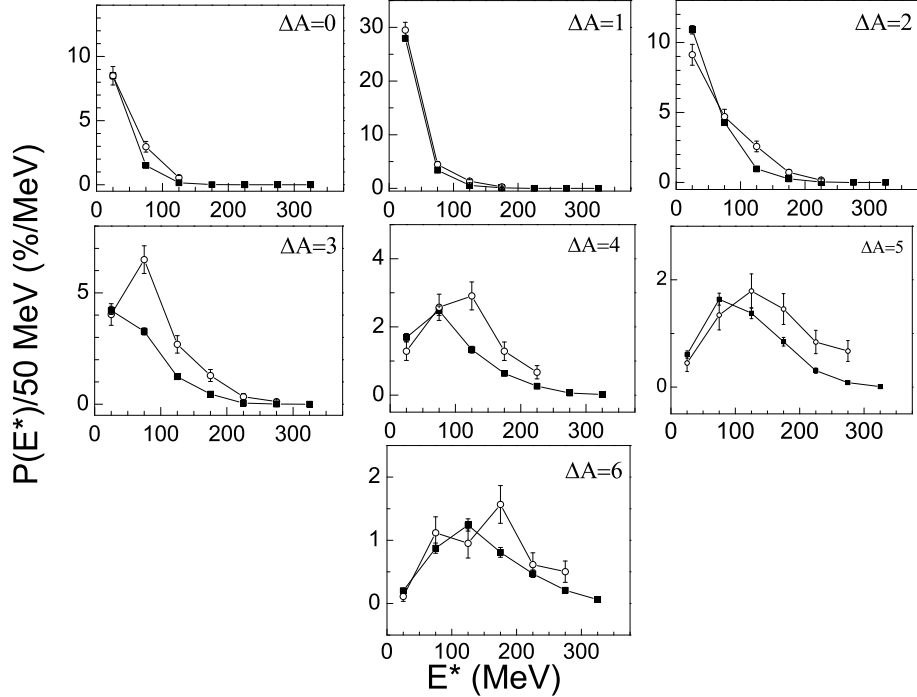


Figure 2.5: The probabilities to remove the first six nucleons from a  $^{40}\text{Ar}$  projectile are shown. The open circles are the excitation energies calculated in reference [39] and the solid squares are the calculated excitation energy from a LINUX version of ISABEL used in the present work. The two data sets were used to determine whether the Linux version of ISABEL is comparable with an older version of ISABEL.

where  $\langle \text{BE} \rangle$  represents the average binding energy,  $E_{\text{Coul}}$  is the Coulomb energy and  $E_F$  is the Fermi energy of the nucleus. All captured nucleons and holes in the density distribution contribute to the final excitation energy of the prefragment. The contributions from these terms are written as

$$E^* = \sum_{i=0}^{N_{\text{hole}}} E_{\text{hole}} + \sum_{i=0}^{N_{\text{particle}}} E_{\text{particle}} \quad (2.22)$$

where the hole and particle energies,  $E_{\text{particle}}$  and  $E_{\text{hole}}$ , respectively, are measured with respect to the Fermi energies.

To test a recent LINUX version of ISABEL [19, 20], a comparison of the excitation energies of the prefragments for removing zero to six nucleons from a 213 MeV/nucleon  $^{40}\text{Ar}$  projectile was made to an older version found in the literature [39]. The open circles in Figure 2.5 were taken from reference [39] and normalized by the

total number of counts and the filled squares are from the version used in this work. The probabilities were determined from the number of counts in 50 MeV increments (the data points including statistical error bars are positioned at the center of each of the 50 MeV increments). Both versions of ISABEL predict approximately the same excitation energy distributions and show that the prefragment becomes very excited as the number of removed nucleons increases.

A comparison of the predicted prefragment distributions for removing the first 12 nucleons from a  $^{48}\text{Ca}$  projectile from ISABEL (filled squares) using 30,000 primary events and the abrasion-ablation model in LISE (unfilled circles) are shown in Figure 2.6. The error bars associated with the ISABEL calculations are statistical. Note that the ablation-abrasion model does not allow for masses heavier than the projectile or transfer of nucleons, hence the predictions are only shown up to  $Z = 20$ . The abrasion-ablation model predicts similar distributions to those from ISABEL for small mass losses ( $A_f > 41$ ) and broader distributions of prefragments for larger mass losses. This variation is a direct consequence of the difference in excitation energy. ISABEL predicts narrower mass distributions, but the excitation energies of the prefragments are much larger (open squares) than the energies from the abrasion-ablation model (lines =  $13.3 \text{ MeV}/\Delta A$ ). Even so, the prefragment distributions of ISABEL and the abrasion-ablation model can lead to similar cross sections of the final fragments.

The excitation energy of the prefragments in the LISE version of the abrasion-ablation model is a variable parameter, while the energies predicted by ISABEL are not. The excitation energies of the prefragments from ISABEL do depend on the target. This dependence on the reaction targets can be seen in Figure 2.7 for the reaction of a 127 MeV/nucleon  $^{40}\text{Ar}$  with a  $^9\text{Be}$  target (triangles), a  $^{nat}\text{Ni}$  target (squares), and a  $^{181}\text{Ta}$  target (circles). The excitation energies shown in the eight panels increase with the target mass. The fate of the prefragment will depend largely on the amount of excitation energy it has received during the cascading process. The

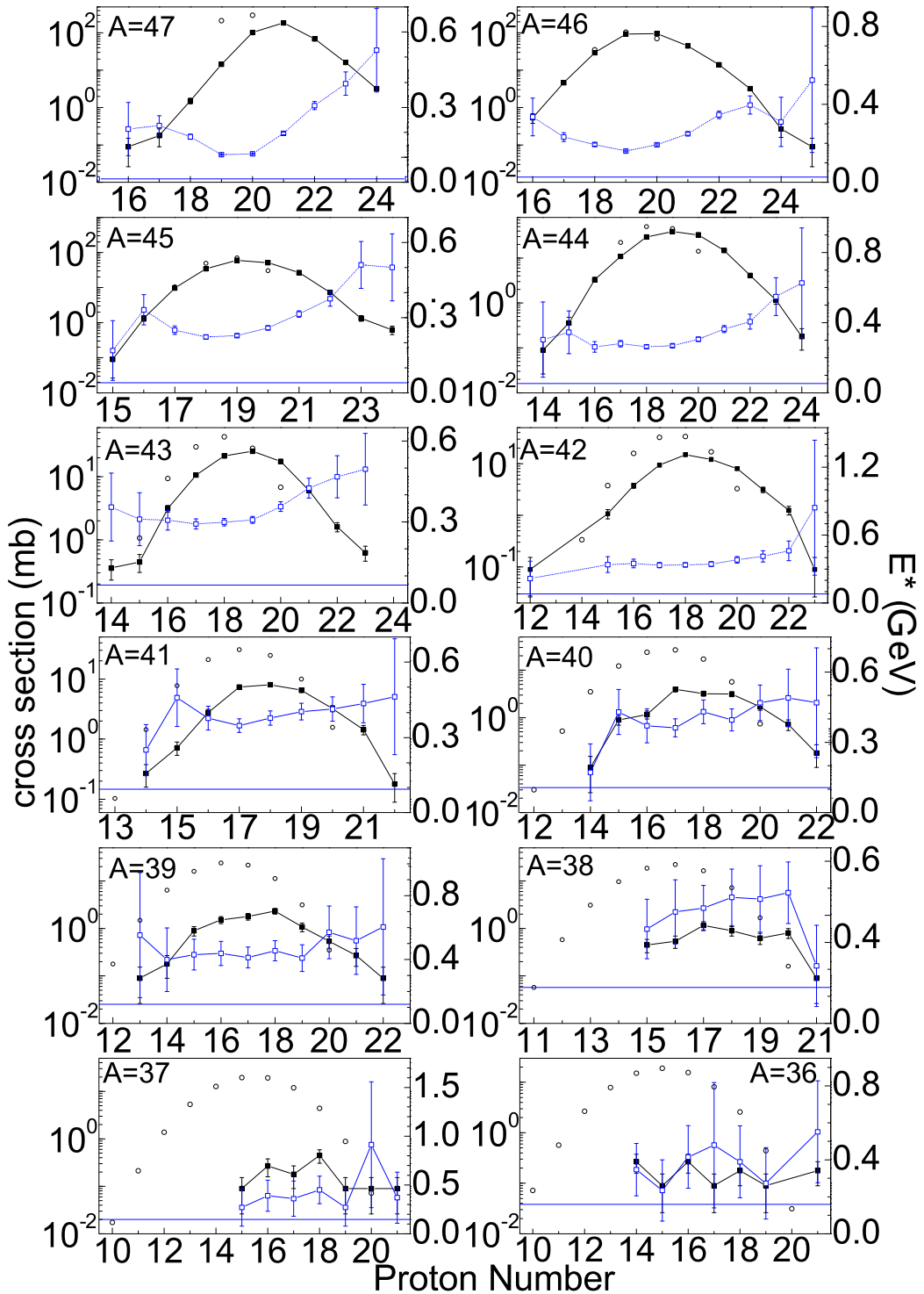


Figure 2.6: The distribution of prefragments from ISABEL (squares) and the ablation-abrasion model in LISE (unfilled circles) produced in the reaction of  $^{48}\text{Ca}$  with  $^{181}\text{Ta}$ . The average excitation energies of the prefragments from ISABEL (unfilled squares) and ablation-abrasion (horizontal lines) that lead to the predicted distributions are also shown. The error bars are statistical and the cross sections are in mb.

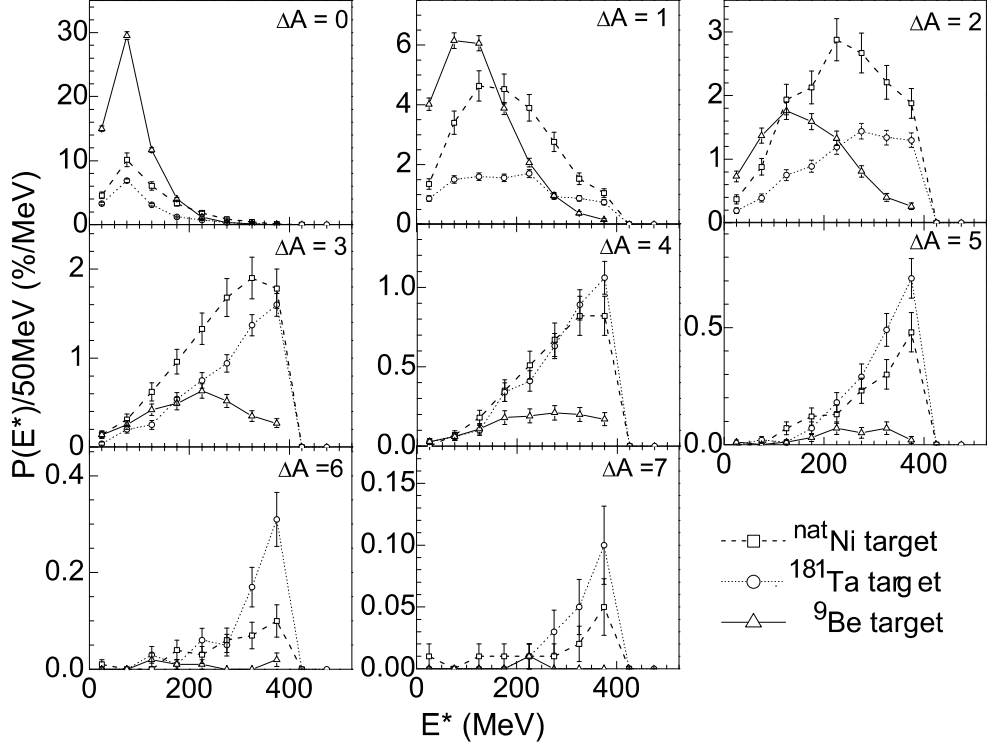


Figure 2.7: The eight panels shows the excitation energies predicted by ISABEL for removing the first seven nucleons from a  $^{40}\text{Ar}$  projectile. The open triangles are the energy probabilities from the reaction with a  $^9\text{Be}$  target, the open squares are from a  $^{nat}\text{Ni}$  target, and the open circles are from  $^{181}\text{Ta}$  target.

excited prefragments de-excite by emission of nucleons and  $\gamma$ -rays in the same manner as in the ablation-abrasion model. The cross sections and velocities of neutron-rich fragments after de-excitation were calculated using the internuclear cascade code ISABEL coupled to a statistical de-excitation code GEMINI [41] and compared with data produced from projectile fragmentation of  $^{40}\text{Ar}$  with  $^9\text{Be}$ ,  $^{40}\text{Ar}$  with  $^{nat}\text{Ni}$ ,  $^{40}\text{Ar}$  with  $^{181}\text{Ta}$ , and  $^{48}\text{Ca}$  with  $^{181}\text{Ta}$  at an intermediate energy of 127 MeV/nucleon (the energy of the projectile at the center of the target).

## 2.4 Deep Inelastic Transfer (DIT) Model

At low energies, it is widely known that nucleon transfer mechanisms are the dominant processes that lead to the production of radioactive nuclei. The transfer mechanism is expected to subside as the kinetic energy of projectile increases due to the increasing

difference between the projectile and target nucleon momenta. The disappearance of transfer mechanism signatures such as the suppression of the yields of masses heavier than that of the projectile (in the case of projectile fragmentation) has been thought to be an indication of the onset of the fragmentation mechanism, while others have argued that these nuclei tend to be highly excited and the suppression of their yields may be the result of evaporative processes that occur to de-excite the nucleus thus reducing the number of observed heavy nuclei [23]. The presence of the transfer mechanisms may result in the dissipation of energy in heavy-ion reactions, which can occur well past the Fermi energy. Many theoretical models that use successive nucleon transfer to excite the nucleus have been produced in attempts to explain results of reactions near the Fermi energy. One such model was developed by Tassan-Got and St  phan [23]. An outline of their model will be given below. The assumptions made by Tassan-Got and St  phan are similar to those in early work by Samaddar et al. [42] with the addition of angular momentum and a friction force. The nucleons in this model are assumed to move in classical trajectories. As one nucleus approaches the other nucleus, a window in the potential barrier opens for stochastic transfer of nucleons (excluding clusters). Pauli blocking reduces the transfer probability to

$$P = \int T \cdot n_d \cdot (1 - n_a) \cdot \Phi d^5\sigma. \quad (2.23)$$

The first term ( $T$ ) is the barrier penetrability including nuclear and Coulomb interactions and is calculated using the Hill-Wheeler formula for a parabolic barrier. The barrier penetrability determines the probability of nucleons to tunnel across the potential barrier. The second and third terms ( $n_d \cdot (1 - n_a)$ ) determines the occupational probability of the donor nucleus ( $n_d$ ) and acceptor nucleus ( $n_a$ ) for a given system in equilibrium. This term is given by

$$n_i = \frac{1}{1 + \text{Exp}[(\epsilon_i - \epsilon_{Fi} - S_i l_i / I) / T_i]} \quad (2.24)$$

where

$i$  = donor or acceptor

$S_i$  = spin of the nucleus

$l_i$  = nucleon's angular momentum with respect to the nucleus  $i$

$I_i$  = the moment of inertia.

Only the components of the angular momentum that are perpendicular to the reaction plane are expected to increase on average with each nucleon transferred and are considered. The final term ( $\Phi$ ) in Equation 2.23 is defined as the one way local phase-space flux and is equal to

$$\Phi d^5\sigma = 2h^{-3}v_x d^3\vec{p} \rho d\rho d\theta, \quad p_x \geq 0 \quad (2.25)$$

where  $\rho$  and  $\theta$  are coordinates used to determine the position of the transferred nucleon with respect to the center of the region of overlap, and  $v_x$  is the velocity in the direction of the other nucleus and perpendicular to the projectile trajectory and  $p$  is momentum of the nucleus. Each trapped nucleon (i.e. particle) or transferred nucleon (i.e. hole) of mass  $m$  makes a particle and hole contribution to the excitation energy equal to

$$\Delta E_p = \frac{m}{2}(v_F + v_{rel})^2 - E'_F - \Delta U, \quad \text{particle excitation energy} \quad (2.26)$$

$$\Delta E_h = E_F - \frac{mv_F^2}{2}, \quad \text{hole excitation energy} \quad (2.27)$$

where  $v_F$  is the transferred nucleon's intrinsic Fermi velocity in the donor nucleus,  $v_{rel}$  is the relative velocity,  $E'_F$  is the Fermi energy of the accepting nucleus after receiving the transferred nucleon and  $\Delta U$  is the potential energy of the composite system. Nucleons will continue to be transferred from one nucleus to the other until the two nuclei move apart from each other after some interaction time  $\Delta t$  has elapsed,

after which time the exchanged nucleons become trapped. The total excitation energy of the nucleus of mass M after all nucleon transfers has occurred is given by the expression:

$$E^* = \int P\Delta E_p dt + \int P\Delta E_h dt \quad (2.28)$$

where P is the transfer probability defined in Equation 2.23.

The product nuclei with the excitation energy from the Monte Carlo DIT code by Tassan-Got have recently been coupled to the statistical de-excitation code GEMINI in order to compare cross sections of fragments from the reaction of a 25 MeV/nucleon  $^{86}\text{Kr}$  beam in a  $^{64}\text{Ni}$  target, a  $^{112}\text{Sn}$  target and a  $^{124}\text{Sn}$  target [43]. The overall agreement of the calculated cross sections with the data at these low bombarding energies indicates the general validity of this approach to produce neutron-rich nuclei. The authors note that the enhancement in the production of the most neutron-rich nuclei with neutron-rich targets is not reproduced by the calculations. They suggest the peripheral collision that creates these nuclei restricts the nucleon exchange to the surface of the neutron-rich target (i.e. the neutron skin) resulting in a preferential exchange of neutrons. This detail related to the neutron skin is lacking from the present model. The cross sections and fragment velocities from the DIT+GEMINI codes will be calculated at an intermediate energy of 140 MeV/nucleon and compared with data from the present work. The results will be described in Chapter 4.

## 2.5 De-excitation and evaporation of prefragments

Once an excited prefragment is created, the nucleus will decay towards a more stable and less excited nucleus. The probability for an excited  $^{A_o}Z_o$  nucleus with spin  $J_o$  to decay to a nucleus with mass  $A_1$ , charge  $Z_1$ , and spin  $J_1$  can be described by the Breit-Wigner resonance formula [44]:

$$P = \frac{2J_R + 1}{(2J_1 + 1)(2J_2 + 1)} \frac{\lambda^2}{(E - E_R)^2 + \lambda^2/2} \quad (2.29)$$

where  $J_R$  and  $E_R$  are the spin and energy of the resonance state and the width ( $\lambda$ ) is defined by Fermi's Golden rule [13]:

$$\lambda = \frac{2\pi}{\hbar} |V'_{fi}|^2 \rho(E_f). \quad (2.30)$$

Equation 2.30 depends on the density of the final states  $\rho(E_f)$  within an energy interval  $dE_f$  and the transition probability

$$|V'_{fi}|^2 = (\int d\nu \Psi_f V' \Psi_i)^2 \quad (2.31)$$

depends the initial and final wavefunctions ( $\Psi_i$  and  $\Psi_f$ , respectively) and on a small perturbation ( $V'$ ) to the nuclear potential that allows the transition to occur.

A variety of evaporation codes are available such as CASCADE [45], PACE [46], and GEMINI [41] that attempt to solve Equation 2.30 analytically. The solution to Equation 2.30 depends on how the transition probability and density of states are defined. Intensive studies have been made to determine the density of states of nuclear matter [47,48]. Bethe demonstrated that the level density of energy independent single particle states of a Fermi gas can be described by an exponential of the form [49]:

$$\rho(U) = \frac{\sqrt{\pi}}{12a^{1/4}U^{5/4}} e^{2\sqrt{aU}}. \quad (2.32)$$

An energy shift ( $\Delta = \chi \frac{12}{\sqrt{A}}$ ) to the excitation energy ( $U$ ) was found necessary in Equation 2.32 in order to account for the pairing effect [50]. For a Fermi gas, the level density parameter ( $a$ ) may be approximated by the semi-empirical function

$$a = \frac{A}{m} \quad (2.33)$$

with  $m$  taken as a variable. This assumption is valid for a large volume homogeneous gas where the effects near the surface can be ignored (i.e. regions where the particle

density is constant) [51]. Higher order effects due to surface energy and shell effects may be included into Equation 2.33 which may have a large influence in the lightest nuclei where there exist relatively few states compared to heavy nuclei. For the purpose of this work, the code GEMINI was used to de-excite the prefragments and higher order effects to the density parameter were neglected.

GEMINI is a statistical de-excitation code developed to track the sequential binary decays of compound nuclei. The decay width ( $\Gamma(Z_o, A_o, J_o | Z_1, A_1, J_1; Z_2, A_2, J_2) = \hbar\lambda$ ) from Equation 2.30 has been modified to include the angular momenta so that the decay width for the evaporation process for light nuclei can be written as

$$\Gamma(Z_o, A_o, J_o | Z_1, A_1, J_1; Z_2, A_2, J_2) = \frac{2J_2 + 1}{2\pi\rho_o} \sum_{l=(J_o-J_1)}^{J_o+J_1} \int_0^{U_2+E_f} d\epsilon \rho_l(U_1, J_1) T_l(\epsilon) \quad (2.34)$$

where the transmission coefficient is defined as

$$T_l(\epsilon) = \begin{cases} 0 & \epsilon < E_{coul} + \frac{\hbar^2 l(l+1)}{2\mu R^2} \\ 1 & \text{otherwise} \end{cases} \quad (2.35)$$

and  $R$  is the absorptive radius, the  $2J + 1$  arises from the degeneracy in the angular momentum and the subscripts 0, 1, and 2 indicate the properties of the initial and final two nuclei. For light particles, the nucleus is assumed to always decay if the difference between the final kinetic energy ( $E_f$ ) and the energy of the Coulomb barrier ( $U$ ) is greater or equal to  $\frac{\hbar^2 l^2}{2\mu R^2}$ . Here,  $R$  is the same absorptive radius for a classical system and  $\mu$  is the reduced mass. The level density for a Fermi gas can be rewritten to include the nuclear spin such that:

$$\rho(U, J) = (2J + 1) \left( \frac{\hbar^2}{2I} \right)^{3/2} \frac{\sqrt{a}}{12U^2} e^{2\sqrt{aU}} \quad (2.36)$$

where  $I$  is the residual nuclei's moment of inertia. A similar Equation for the decay width of heavier nuclei ( $A > 12$ ) can be written by replacing the energy of the Coulomb

barrier with the thermal energy of the saddle point and assuming full transmission over the barrier.

The prefragments calculated by ISABEL produced in the reaction of  $^{40}\text{Ar}$  with  $^{12}\text{C}$  have been deexcited by GEMINI to determine if the final fragment distributions can be correctly predicted. Figure 2.8 shows a comparison of the cross sections from reference [39] (symbols) and ISABEL+GEMINI (histograms). The magnitude and widths of the distributions for the oxygen, fluorine, and neon isotopes in panels (a), (b), and (c), respectively, are well reproduced by ISABEL+GEMINI except for the lightest oxygen isotopes near the proton drip-line. The similar distributions suggest that the two codes of ISABEL and GEMINI may be suitable for describing the production of light neutron-rich nuclei. Thus, the prefragment distributions from ISABEL and DIT have been coupled to the de-excitation code GEMINI to determine if the cross sections from this work can be reproduced and if either codes can give information about the reaction mechanism for light nuclei produced in projectile fragmentation.

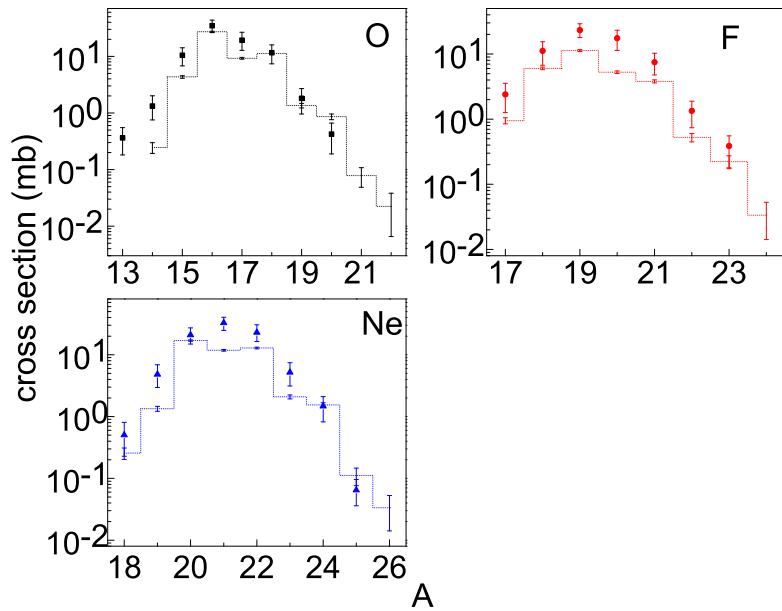


Figure 2.8: A comparison of cross sections for the oxygen, fluorine, and neon isotopes in panels (a), (b), and (c), respectively, produced from the fragmentation of  $^{40}\text{Ar}$  with  $^{12}\text{C}$ . The experimental data (symbols) is from reference [39] and the dashed histograms are the predicted cross sections from simulations made by ISABEL+GEMINI.

# Chapter 3

## Nuclei Near the Neutron Drip-Line

### 3.1 Motivation

The establishment of the limits of stability is one of the major objectives in nuclear physics. The determination of the locations of the drip-lines is a means to test the validity of current nuclear structure theories. Fundamental properties obtained from the study of nuclei near  $\beta$ -stability are expected to change as nuclei become more neutron-rich. For example, possible “tailing” of the nuclear wave function due to the weak binding of the last nucleon(s) allows halo structures to exist [52]. In addition, the levels structure of nucleons in a nucleus described by three dimensional harmonic oscillator wavefunctions, which work well for stable nuclei, may no longer be valid. The spin-orbit interaction, orbital angular momentum ( $l$ ), and the spin angular momentum of nucleons play a significant role in determining the location of a specific energy level and thus influences the locations of the so called “magic numbers”. For example, states with parallel coupling of angular momenta lie significantly below the energies of states with antiparallel coupling. The  $1f_{7/2}$  level is so much lower than the other  $3\hbar\omega$  harmonic oscillator levels that it opens a gap in the level spacing at the  $N = 28$  magic number, see Figure 3.1 (a). It has been suggested that this spin-orbit interaction will decrease in strength near the drip-lines [53]. As another example, unusual filling

patterns allow strong attractive nucleon-nucleon interactions between the protons in the  $j = l + 1/2$  level and neutrons in the  $j = l - 1/2$ . This can result in the shifting of the energy of the levels and the so called quenching of the known magic numbers as shown in Figure 3.1 (a), and the creation of “new” magic numbers such as the one putatively shown in Figure 3.1 (b). Evidence for the changing of the nucleon number’s magicity can be seen in the one-neutron separation energies of isospin chains. The neutron separation energies of ten total isospin chains of nuclei near the neutron drip line are shown in Figure 3.2 as a function of neutron number to determine the locations of possible magic numbers. The separation energies were obtained from the 2003 Atomic Mass Evaluation [54]. For the smallest isospins, the magic numbers 8 and 20 are suggested by the sudden drops in the one-neutron separation energies. As the isospin increases, the disappearance of the magic numbers 8 and 20 and the appearance of a new magic number  $N = 16$  become evident.

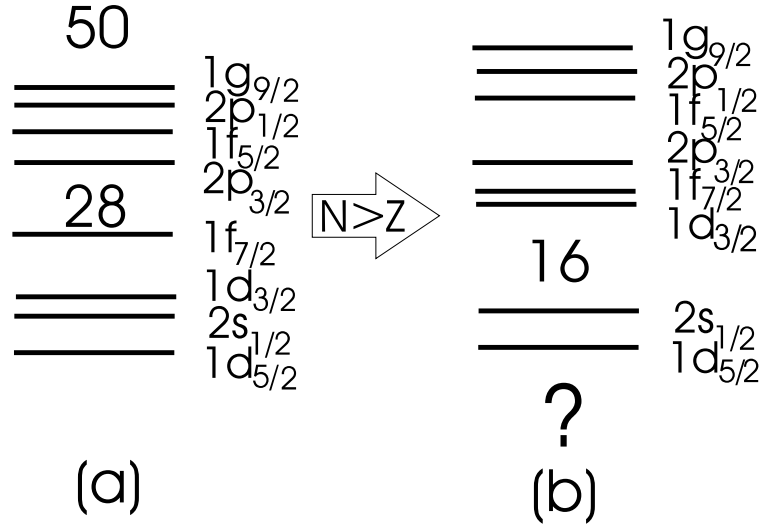


Figure 3.1: Schematic representation of the neutron single particle energy levels for a) nuclei near  $\beta$ -stability and b) a scenario for nuclei away from  $\beta$ -stability.

Much attention has been focused in the region of the drip-line around the predicted  $N = 20$  shell closure because of the apparent disappearance of this magic number for neutron-rich nuclei [56]. An  $N = 20$  shell closure would mean that  $^{28}\text{O}$  should be doubly magic (i.e.  $Z$  and  $N$  are both magic numbers) and should be particle bound.

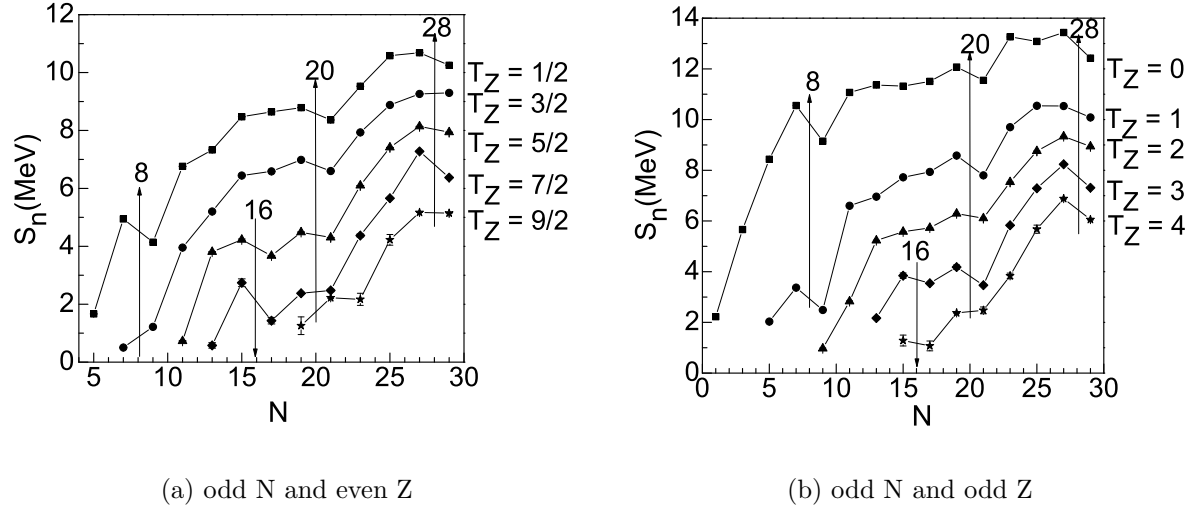


Figure 3.2: One-neutron separation energies from the 2003 Atomic Mass Evaluation [54] for  $T_z < 5$ .

Experiments performed at the NSCL [57, 58] and other facilities [59, 60] failed to observe  $^{28}\text{O}$  and not even  $^{26}\text{O}$  (only even-even oxygen nuclei are expected to be bound near the drip-line due to the added stability from the pairing of like nucleons). The pairing of like nucleons adds stability to a nucleus and thus causes the observed odd-even staggering in the chart of nuclides [61]. Thus,  $^{25,27}\text{O}$  are unlikely to be particle bound and have yet to be observed [62, 59]. The non-observation of these nuclei suggest that  $^{24}\text{O}$  is located along the neutron drip-line of the oxygen isotopes, see Figure 3.3.

The location of the neutron drip-line is of particular interest because it provides a definitive test of the limit of the binding of neutrons to protons. In the late 1990s, Sakurai et al. [10] explored the production of nuclei in the region around the known neutron drip-lines of  $Z \leq 12$ , see Figure 3.4 and the  $^{31}\text{F}$  nucleus was observed for the first time. The rapid change in the number of bound neutrons,  $N = 22$  for  $^{31}\text{F}$  compared to  $N = 16$  for  $^{24}\text{O}$ , with the addition of one proton into the sd shell is surprising and it may suggest the onset of deformation around the  $N = 20$  magic number for nuclei in the vicinity of the neutron drip-line [4, 10]. Utsuno et al. [63] argued that if  $N = 20$  were to remain a magic number, the unbound  $^{26}\text{O}$  and  $^{28}\text{O}$

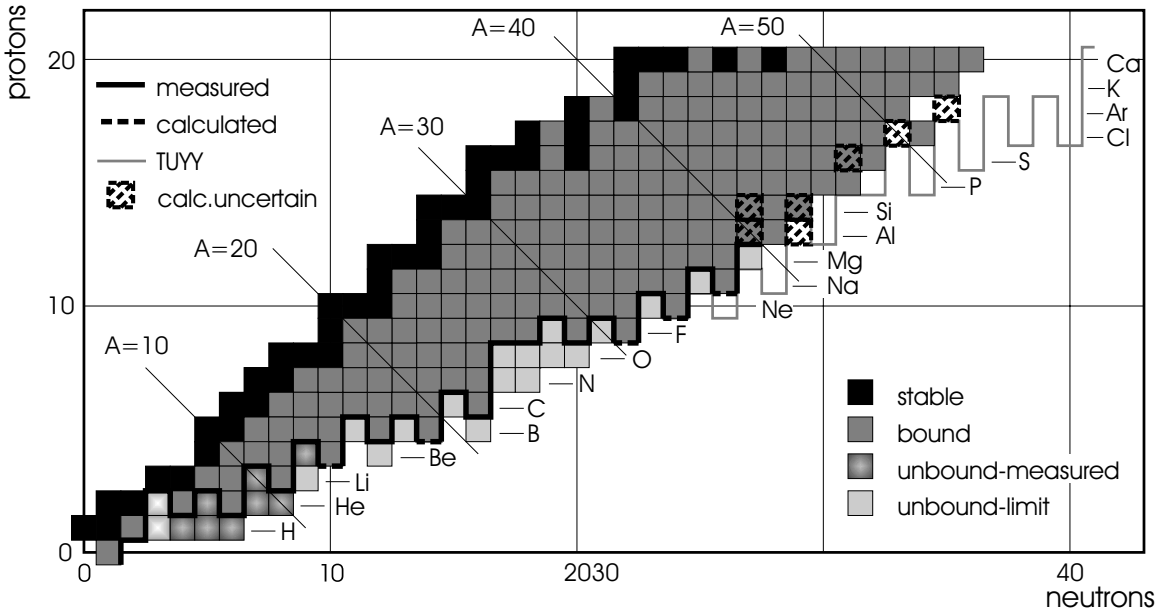


Figure 3.3: The chart of nuclides along the neutron-drip line for  $Z \leq 20$ . The figure is taken from reference [3]. The solid black line is the experimentally determined location of most neutron-rich nuclei of the isotopic chain. The dashed lines are possible locations of drip-line nuclei for a fixed  $N$  based on the uncertainties in the 2003 atomic mass evaluation (2003AME). The dashed boxes are regions where it is unclear whether nuclei may or may not be bounded based on the uncertainties in the 2003AME predictions. The gray boarders labeled TUYY for the authors are the predicted location of the drip-line by Tachibana et al. [55]

isotopes would also require  $^{29}\text{F}$  to be particle unbound.  $^{29}\text{F}$  was first observed in 1989 at GANIL [4], thus  $N = 20$  is unlikely to be a magic number far from stability. Utsuno et al. suggest that an addition of a proton to the  $^{24}\text{O}$  core allows the unbound neutrons in the  $^{26,28}\text{O}$   $1\text{d}_{3/2}$  orbital to be loosely bound in the fluorine isotopes and the additional binding due to the two valence neutron holes in  $^{27}\text{F}$  is lost in  $^{29}\text{F}$  and results in  $^{29}\text{F}$  being unbound. Only through the narrowing of the neutron effective shell gap can  $^{29}\text{F}$  be bound. Models such as the finite range droplet model (FRDM) by Möller et al. [64] and a Hartree-Fock model using a MSK7 interaction by Brown [65] predict  $^{31}\text{F}$  to be the last particle bound fluorine isotope along the neutron drip-line, see Table 3.1 and Figure 3.5. Both models predict that  $^{32}\text{F}$  to be unbound against one- and two-neutron emissions and  $^{33}\text{F}$  to be unbound against two-neutron emission.

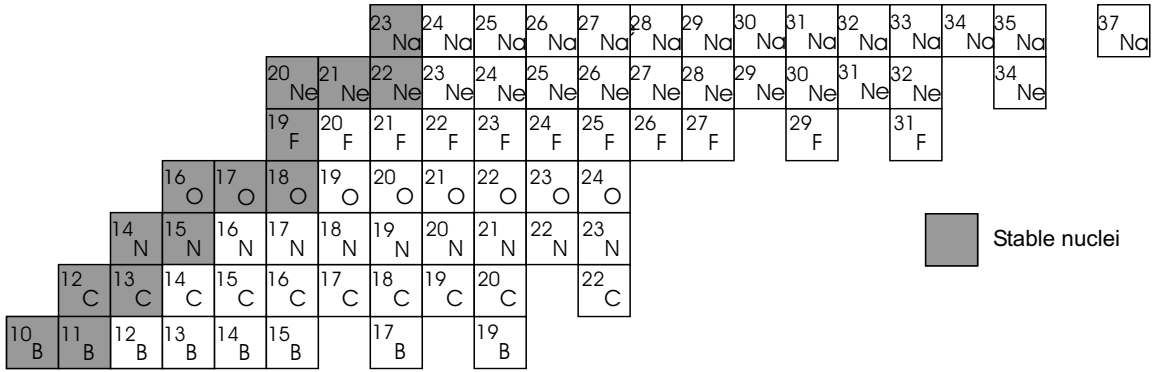


Figure 3.4: The known neutron-rich nuclei from Be to Na are shown.

Table 3.1: Predicted one- and two-neutron separation energies (in MeV) of  $^{31}\text{F}$ ,  $^{32}\text{F}$ , and  $^{33}\text{F}$ .

nuclei	FRDM [64]		HF + MSk7 [65]	
	$S_{1n}$	$S_{2n}$	$S_{1n}$	$S_{2n}$
$^{31}\text{F}$	3.84	2.46	1.95(12)	0.78(12)
$^{32}\text{F}$	-1.76	2.08	-2.2(16)	0.01(23)
$^{33}\text{F}$	-0.57	-2.32	0.75(12)	-1.52(20)

The establishment of the locations of the drip-lines is of such great interest that in 2003, the Nuclear Science Advisory Committee (NSAC) released a report that suggested as one of the milestones in the nuclear physics program should be to determine the locations of the neutron drip-line up to the sodium isotopes ( $Z = 11$ ) by 2007 [66]. Currently, the only method to produce such exotic nuclei and identify the exact location of the drip-lines is projectile fragmentation. The location of the neutron drip-line is only experimentally known up to the oxygen isotopes [3]. As part of the present work, two experiments were performed at the NSCL to measure the production of neutron-rich nuclei by projectile fragmentation from  $\beta$ -stability to the neutron drip-lines near the oxygen and fluorine isotopes and to try to determine the location of the drip-line above oxygen. Experimental results will be presented in Chapter 4.

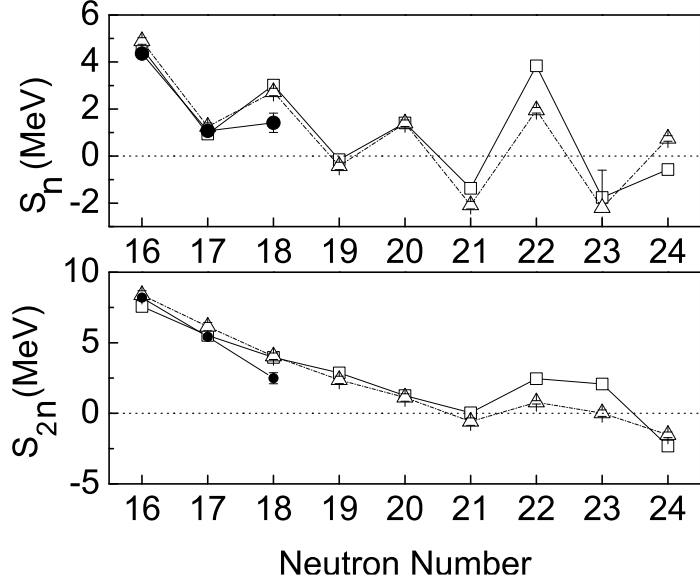


Figure 3.5: The one- and two neutron separation energies of the fluorine isotopes near the neutron drip-line. The open squares and triangles are the predicted one and two neutron separation energy predicted by Möller and Nix [64] and Brown [65], respectively, and filled circles are data from reference [54]. Values below zero (dashed horizontal line) indicate that the nucleus should be unbound.

## 3.2 Experimental Setup

Radioactive nuclei were produced at the NSCL from the fragmentation of  $^{40}\text{Ar}$  and  $^{48}\text{Ca}$  beams. In the first experiment, the  $^{40}\text{Ar}^{18+}$  beam was attenuated by 1/3 the source intensity to about 3.5 electrical nanoAmps (enA) ( $\sim 10^9$  particles per second) and accelerated to 140 MeV/nucleon ( $\beta \sim 0.5 c$ ) using the coupled cyclotrons before fragmenting in three different targets of Beryllium, Nickel, and Tantalum. The target thicknesses were chosen to maximize the production of  $^{31}\text{F}$  and to yield similar energy losses for the fragments of interest. This allowed the same fragments produced in each target to be transmitted through the separator without changing the rigidity settings. The effective thickness of the targets summarized in Table 3.2 were determined from the initial and final energies of the  $^{40}\text{Ar}$  projectile based on the magnetic rigidity used to center the beam at the midpoint of the fragment separator using the Image 2 viewer. A maximum  $\frac{1}{2}$  mm deviation of the beam's centroid to the center of the Image 2 viewer was estimated from photographs of the centered beam. This variation

Table 3.2: The effective thickness of the targets used in the present work.

target	projectile	beam energy (MeV/nucleon)	manufacturer's thickness (mg/cm <sup>2</sup> )	effective thickness <sup>1</sup> (mg/cm <sup>2</sup> )	beam energy at center <sup>1</sup> (MeV/nucleon)
<sup>9</sup> Be	<sup>40</sup> Ar	141	658	668(39)	127.8(12)
<i>nat</i> Ni	<sup>40</sup> Ar	141	767	775(42)	127.8(15)
<sup>181</sup> Ta	<sup>40</sup> Ar	141	1041	1086(53)	127(2)
<sup>181</sup> Ta	<sup>48</sup> Ca	142	1181	1168(57)	127(3)

<sup>1</sup>Calculated using equation 4.3.

was included in the uncertainties listed in Table 3.2. Three target materials were chosen to fragment the <sup>40</sup>Ar projectile in order to investigate the influence of the neutron-excess of the target on the N/Z ratio of fragments. In the high-energy limit of the projectile fragmentation mechanism, the target N/Z ratio does not play any role in the determination of the neutron excess of the products (see for example the EPAX parameterization of the yields). However, at energies near the Coulomb barrier, the target and projectile can rapidly equilibrate their N/Z ratio due to their long interaction time. Large N/Z targets are thought to increase the yields of neutron-rich fragments at intermediate energies due to the re-absorption of nucleons from the participant zone or nucleon-nucleon exchange during the target-projectile collision [29] and the yield is expected to only depend on the targets neutron excess and be independent of the size of the target [67]. The effect of the neutron-excess of the target on the production yields may be determined by studying the extent of products from the interaction of the <sup>40</sup>Ar beam with each of the three targets. Results from the first experiment were used to select the reaction target for the higher intensity production experiment. In the second experiment, a  $\sim 160$  enA <sup>48</sup>Ca<sup>19+</sup> beam was accelerated to 140 MeV/nucleon and fragmented with a <sup>181</sup>Ta target to produce neutron-rich nuclei in the same region as the first experiment. Momentum distributions were again measured and an attempt was made to determine the location of the neutron drip-line above oxygen.

Nuclei produced in the four reactions were separated in-flight based on their mass-

to-charge ratio ( $A/Q$ ) using the A1900 fragment separator [68]. The A1900 is a third generation separator consisting of fifty six superconducting multipole magnets (twenty four quadrupoles, sixteen hexapoles and sixteen octupoles) and four dipoles magnets that can be operated at a maximum rigidity of six Tm [68]. The four dipole magnets are used to select fragments produced in the target-projectile reaction based on the ion's magnetic rigidity ( $B\rho$ ) and the other the magnets were used to focus the beam and correct for aberrations. In the present work, the A1900 was operated as a zero-degree spectrometer. Ions with the correct momentum-to-charge ratio and angular acceptance were transmitted  $\sim 35$  meter downstream to an achromatic focal plane and identified. The A1900 fragment separator was designed to have an angular acceptance of 8 msr. The magnetic field strengths of the dipoles within the A1900 were set to the LISE [8] predicted peaks of the momentum distributions of the fluorine isotopes in the ranges from  $^{22}\text{F}$  to  $^{31}\text{F}$  ( $3.628 \leq B\rho \leq 5.228$  Tm) and  $^{25}\text{F}$  to  $^{32}\text{F}$  ( $4.042 \leq B\rho \leq 5.703$  Tm) for the first and second experiments, respectively. Apertures located at Image 2 and Image 3 limited the momentum acceptance of the separator to  $\Delta p/p = \pm 0.5\%$ , see Figure 3.6. These apertures were opened at the highest magnetic fields to allow particles to be transmitted through the full acceptance  $\Delta p/p = \pm 2.5\%$  of the separator in order to search for the production of the weakest channels:  $^{31}\text{F}$  and  $^{32}\text{F}$ . Particles were tracked and identified using various detectors located at the focal plane. A schematic diagram of the focal plane detectors and their location are shown in Figure 3.7. Five  $5 \times 5 \text{ cm}^2$  Si PIN detectors in the dE telescope with thickness of 980, 966, 1001, 988, and 992  $\mu\text{m}$ , and a 10 cm thick plastic scintillator with an active area of  $15 \times 10 \text{ cm}^2$  were used to measure the energy loss and kinetic energy in order to identify the transmitted particles. A pair of position sensitive parallel plate avalanche counters (PPAC's) with a  $10 \times 10 \text{ cm}^2$  active area and a  $28 \text{ mg/cm}^2$  plastic BC-400 scintillator located at Image 2 were used to track the positions of the ions. The positions measured by the PPAC's located at the front and the back of the focal plane box were previously calibrated with a mask. The two positions of the

fragments measured by the PPAC's were used to determine the angular acceptance at the focal plane. Shown in Figure 3.8 is the horizontal and vertical spatial and angular distributions of fragments produced from the fragmentation of  $^{40}\text{Ar}$  with  $^9\text{Be}$  at the focal plane of the A1900, left and right panels, respectively. The transmitted fragments in both experiments were found to be  $\sim \pm 60$  ( $\pm 15$  mm) and  $\sim \pm 40$  mrad ( $\pm 15$  mm) centered about  $0^\circ$  in the horizontal ( $\theta$ ) and vertical ( $\phi$ ) planes, respectively. Four inch thick copper slits located at the focal plane opened to  $\pm 2.5$  cm about the central beam axis were used during the second experiment to prevent ions from going around the Si dE telescope and triggering the larger focal plane scintillator. This reduced the probability of particles from hitting the edges of the Si telescope where partial charge collection can occur thus increasing the CPU's dead time. No wedges were used at Image 2 in order to avoid any complications that may occur during the study of the projectile fragmentation process. Thus, the Image 2 detector was not used in the first experiment at the 1% momentum acceptance. At full momentum acceptance, the scintillator was inserted to measure the positions of the ions at Image 2. The insertion of the thin Image 2 scintillator resulted in a small wedge effect

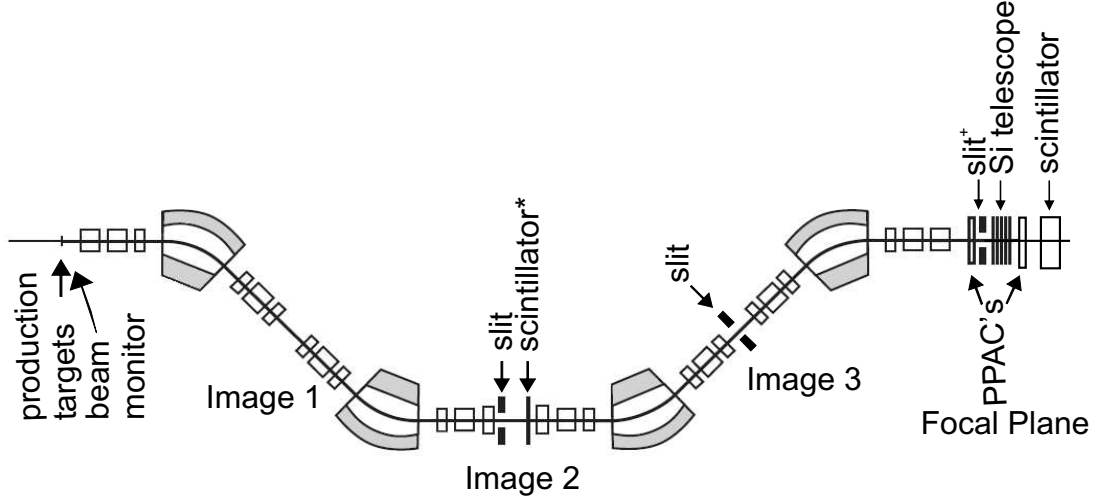


Figure 3.6: Schematic diagram of the A1900 during the two experiments. Fragments travel from the entrance of the spectrometer (left) to the focal plane (right). The small rectangles indicate the positions of the 24 focusing quadrupoles.

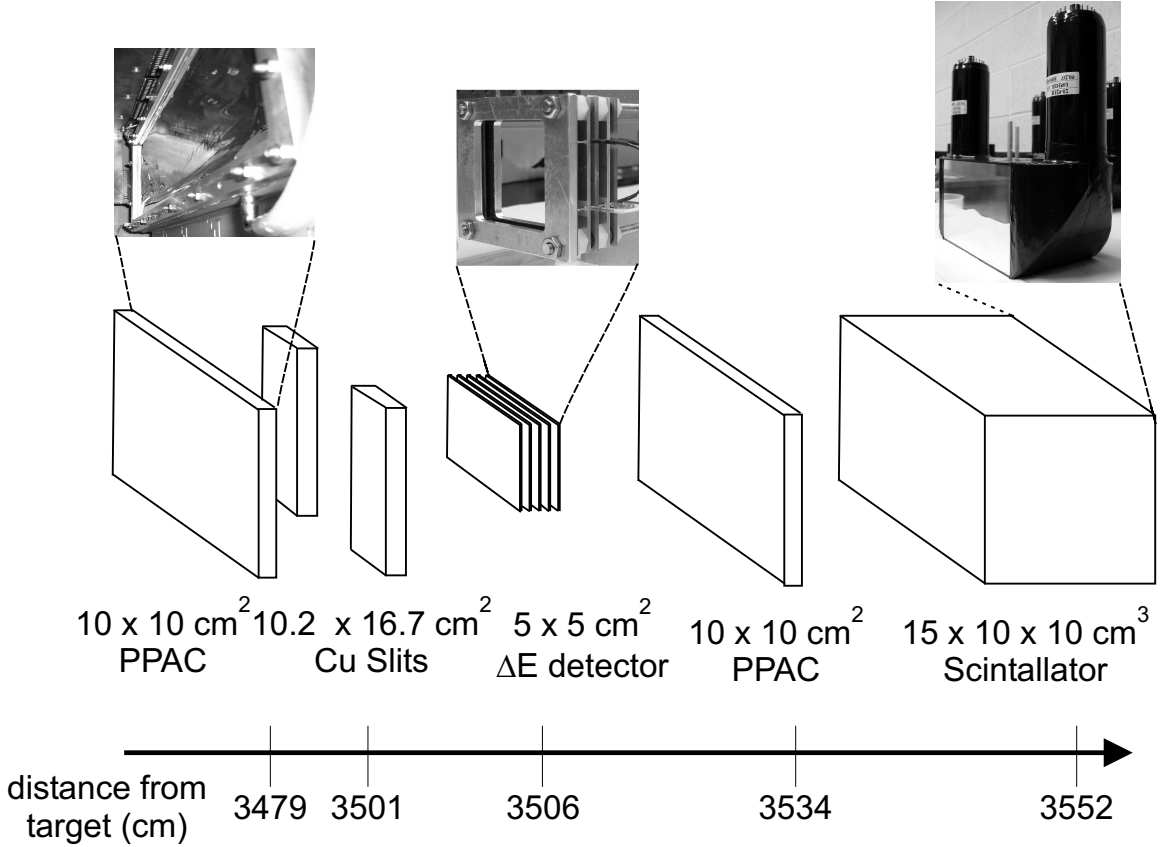


Figure 3.7: The focal plane detectors used during the two experiments. The x-axis is not drawn to scale.

(i.e. small shift in the rigidities of the fragments), but allowed the fragments to be corrected for their different flight paths. The scintillator was left in during the second experiment so that no additional changes to the system were necessary except for the variation to the momentum acceptance.

### 3.3 Electronic System

The standard A1900 electronic setup was used during the two experiments, see Figure 3.9. Fast preamplifiers were used to match the impedance of the detectors to the shaping amplifiers before being recorded for further processing by other electronic modules. Analog-to-digital converters (ADC's) and charge-to-digital converters (QDC's) read the energy signals from the PPAC's, Si detectors, and charge signals from the two scintillators. The time-of-flight (TOF) of the particles through the full  $\sim$

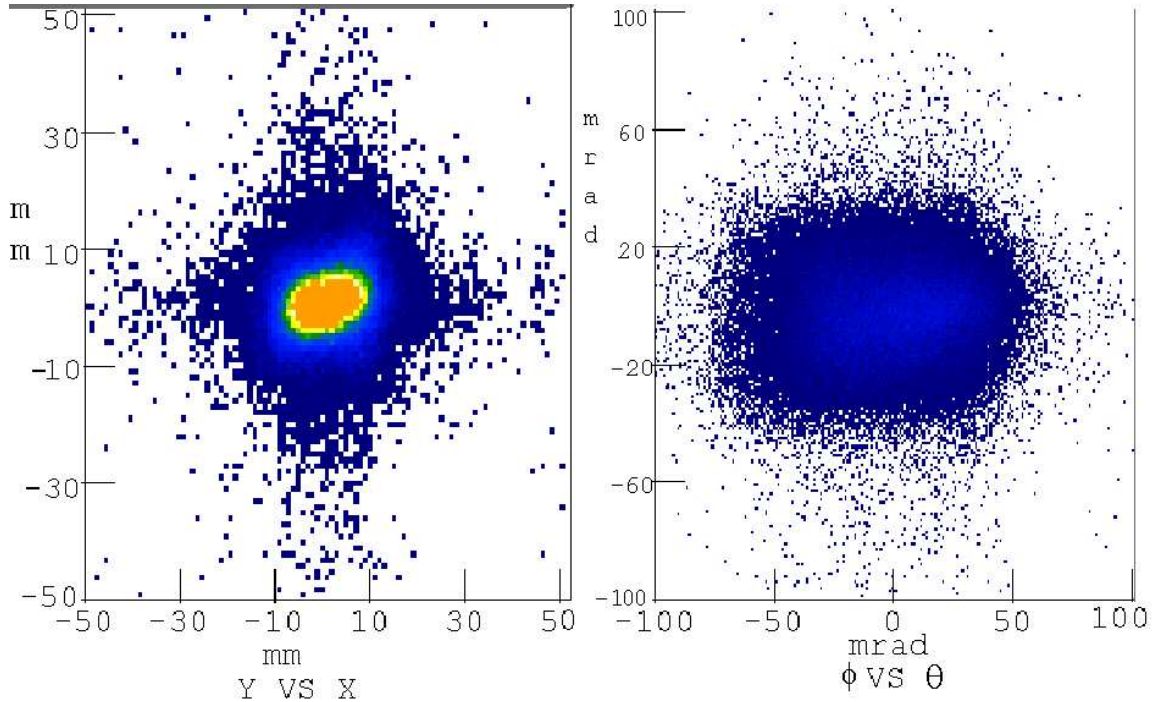


Figure 3.8: The fragment profiles in position and angular phase space at the focal plane of the A1900, left and right panels, respectively.

35 m of the separator (distance from the target to focal plane) and the second half  $\sim$  17.5 m (Image 2 to the focal plane) were measured by four time-to-analog converters (TAC's). The 966  $\mu\text{m}$  Si PIN detector and the 10 cm plastic scintillator each provided start signals for the two TAC's, while the radio frequency (RF) of the cyclotrons and the Image 2 plastic scintillator provided the stop signals for the TAC. In this way, four redundant measurements of the TOF were recorded for each event. The path length of through the entire separator resulted in a  $\sim$  250 ns flight path for the transmitted fragments. This longer path length increased the resolution in the time of flight spectra allowing for mass separation at the largest momentum acceptances of the A1900, but allowed the slowest and fastest fragments to overlap in time-of-flight relative to the cyclotron rf. The RF freq of the coupled cyclotrons (23.1844 and 23.08667 MHz for the  $^{40}\text{Ar}$  and  $^{48}\text{Ca}$  beams, respectively) produced a beam packet every 43 ns. The analysis of the TOF will be discussed in section 3.4. The timing logic pulse from the constant fraction discriminators (CFD's) had a small walk at low pulse heights, visible in the TOF distribution of Figure 3.10. Fragments with the same charge-to-mass

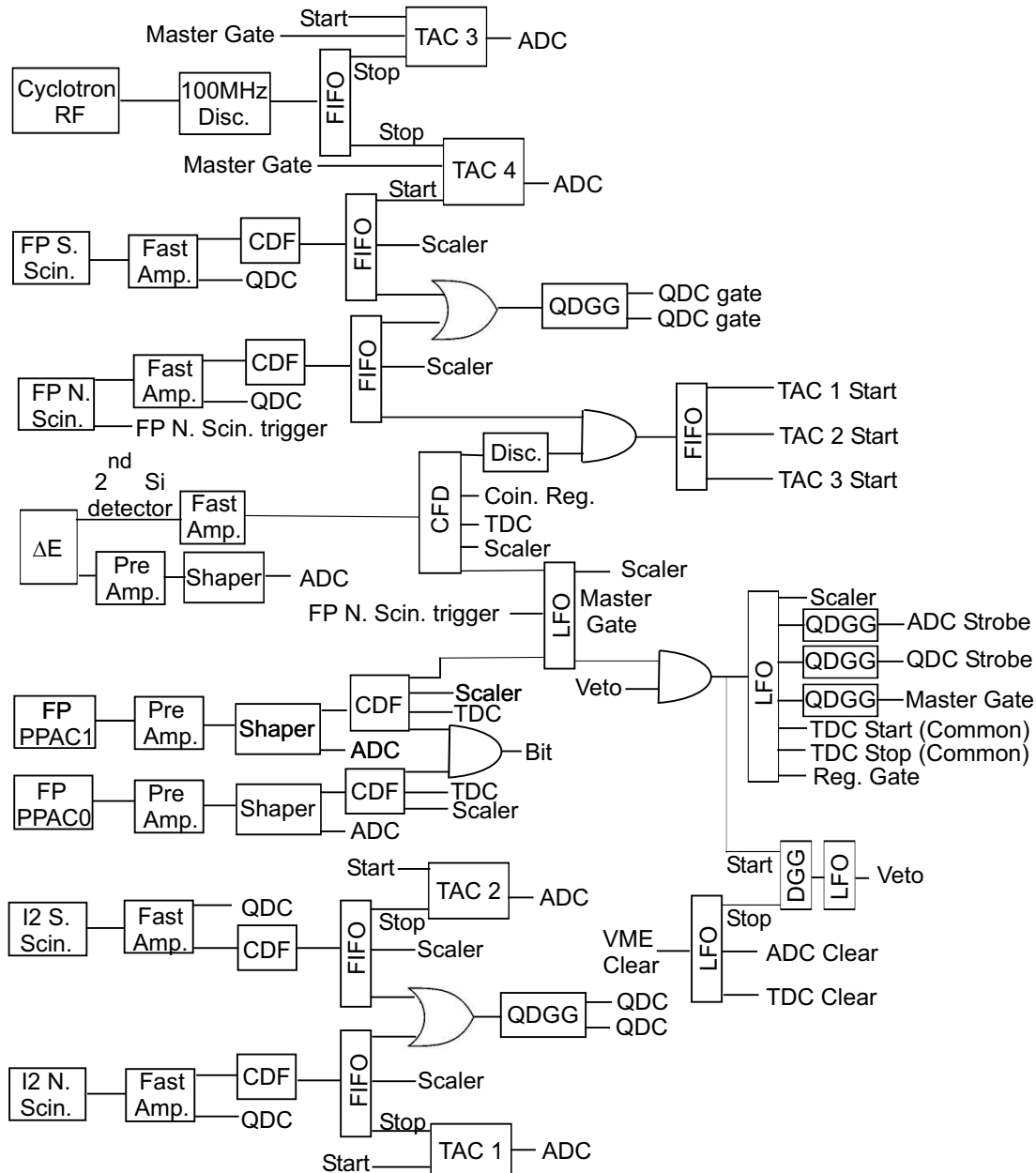


Figure 3.9: Schematic electronics diagram of the A1900 during the two experiments. Acronyms: ADC - analog-to-digital converter, Amp - amplifier, CFD - constant fraction discriminator, Coin. Reg. - coincidence register, Disc - discriminator, FIFO - fan in fan out, LFO - Logic fan out, TAC - time-to-analog converter, TDC - time to digital converter, QDC - charge-to-digital converter, QDGG - quad delay gate generator

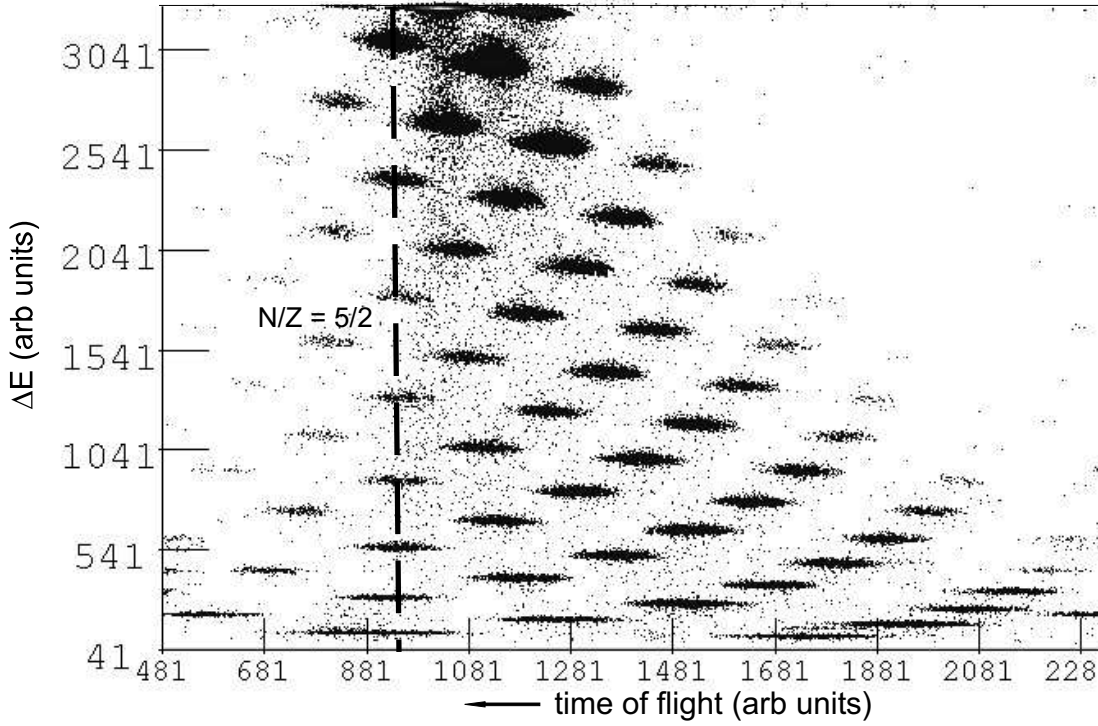


Figure 3.10: The particle identification of fragments the reaction of  $^{40}\text{Ar}$  with  $^9\text{Be}$  at a  $B\rho$  setting of 3.6279 Tm. The walk introduced by the CFD is illustrated in the curvature of the  $N/Z = 5/2$  line at small  $\Delta E$  values.

ratio should have the same TOF through the separator. Thus, the  $N/Z = 5/2$  line (dashed line) should not have any curvature in its time-of-flight. A quadratic function in  $\ln(dE/dx)$  (where  $dE/dx$  is the energy loss) was applied to the TOF in order to correct for this effect, see Figure 3.11. This correction factor was found to hold for all the rigidity settings used in the current work. Information from the ADC's, QDC's and TAC's was written to disk and stored on tape for later analysis. A veto signal present when the CPU was busy limited the data acquisition (DAQ) system in the number of collected events written to file.

### 3.4 Particle Identification

The silicon PIN detectors were used to measure the  $dE/dx$  of the fragments as they traverse through each of the five detectors. The pulse heights from the ADC's were converted to an energy loss assuming a linear function. The expected energy losses

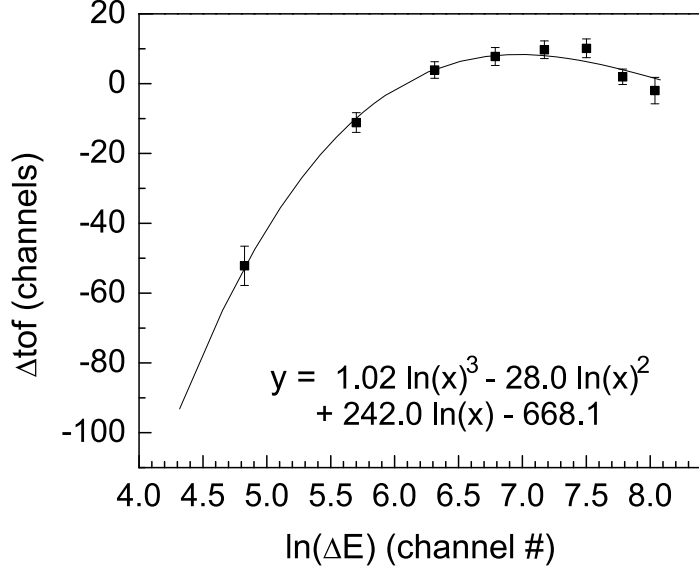


Figure 3.11: Correction to the walk in the tof spectrum introduced by the CFD. The time difference of the N/Z = 5/2 line is relative to the centroid of  $^{40}\text{S}$ .

of the fragments used in the calibration were determined using ATIMA 1.2 with LS-theory [69, 70, 71] in LISE. All of the observed nuclei penetrated into the 10 cm thick focal plane (FP) plastic scintillator due to the large ranges of these light neutron-rich fragments ( $^{31}\text{F}$  has a range of  $\sim 21$  mm in Si under these conditions). Silicon detectors of approximately 1 mm were chosen because large surface area Si detectors are not generally available with thicknesses greater than  $\sim 1$  mm at present. By comparing the  $dE/dx$  measured in a PIN detector with the total kinetic energy signal from the FP scintillator, the charge of the fragments could be determined. Only one charge state of the fragments was observed and this charge state was found to be fully stripped based on the magnetic rigidities and the energy losses.

The proton number (Z) and the mass-to-charge ratio (A/Q) of the ions were calculated on an event-by-event basis using multiple TOF's for the  $\sim 35$  m (timing difference calculated from the RF timing and the second Si detector) and the  $\sim 17.5$  m path lengths (timing difference measured from RF and FP scintillator),  $dE/dx$ 's, and the magnetic rigidities. The particle rates were measured using the TOF's from the RF signals due to the better overall resolution from the longer path length and the

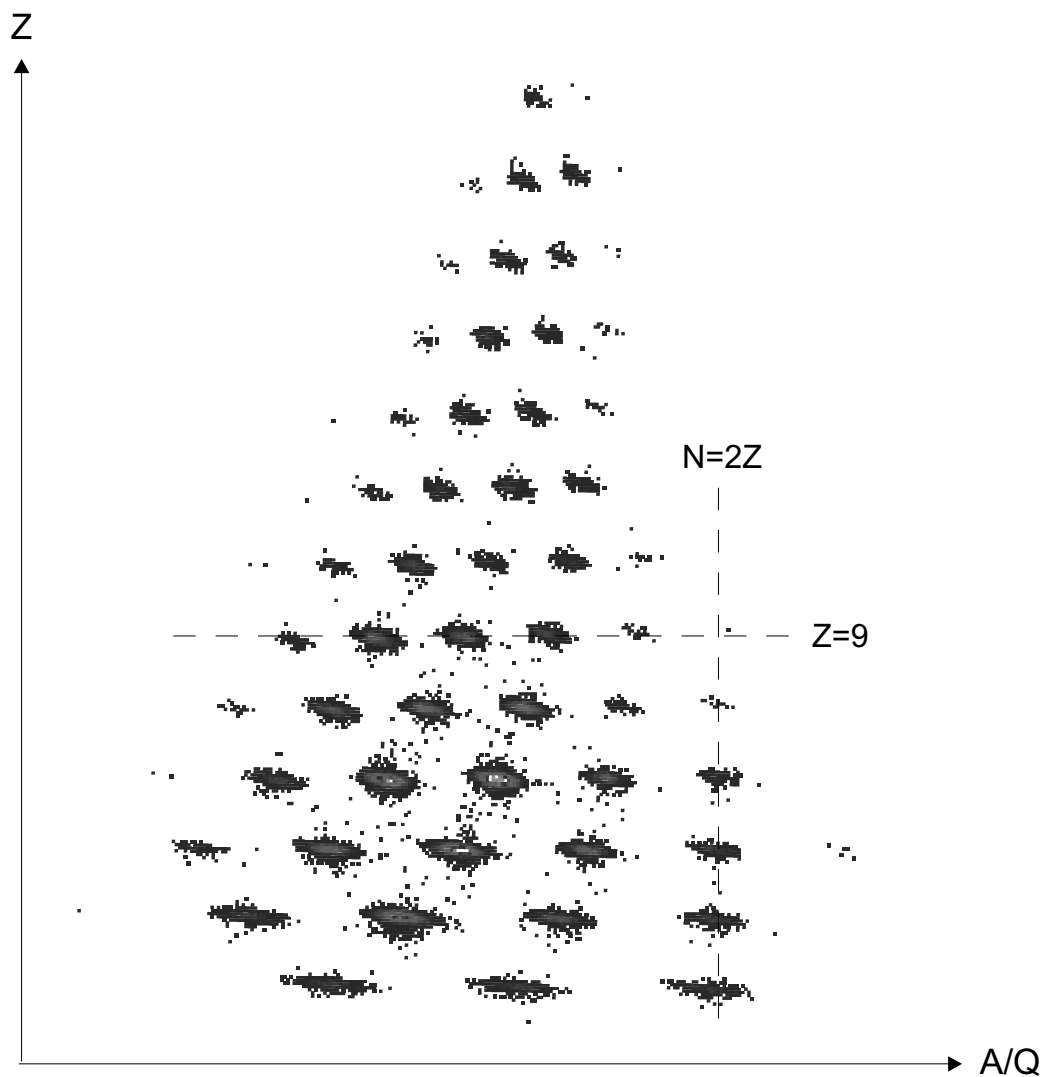


Figure 3.12: The particle identification of neutron-rich nuclei that are transmitted to the focal plane of the A1900 from the reaction of  $^{48}\text{Ca} + ^{181}\text{Ta}$  with  $B\rho_{3,4} = 4.4835$  Tm and  $\Delta p/p = \pm 0.5\%$ .

resolvability of masses at full acceptance. At the lowest rigidities ( $\sim 3.6$  Tm), the time difference between the fastest and slowest fragments produced by the fragmentation of a single beam packet was larger than the flight time of the fastest fragments produced by the fragmentation of the next beam packet. The additional TOF signals from the Image 2 scintillator and the kinetic energy allowed the fastest and slowest fragments in the RF spectra to be resolved. One structure in the particle id spectrum was obtained from the RF by subtracting or adding the time of one RF cycle to the second structure. Time was added or subtracted to the RF TOF depending on which side that the RF signal was relative to the first PID structure in the Image 2 TOF vs RF TOF spectra. The average atomic number and TOF from the last four Si PIN detectors were used to construct a particle identification (PID) plot such as the one shown in Figure 3.12 in order to determine the fragment intensities. The  $N/Z = 5/2$  and  $7/3$  lines in the PID plots were used to identify the isotopes in both experiments. The holes in the PID plots due to the unbound nuclei of  $^{8,13}\text{Be}$  provided additional conformation of the particle's identification. The first detector was used in the calculation of the kinetic energies and to construct software gates to clean the PID but not used in the identification due to the poor resolution of the detector caused by radiation damage. The resolution of the Si detectors can be seen in the widths of the energy loss for the 5600 MeV  $^{40}\text{Ar}$  beam shown in Figure 3.13. The detector resolution summarized in Table 3.3 were determined from the full width at half maximum and the centroid of each Si detector. The resolution from an 8.78 MeV alpha produced from a  $^{232}\text{U}$  source is also listed as a comparison. The resolution of the first detector is approximately two times worse than that of the other detectors. A shim was placed under the Si detectors to lower the detectors by 1 mm in an attempt to avoid the most damaged area on the first detector.

The atomic numbers were obtained from the  $dE/dx$ 's measured by each of the Si detectors using the Bethe-Bloch formula for energy loss in material by heavy ions.

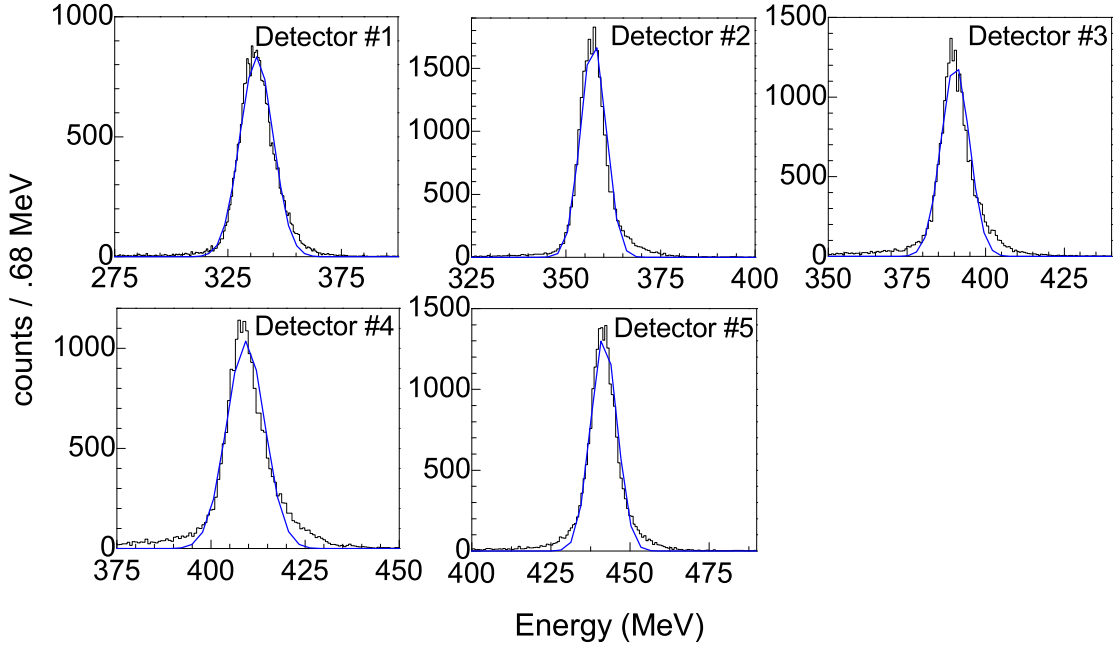


Figure 3.13: The energy deposited in the five Si detectors by a 5600 MeV ( $B\rho = 3.93898 \text{ Tm}$ )  $^{40}\text{Ar}$  beam. The spectra were fitted with a Gaussian (blue curve) to determine the energy resolution displayed in Table 3.3. The thicknesses of the detectors are given in Table 3.3.

Table 3.3: The measured energy resolution of the silicon stack detectors along with the FWHM and the  $\langle \Delta E \rangle^1$  of the energy loss by  $^{40}\text{Ar}$  are given.

Detector no.	thickness ( $\mu\text{m}$ )	$\langle \Delta E \rangle$ (MeV)	FWHM (MeV)	Resolution (%)	Resolution <sup>1</sup> (%)
1	980	337.63(0.05)	7.21(0.13)	5.10(0.04)	2.2
2	966	357.24(0.02)	7.78(0.05)	2.178(0.15)	1.3
3	1001	390.36(0.04)	10.55(0.10)	2.70(0.02)	1.3
4	988	409.24(0.04)	11.93(0.10)	2.92(0.03)	1.3
5	992	441.76(0.02)	9.69(0.06)	2.193(0.13)	1.3

<sup>1</sup>Resolution calculated from a 8.78 MeV alpha produced from the decay of a  $^{232}\text{U}$  source.

The Bethe-Bloch formula can be written in terms of the proton number (Z) as:

$$Z = m \sqrt{\frac{dE/dx}{\beta^2} \cdot (\log(I\gamma^2) - \beta^2)} + b \quad (3.1)$$

where the ionization potential (I) of the stopping material (Si) is  $\sim 0.17$  MeV. The slope m and the offset b are calibration constants determined for each detector. Nu-

clear magnetic resonance (NMR) probes were used to monitor the magnetic field strength ( $B$ ) in each of the four dipoles and to determine the magnetic rigidity of the transmitted fragments. From the Lorentz force equation, it can be shown that  $A/Q$  is related to the magnetic field strength  $B$  (in Telsa) and the particles momentum  $P$  (in MeV/c) via the equation:

$$\frac{A}{Q} = \frac{P}{uc\beta\gamma Q} = \frac{eB\rho}{uc\beta\gamma} \quad (3.2)$$

where  $\rho$  is the radius of curvature of the fragments given in meters,  $e$  is the charge of an electron,  $c$  is the speed of light,  $u$  is the atomic mass unit,  $\beta$  is the relativistic velocity, and  $\gamma$  is the Lorentz factor. The dispersion of the ions due to the variation in momenta causes the fragments to follow different flight paths through the separator. The separator is designed such that a dispersion ( $\Delta x$ ) at Image 2 is related to the spread in the magnetic rigidities ( $\Delta B\rho$ ) via the relation

$$x = \frac{\Delta x}{\Delta B\rho} B\rho = 59 \frac{\text{mm}}{\%} \frac{B\rho}{\Delta B\rho}. \quad (3.3)$$

Using this relationship, the true fragment rigidities were determined. The horizontal position  $x$  of each event was determined using the timing difference between the photomultiplier tubes of the Image 2 scintillator and hence the true rigidity is related to the central rigidity is the along the beam axis  $B\rho_o$  by the following equation:

$$B\rho = B\rho_o \left(1 - \frac{x}{59 \frac{\text{mm}}{\%}}\right). \quad (3.4)$$

Using the corrected rigidities in the mass-to-charge ratio allowed for separation between the adjacent masses at the full momentum acceptance of the separator and provided a particle resolution of  $A/Q$  of  $\sim 0.5\%$  and  $Z$  of  $\sim 1\%$ . For example, Figure 3.14 shows the resolution of beryllium isotopes produced in the reaction of  $^{40}\text{Ar}$  with  $^9\text{Be}$ .

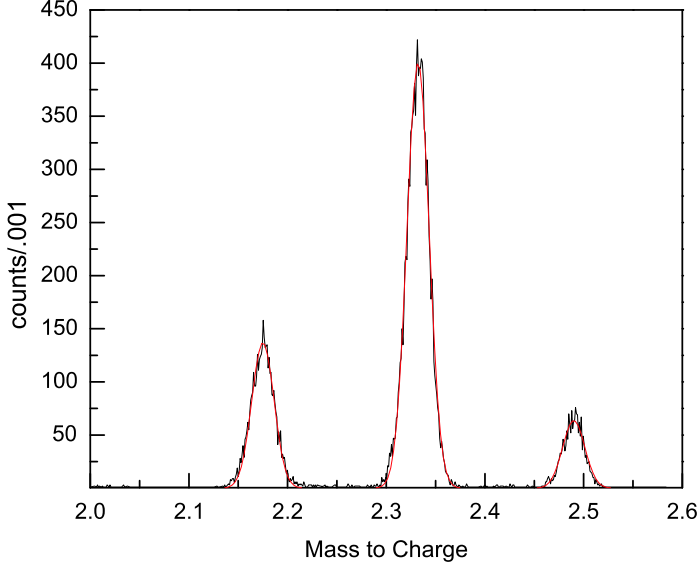


Figure 3.14: The mass resolution of Beryllium isotopes produce in the reaction of  $^{40}\text{Ar}$  with  $^9\text{Be}$  using a rigidity setting of 3.6279Tm.

Software gates were implemented to insure that each event passed through the Si telescope by requiring the fragments had valid angular and spacial distributions that rejected ions with partially deposited charge. The events that fulfilled these requirements were used to determine the fragment yields at each rigidity setting. The yield of the observed fragment ( $Y_F$ ) in the spectrometer can be approximated using the standard formula for thin targets:

$$Y_F = \frac{N}{t\epsilon_\tau I_b \Delta p \epsilon_{ppac}} \int \frac{d\omega}{\Delta\theta_x \Delta\theta_y}. \quad (3.5)$$

where  $I_b$  is the primary beam intensity,  $N/t$  is the number of particles per unit time,  $\epsilon_\tau$  is the fractional live time of the CPU and  $\Delta p$  is the momentum spread. The angular acceptances of the fragments ( $\int \frac{d\omega}{\Delta\theta_x \Delta\theta_y}$ ) were determined to first order using the convolution of a Gaussian and exponential for the parallel-momentum distributions in the simulation program LISE, the solid curves in panels (a) ( $^{40}\text{Ar} + ^9\text{Be}$ ), (b) ( $^{40}\text{Ar} + ^{nat}\text{Ni}$ ), (c) ( $^{40}\text{Ar} + ^{181}\text{Ta}$ ), and (d) ( $^{48}\text{Ca} + ^{181}\text{Ta}$ ) in Figure 3.15. The angular transmission was found to depend mostly on the mass number of the fragment and not the fragment charge. The fragment's angular transmission of the fragments has

been fitted with a fourth order polynomial of the form  $y = P_0 + P_1x + P_2x^2 + P_3x^3 + P_4x^4$  (solid curve). The coefficients from the fits are summarized in Table 3.4.

Simulations using a Monte Carlo code Mocadi [72] were also done in order to include higher order effects to the angular acceptance of the separator. Mocadi is a program that was developed to simulate the transport of heavy ions through matter in optical systems and it calculates the trajectories of ions through an optical system using third order optics. Fragments were assumed to be produced from the fragmentation of an elliptical  $^{40}\text{Ar}$  beam that is confined to  $x^2 + y^2 \leq 0.01$  in x-y coordinate space and  $a^2 + b^2 \leq 25$  in a-b angular phase space, where x and y are in cm and a and b are in mrad. The angular transmission of fragments was determined from the number of events within a momentum acceptance of 0.02% from the central rigidity that reached the focal plane relative to the number of events at the target position. Figure 3.16 shows a comparison of the predicted angular acceptance for fragments produced in the reaction of  $^{40}\text{Ar}$  with (a) $^9\text{Be}$ , (b) $^{nat}\text{Ni}$ , and (c) $^{181}\text{Ta}$  from LISE (filled squares) and Mocadi (first order calculations are the open circles and third order simulations are the filled triangles). The error bars shown in the figure are statistical. The first order simulations from Mocadi using a  $^9\text{Be}$  reaction target tend to be smaller (up to  $\sim 65(29)\%$  less for the lightest fragments) than the angular acceptance from LISE. Third order corrections to the optical transmission were also calculated in Mocadi for a more realistic simulation of the transmission. Large deviations in the angular transmission appears for the heaviest fragments ( $A_P > 25$ ) produced in the reaction of  $^{40}\text{Ar}$  with  $^{181}\text{Ta}$ . The transmission of these fragments is  $\sim 40\%$  regardless of the mass. This behavior has not been seen in simulations using a thinner  $^{181}\text{Ta}$  target. The angular distribution of the fragments at the focal plane from Mocadi using the thickness of the  $^{181}\text{Ta}$  target in this work ( $\Delta\theta_x \sim \pm 35$  mrad and  $\Delta\theta_y \sim \pm 40$  mrad) were found to be smaller than the measured distributions. The same angular distribution was found at the focal plane regardless of the initial beam profile. The angular transmission from LISE was used to correct the differential cross

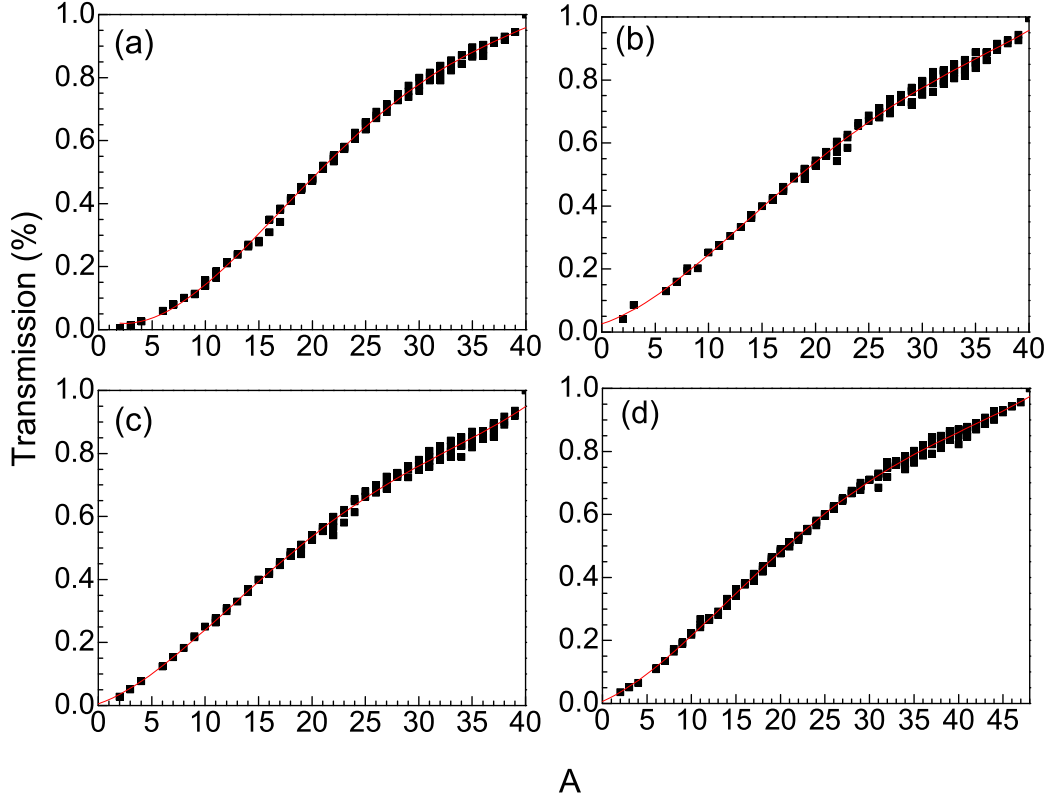


Figure 3.15: The angular acceptance through the A1900 for fragments produced in  $^{40}\text{Ar}$  with (a)  $^9\text{Be}$ , (b)  $^{nat}\text{Ni}$ , and (c)  $^{181}\text{Ta}$  and (d)  $^{48}\text{Ca}$  with  $^{181}\text{Ta}$ . The acceptances are calculated to first order using the simulation program LISE.

Table 3.4: The coefficients for the angular transmission determined from the fits to Figure 3.15.

reaction	$\mathbf{P}_0$	$\mathbf{P}_1$	$\mathbf{P}_2$	$\mathbf{P}_3$	$\mathbf{P}_4$
$^{40}\text{Ar} + ^9\text{Be}$	3.1E-2	-1.4E-2	3.4E-3	-9.5E-5	8.5E-7
$^{40}\text{Ar} + ^{nat}\text{Ni}$	2.6E-2	1.1E-2	1.6E-3	-5.5E-5	5.6E-7
$^{40}\text{Ar} + ^{181}\text{Ta}$	5.2E-3	1.1E-2	1.9E-3	-7.4E-5	8.5E-7
$^{48}\text{Ca} + ^{181}\text{Ta}$	6.3E-3	1.1E-2	1.3E-3	-4.0E-5	3.7E-7

sections due the inability of the Mocadi simulations to correctly predict the angular phase space at the focal plane. Corrections to the optical matrices are currently being done to include higher order effects and to correct for optical abrasions.

The particle rates ( $N/t$ ) were determined from the number of events ( $N$ ) in the  $Z$  vs.  $A/Q$  plots. Losses to the particle yields due to PPAC efficiencies were also included into Equation 3.5 since the PPAC's were the only detectors that did not have a 100% efficiency. Their efficiency was calibrated by determining the number of

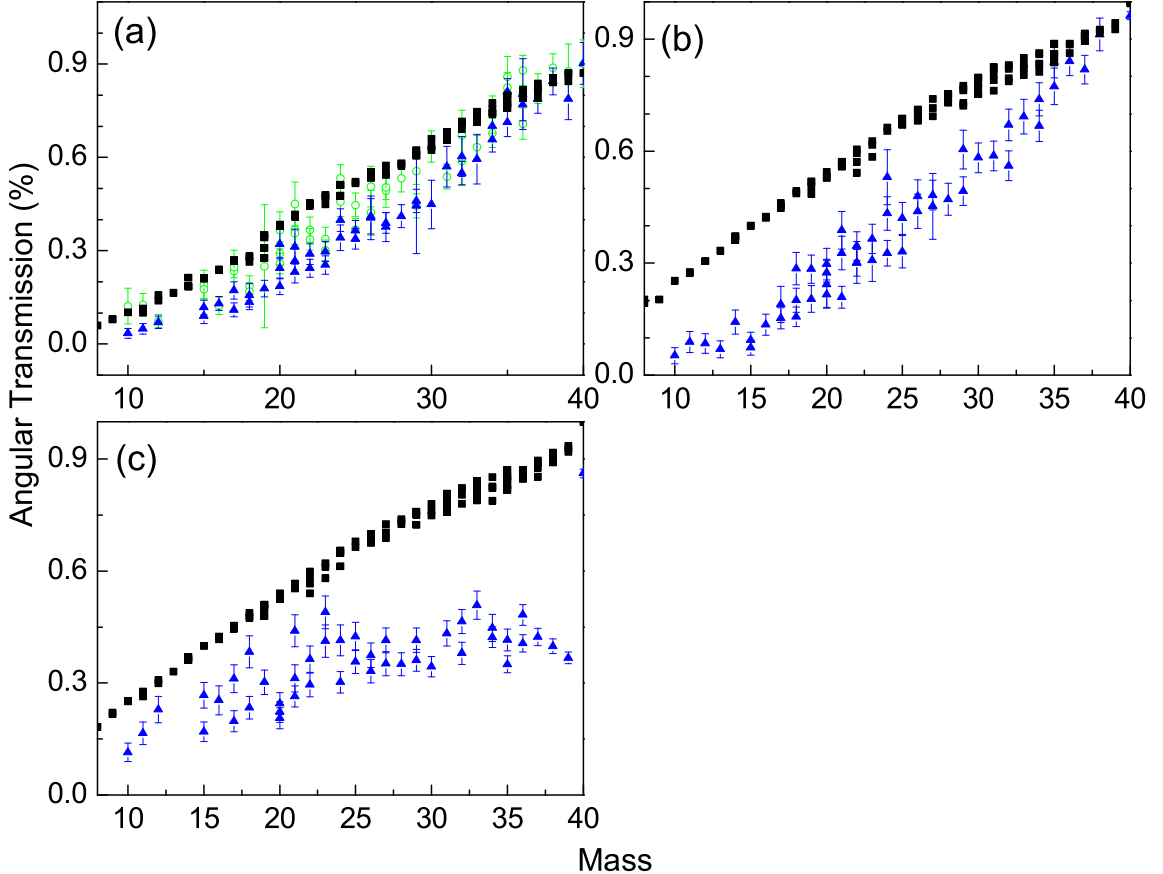


Figure 3.16: Mocadi simulations for the angular transmission of the A1900 separator for the reaction of  $^{40}\text{Ar}$  with (a) $^{9}\text{Be}$ , (b) $^{nat}\text{Ni}$ , and (c) $^{181}\text{Ta}$ . The angular transmission from Mocadi (the open circles are simulations using first order calculations and the filled triangles are simulations using third order corrections) and LISE (filled squares) are shown as a function of mass number.

counts detected in the Si detectors with and without using software gates from the PPAC's. The efficiency ( $\epsilon_{ppac}$ ) was found to depend on the energy and charge of the ions. In the case of the nitrogen isotopes, the efficiency fell to about 55%. Figure 3.17 shows the efficiency of a PPAC as a function of the energy loss as determined by the Born-Bethe equation:

$$-\frac{dE}{dx} = \frac{cAZ^2}{TKE} \quad (3.6)$$

where  $c$  is a constant and TKE is the total kinetic energy of the  $AZ$  ion. The open squares and triangles are the fragment efficiencies at the lowest and highest primary beam intensities ( $I_b$ 's), respectively, and the open stars are the efficiencies at beam

intensity of  $\sim 1.7$  enA. No rate dependence on the efficiency was found. The data was fitted with a Hill function of the form:

$$\epsilon_{PPAC} = \frac{\epsilon_0 (AZ^2/TKE)^n}{k^n + (AZ^2/TKE)^n} \quad (3.7)$$

where k, n, and  $\epsilon_0$  are constants determined from the fit.

A BaF<sub>2</sub> detector located the corner of the target box that was sensitive to various charged particles produced in the target was used to monitor the relative primary beam intensity ( $I_b$ ) as a function of time. The rates measured by the BaF<sub>2</sub> for each projectile-target combination were calibrated against the ion current measured by the faraday cup closest to the target box, see Figure 3.18. Attenuators consisting of four fine wire meshes located in the injection beam line before the cyclotrons with attenuation factors of 3, 10, 100, and 1000 were used in combination to limit the rates on the dE telescope to  $\sim 1500$  particles/second. The linear calibrations in Figure 3.18 are only valid at the highest beam intensities. At the lowest beam intensities (i.e. the attenuation factor  $> 30000$ ), the rates measured by the BaF<sub>2</sub>

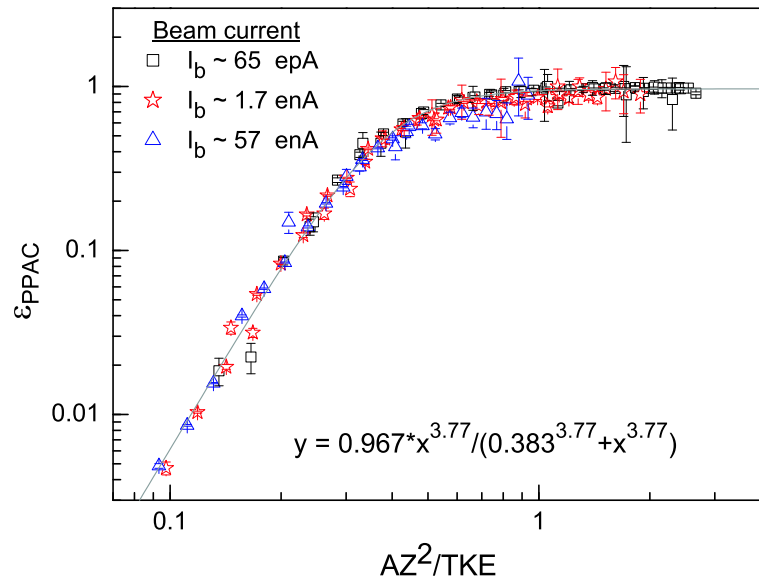


Figure 3.17: Efficiency of the focal plane PPAC's for three beam intensities. The open squares are at the lowest intensity, the open triangles are at the highest intensity, and the open stars at an intensity midway between the highest and lowest intensities.

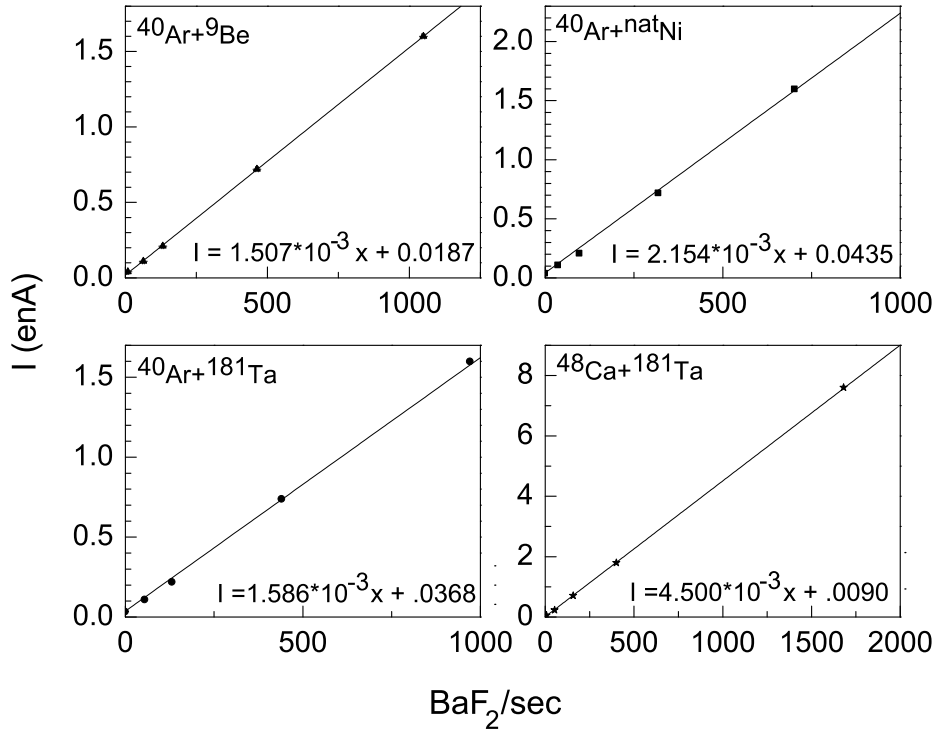


Figure 3.18: Calibration of the primary beam intensities for the four experiments used in the present work.

detector were approximately equivalent to the rates due to background radiation ( $\sim 2 \times 10^{-8}$  pps), thus the linear calibration shown in Figure 3.18 was not valid. The beam currents at these lowest intensities were approximated by dividing the rates from the BaF<sub>2</sub> detector (i.e. back ground current) by a constant that is dependent on the attenuator used in the beam line. The values of the constants were determined by the effect the attenuators should have on the beam current. For example, it was found that changing from a 30k attenuator to a 10k attenuator increased the beam current by 3.5 times, thus the beam current from the cyclotron using a 30k attenuator was scaled down by a factor of 3.5 relative to the beam current from the cyclotron using a 10k attenuator, see Table 3.5. These corrections were only necessary in the first experiment where the 30k, 100k, and 300k attenuators were used.

The momentum distributions of the transmitted fragments were determined from the measurement as a function of  $B\rho$ . Figure 3.19 shows a typical momentum distribution for the fragments observed in this work. The uncertainties in the differential

Table 3.5: Corrections to beam current for low intensities. The beam intensities listed below are relative to the beam current from the cyclotron using a 10k attenuator.

target	30k	100k	300k
<sup>9</sup> Be	3.3(1.3)	8.2(1.1)	30.4(1.7)
<i>nat</i> Ni	3.2(0.2)	8.9(0.2)	-
<sup>181</sup> Ta	3.5(0.2)	12.4(3.1)	43.6(2.0)

momentum distributions include statistical uncertainties as well as systematic errors due to the target thickness, primary beam intensities and fragment transmission. An asymmetric Gaussian (solid curve) was found to describe the distributions well. The parameters from the fit were used to extract information about the reaction mechanism. The fit and parameters will be described in the next chapter.

The isotopic yields of fragments produced by projectile fragmentation were determined using Equation 3.5. The isotopic yields of the fluorine isotopes produced from the fragmentation of a <sup>40</sup>Ar projectile used in first experiment in <sup>9</sup>Be (black triangles), *nat*Ni (blue squares), and <sup>181</sup>Ta (red circles) are shown in Figure 3.20. The fragment yields also include the angular acceptance of the A1900. The points are connected by a solid line to guide the eye. The fluorine fragments were found to have a Gaussian momentum distribution with an asymmetric tail on the low momentum side of the distribution. The momentum distributions of the current work

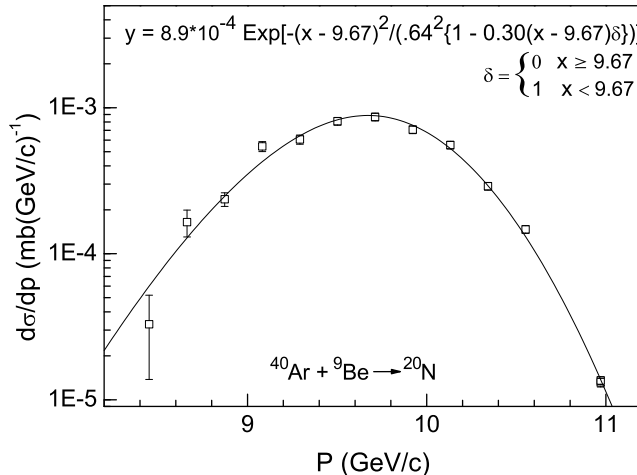


Figure 3.19: The yield of <sup>20</sup>N produced from the reaction of 127 MeV/nucleon <sup>40</sup>Ar with <sup>9</sup>Be. The solid curve is an asymmetric Gaussian fitted to the data.

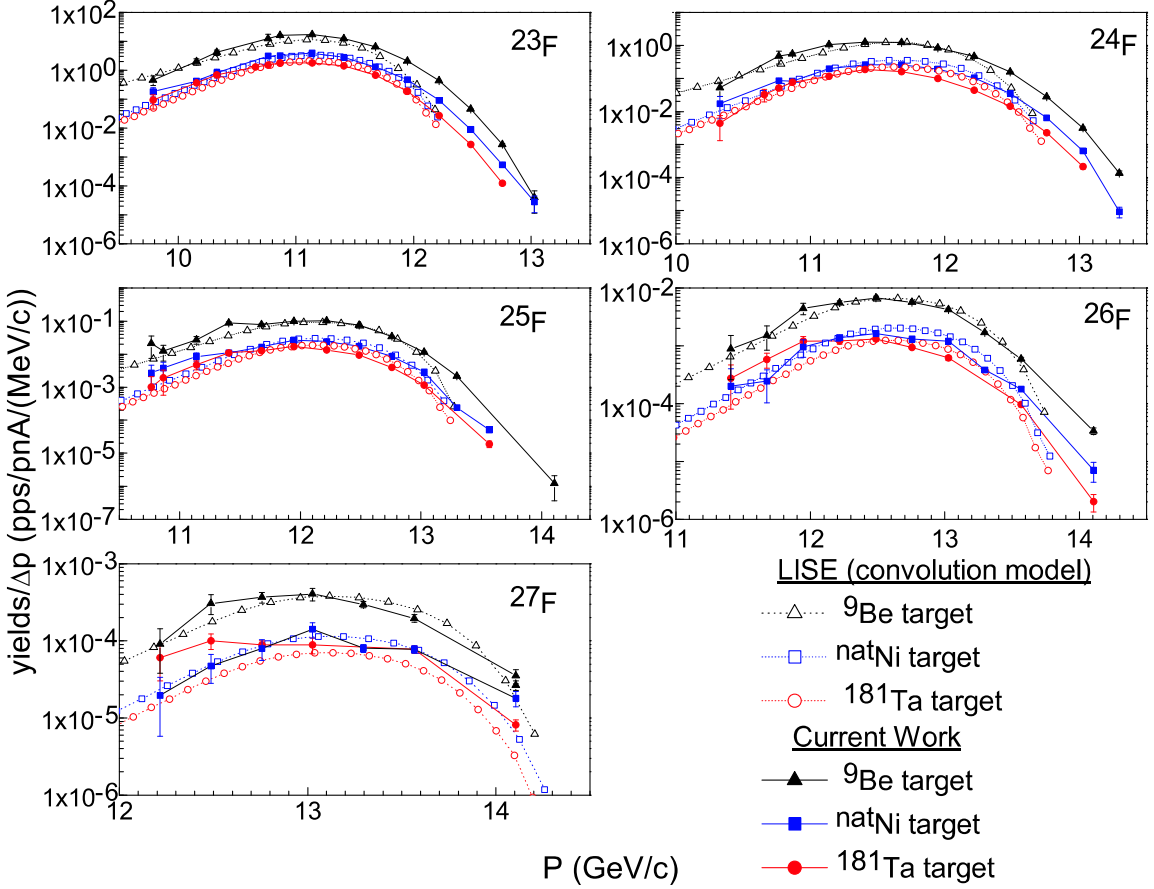


Figure 3.20: A comparison of the momentum distribution of the fluorine isotopes from the reaction of  $^{40}\text{Ar}$  with  $^9\text{Be}$  (triangles),  $^{nat}\text{Ni}$  (squares), and  $^{181}\text{Ta}$  (circles). The open and filled symbols are the momentum distributions predicted by LISE++ using a convolution momentum distribution and the current work, respectively. The lost of particles due to the angular acceptance through the separator is also included.

(filled symbols) are compared with simulations made in LISE++ version 7.4.75 [8] using a convolution model which assumes a Gaussian momentum distribution with an exponential tail on the low momentum side [73] (open symbols). The curves are colored by the reaction target and have the same color code as the experimental data points. The approximate shapes and centroids are reproduced by LISE near the peaks of the distributions, but large deviations appear on the high momentum side. The shapes and positions of the momentum distributions provide important clues into the mechanism that creates these fragments. Various fitting techniques that range from a double Gaussian [74,75] to a variable cutoff percentages on the low

momentum side [76] have been used in the intermediate energy regime in attempts to extract information about the reaction mechanism. For the purpose of this work, the momentum distributions were fitted with an asymmetric Gaussian of the form:

$$y = y_0 \text{Exp} \left[ \frac{-(x - x_o)^2}{2\sigma^2(1 + \frac{\delta a(x_o - x)}{\sqrt{2}\sigma})} \right] \quad (3.8)$$

where the asymmetry factor is defined as:

$$\delta a = \begin{cases} 0 & x \geq x_o \text{ (centroid)} \\ a & x < x_o \end{cases} \quad (3.9)$$

and  $\sigma$  is the width of the Gaussian on the high momentum side. An example of equation 3.8 fitted to data is shown in Figure 3.19. The creation of fragments at different locations within the target results in different energy losses of the projectile and fragment that broadens the observed momentum widths. The effects of this energy straggling must be separated from the measured widths in order to gain an understanding in the reaction mechanism and will be discussed in the next section.

# Chapter 4

## Discussion and Experimental Results

### 4.1 Energy Loss

To produce lighter nuclei than the projectile, the projectile must first interact with a nucleus in the target with some thickness  $t$ . The type of interaction the charged particle undergoes will depend on the impact parameter ( $b$ ) [77]. If the impact parameter is small enough (i.e.  $b \leq R_P + R_t$ ), the projectile will be fragmented into smaller nuclei. These nuclei may also interact with the target to produce other nuclei. The probability of fragments to undergo a secondary interaction can be determined from Beer's Law, see Equation 1.1. Using the geometric cross sections

$$\sigma_{geom}(fm^2) = \pi(1.2\{A_t^{1/3} + A_p^{1/3}\} + 1)^2, \quad (4.1)$$

the probability for fragments to interact somewhere in the second half of the target in the four reactions measured in this work were estimated, see Figure 4.1. At most, 4% of the initial fragments, in the case of  $^{40}\text{Ar} + ^9\text{Be}$ , are lost due to multiple interactions. The cross sections listed in the Appendix C and D were adjusted to

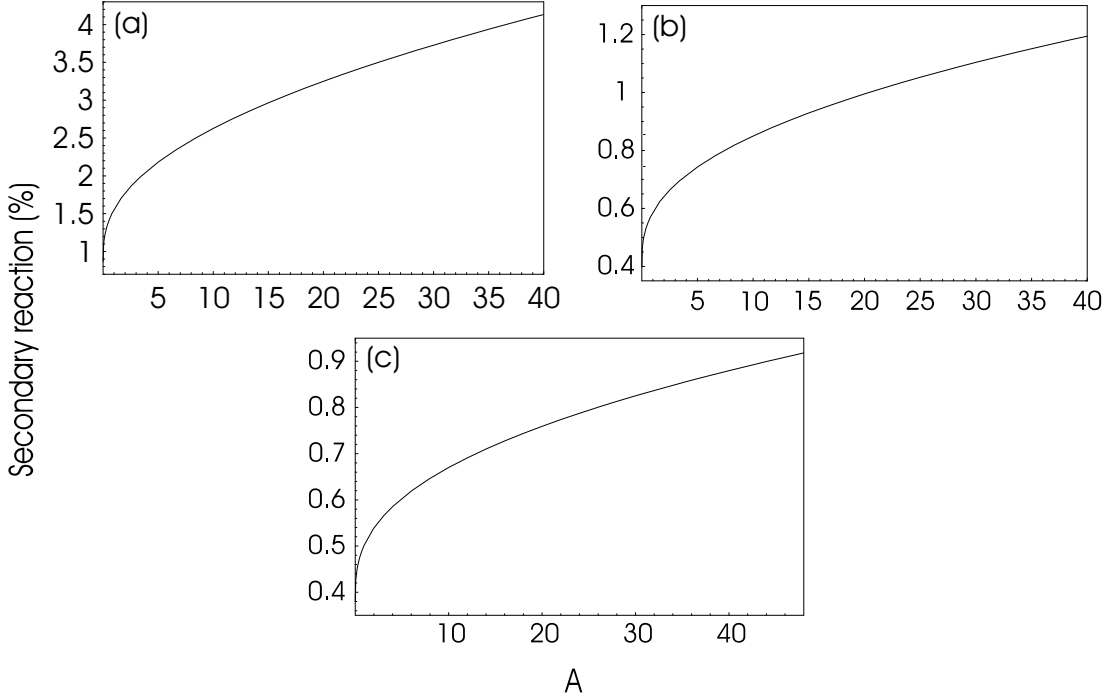


Figure 4.1: The percentage of nuclei that interact twice with the (a) ${}^9\text{Be}$ , (b) ${}^{nat}\text{Ni}$  and (c) ${}^{181}\text{Ta}$  targets are shown as a function of fragment mass number.

include this effect.

Electromagnetic interactions of heavy-ions with material will result in the lost in kinetic energy by bremsstrahlung radiation, excitation, or by ionization [78]. The acceleration of the ions ( $\sim Z_t Z_p e^2 / M_p$ ) due to the Coulomb repulsion with the absorber nuclei will cause the ions to radiate energy by electromagnetic radiation. These inelastic collisions are known as bremsstrahlung [79]. This process is nearly negligible for heavy ions due to the  $M_p^{-2}$  dependence of the energy lost.

If the ion passes close enough to an absorber nucleus, it can interact with highest lying orbital electrons in the absorber nucleus and excite the electrons to higher lying shells. This process is known as excitation. If the energy transferred to the orbiting electrons is larger, electrons attached to the absorbing nucleus can break free and the atom will be ionized. The amount of energy lost by the projectile due to the ionization of the target is dependent on the charge and bombarding energies. In addition to losing kinetic energy, these interactions will deflect the  $Z_p$  projectile by

an angle dependant on its impact parameter:

$$\theta = \pi - 2\text{Arccos} \left( \frac{Z_t Z_p e^2}{b4\pi\epsilon_o \sqrt{1 + (\frac{Z_t Z_p e^2}{b4\pi\epsilon_o})^2}} \right) \quad (4.2)$$

where  $\epsilon_o$  is defined as the permittivity constant and  $Z_t$  is the charge of a target nucleus. The interactions of electrons with matter due to ionization have been studied since the early 1930's [80, 81] and has since been extended to charged heavy-ions in matter. The energy straggling due to the ionization matter has implemented in many codes such as ATIMA [69, 70] and SRIM [82] to predict the characteristics of the interaction such as the energy straggling and stopping-ranges. The average energy loss of ions for the purpose of this work was calculated based on the work of Hubert et al. [83].

Dufour et al. suggested that the convolution of the reaction mechanism and the  $\Delta E$  in the momentum widths can be unfolded by calculating one-half the difference in the energy between those fragments formed at the front and those formed at the back of target [84]. Hubert et al. showed that the energy straggling of an  $A_Z$  ion with energy per nucleon  $E$  can be determined from its range in matter ( $R$ ) and can be parameterized by the function:

$$R(A, Z, E) = k \frac{A}{Z^2} E^\gamma + CA. \quad (4.3)$$

The constants  $k$ ,  $C$  and  $\gamma$  depend on the stopping material. The values for these coefficients for the three target materials used in the present work were determined from fits to the ranges of  $^{19}\text{F}$  in reference [83]. The values of the coefficients found are summarized in Table 4.1. From Equation 4.3, it can be shown that the energy of a fragment formed at a depth  $\delta$  can be expressed as:

$$E(\delta) = E_p(\delta) \left( 1 - \frac{\delta}{R(A_p, Z_p, E_p) - cA_p} - \frac{t - \delta}{R(A_f, Z_f, E_p) - cA_f} \right), \quad (4.4)$$

Table 4.1: The coefficients of the range for  ${}^9\text{Be}$ ,  ${}^{nat}\text{Ni}$ , and  ${}^{181}\text{Ta}$  obtained from fits to the ranges of  ${}^{19}\text{F}$ . The data is from reference. [83].

target	k	$\gamma$	c
${}^9\text{Be}$	5.4(0.2)	1.640(0.007)	-3.3(1.1)
${}^{nat}\text{Ni}$	7.4(0.3)	1.611(0.007)	-3.4(1.1)
${}^{181}\text{Ta}$	11.0(0.4)	1.595(0.006)	-3.6(1.4)

and the energy difference of the fragments with initial energy  $E_f$  can be written as

$$\frac{dE_f}{dx} = \left| \frac{Z_f^2}{A_f} - \frac{Z_p^2}{A_p} \right| \frac{1}{k\gamma E_f^{\gamma-1}}. \quad (4.5)$$

The differential energy loss of ions results in a broadening of the momentum widths and a shift to the centroid. Dufour et al. [84] suggested that formation of fragments at different locations within the target will increase the parallel momentum widths. The contributions to the predicted width of  ${}^{22}\text{O}$  (solid blue curve) due to the energy straggling of the fragment produced at the front (dashed black curve), middle (dotted red curve), and back (dotted dashed green curve) of a  $668 \text{ mg/cm}^2$   ${}^9\text{Be}$  target on the parallel momentum width can be seen in Figure 4.2. For an infinitely thin target, the variance,  $\sigma_N$ , in the momentum distribution is a direct consequence of the statistical nature of the fragmentation process, but the measured widths,  $\sigma_{total}(E)$ , in terms of energy will be altered by an amount:

$$\sigma_{total}^2(E) = \sigma_{dE}^2 + \sigma_N^2(E), \quad (4.6)$$

where the first term is broadening due to the energy straggling of the ions. For thin targets,  $\sigma_{dE}$  is approximately zero, but for thick targets, the different energy loss of fragments formed at the front and back of the target will alter the parallel momentum widths by an amount

$$\sigma_{dE} = c_{targ} \left( \frac{Z_p^2}{A_p} - \frac{Z_f^2}{A_f} \right) \quad (4.7)$$

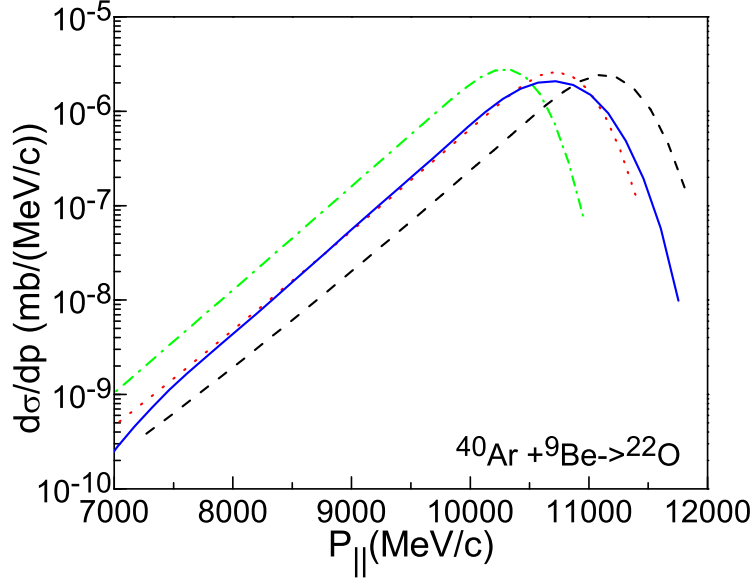


Figure 4.2: The LISE predicted parallel momentum widths for  $^{22}\text{O}$  produced in the fragmentation of  $^{40}\text{Ar}$  with  $^9\text{Be}$  at the front (dashed black curve), middle (dotted red curve) and the back (dotted-dashed green curve) of the target. The solid black curve is the total predicted width.

where  $c_{targ}$  is a constant that is dependent on the target material and thickness, and  $Z_{p,f}$  and  $A_{p,f}$  are the proton number and atomic mass number of the projectile and fragment, respectively. The constant for the four reaction targets used in the current work were determined from linear fits of the LISE predicted  $\sigma_{dE}/(\frac{Z_p^2}{A_p} - \frac{Z_f^2}{A_f})$  vs the average fragment energy, see Figure 4.3. The values of the constants are summarized in Table 4.2.

Table 4.2: The fitted target constants from Figure 4.3.

	$^{40}\text{Ar} + ^9\text{Be}$	$^{40}\text{Ar} + ^{nat}\text{Ni}$	$^{40}\text{Ar} + ^{181}\text{Ta}$	$^{48}\text{Ca} + ^{181}\text{Ta}$
$c_{targ}$	1.245(6)	1.209(5)	1.263(5)	1.415(6)

The broadening due to the fragments energy straggling in the target can have a large effect on the measured momentum widths. The contributions due to the energy straggling from each term can be seen in the example in Table 4.3. The energy straggling of the fragment increased the parallel momentum widths by 143% in the case of  $^{22}\text{O}$  produced by the fragmentation of  $^{40}\text{Ar}$  with a  $668\text{mg/cm}^2$   $^9\text{Be}$  target. Equation 4.4 with  $\delta = t/2$  was used to determine the contribution to the momentum

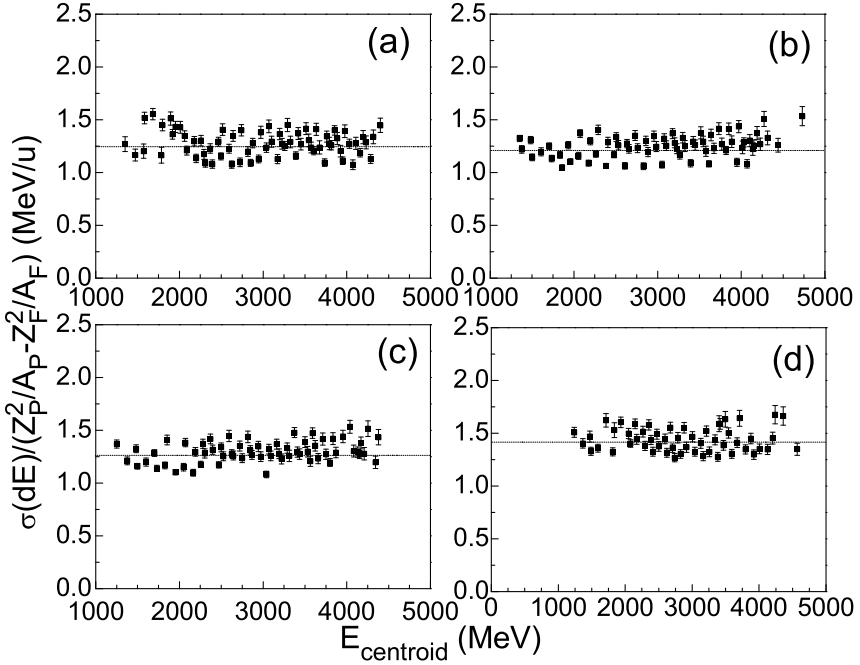


Figure 4.3: The predicted widths due to energy straggling,  $\sigma_{dE}$ , per  $\frac{Z_p^2}{A_p} - \frac{Z_f^2}{A_f}$  for fragments produced in the fragmentation of  $^{40}\text{Ar}$  with (a)  $^9\text{Be}$ , (b)  $^{nat}\text{Ni}$ , and  $^{181}\text{Ta}$ , and (d)  $^{48}\text{Ca}$  with  $^{181}\text{Ta}$  are plotted as a function of the fragments average energy at the back of the target. The horizontal dotted lines are the fitted values for the target constant.

shift due to energy losses in the target. The corrected momentum widths and centroids were analyzed and compared with theoretical predictions in an attempt to give insight into the reaction mechanism and non-observables.

## 4.2 Parallel Momentum Widths

The statistical process that creates the fragments in the fast disintegration process of heavy ions was shown to have a Gaussian momentum distribution [85]. The parallel momentum width ( $\sigma_{||}$ ) of this distribution can give information on how nucleons are removed from the nucleus during the target-projectile interaction. In the early 1970's, Feshbach and Huang attempted to understand the widths of these momentum distributions produced from the sudden emission of nucleons from a nucleus in terms of an "incoherent droplet model" [16]. Nucleons in this model were treated as Fermi

Table 4.3: Contributions to the momentum widths of  $^{22}\text{O}$  produced in the reaction of  $^{40}\text{Ar}$  with  $^9\text{Be}$  due to the energy straggling.

	<b>Lab Frame</b>	<b>Projectile Frame</b>
$E_p$ (MeV/nucleon)	141	0
$\sigma_{total}[P](\text{MeV}/c)$	428(9)	-
$\sigma_{total}[\mathbf{E}](\text{MeV})$	203(7)	-
$\sigma_{dE}(\text{MeV})^1$	144.2(0.6)	-
$\sigma_N[\mathbf{E}] (\text{MeV})$	142(10)	-
$\sigma_N[\mathbf{P}] (\text{MeV}/c)$	311(19)	276(23)

<sup>1</sup>The reduced width calculated from Equation 4.7.

gases with spherically symmetric momentum distributions. They suggested that the momentum width was constant ( $\sigma \sim m_\pi c$ ) regardless of the fragment mass. Later experimental evidence indicated that the momentum width does vary with the fragment mass. Goldhaber showed that the conservation of momentum in the rest frame of the projectile for the statistical process that leads to the emission of a random cluster of  $\Delta A$  nucleons from an  $A_Z$  projectile would naturally lead to a parallel momentum width of

$$\sigma_{||}^2 = \frac{\Delta A(A - \Delta A)\sigma_o^2}{A - 1} \quad (4.8)$$

where the reduced width ( $\sigma_o$ ) is related to the Fermi momentum ( $P_F$ ) via the relationship [86]:

$$\sigma_o^2 = \frac{p_F^2}{5} \quad (4.9)$$

Using the Fermi momentum of  $\sim 260 - 265$  MeV/c from nuclei with nuclear density of  $\rho \sim 0.17$  fm $^{-3}$  from quasielastic electron scattering data, a reduced width of  $\sigma_o \sim 117$  Mev/c is found [87]. Experimentally,  $\sigma_o$  was found significantly smaller ( $\sigma_o \sim 90$  MeV/c) than the reduced width predicted using the Fermi momentum for relativistic bombarding energies. Goldhaber suggested that the difference may be the result of lower  $P_F$  at the nuclear surface for very light or very fragments and that medium mass fragments are likely to have larger than average nucleon momenta. Other authors attribute the lower  $\sigma_o$  value to nuclear and quantum effects such Coulomb repulsion and

Pauli exclusion that are not taken into account in Goldhaber's simple model [88,89]. It has also been suggested that value of the reduced width predicted using the Fermi momentum should be attributed the prefragments distribution [37]. The reduced width has been measured for a variety of reactions at different bombarding energies. Figure 4.4 shows a log-log plot of selected values of  $\sigma_0$  found in literature (unfilled symbols) [90] - [91] for a wide range of projectile energies. These widths appear to depend strongly on the bombarding energy of the projectile. At low energies ( $E/A < 30$  MeV/nucleon), the values of the reduce widths decrease rapidly. At these energies, the fragmentation process is no longer the dominate method in producing the nuclei and the transfer process that creates these nuclei can result in the smaller value for the reduced width. At higher energies ( $E/A > 85$  MeV/nucleon), the experimental values of the reduced widths appear to be approximately constant. This variation of the reduced width with the bombarding energies is not consistent with Goldhaber's

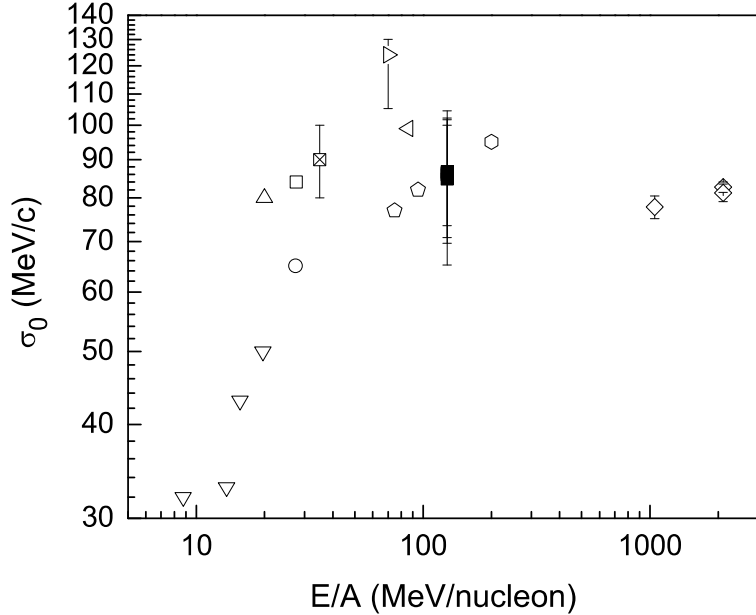


Figure 4.4: The reduced widths of selected reactions found in literature is plotted a function of the bombarding energy. The reduced widths are measured from the following reactions:  $^{197}\text{Au}(^{9}\text{Be},^{7}\text{Li})$  [90](○),  $^{197}\text{Au}(^{9}\text{Be},^{16}\text{O})$  [92](△),  $^{16}\text{O}(^{9}\text{Be},\text{X})$ ,  $^{16}\text{O}(\text{CH}_2,\text{X})$ ,  $^{16}\text{O}(^{12}\text{C},\text{X})$ ,  $^{16}\text{O}(^{27}\text{Al},\text{X})$ ,  $^{16}\text{O}(^{208}\text{Pb},\text{X})$ ,  $^{12}\text{C}(^{9}\text{Be},\text{X})$ ,  $^{12}\text{C}(\text{CH}_2,\text{X})$ ,  $^{12}\text{C}(^{12}\text{C},\text{X})$ ,  $^{12}\text{C}(^{27}\text{Al},\text{X})$ , and  $^{12}\text{C}(^{208}\text{Pb},\text{X})$  [93](◇),  $^{40}\text{Ar}(^{68}\text{Zn},\text{X})$  [94](□),  $^{22}\text{Ne}(^{93}\text{Nb},\text{X})$  [95](▣),  $^{12}\text{C}(^{9}\text{Be},\text{X})$  and  $^{13}\text{C}(^{9}\text{Be},\text{X})$  [96](○),  $^{84}\text{Kr}(^{197}\text{Au},\text{X})$  [97](○),  $^{12}\text{C}(^{12}\text{C},^{7}\text{Be})$  [98](▷),  $^{86}\text{Kr}(^{27}\text{Al},\text{X})$  [99](▷),  $^{208}\text{Pb}(^{16}\text{O},^{12}\text{C})$  [91](▽), present work (■).

model. It has been suggested that decreasing values of the observed width at low energies may be the result of distortions due to the Coulomb force that alter the fragment velocities [88]. At high energies, the Coulomb distortions become insignificant and thus should not affect the reduced widths. The value of the reduced width may be altered if the nucleons were removed over the total interaction time instead of simultaneously. Morrissey suggested that the sequential evaporation of  $A_P - A_F$  nucleons would lead to a width equal to [100]:

$$\sigma_{\parallel} = \sigma_o \sqrt{A_P - A_F} \quad (4.10)$$

where  $\sigma_o$  is taken to be equal to 85 MeV/c.

The momentum widths in the projectile frame for the high momentum side of the Gaussian distribution for fragments produced in the reactions of  $^{40}\text{Ar}$  in a)  $^9\text{Be}$ ,  $^{nat}\text{Ni}$ , and  $^{181}\text{Ta}$  and b)  $^{48}\text{Ca}$  in  $^{181}\text{Ta}$  are shown in Figure 4.5 and are listed in Table 4.4. The widths were corrected for energy straggling using Equations 4.6 and refenergylosswidth. The predicted widths from the sequential evaporation of nucleons assuming a reduced width of 85 MeV/c are plotted using dashed curves. The behavior of the momentum widths for large mass losses from the current experiment (filled symbols) is not reproduced by the sequential evaporation of nucleons model, but the momentum widths in all four cases are more consistent with the parabolic distribution predicted from the simultaneous emission nucleons and the simulated widths from ISABEL+GEMINI (open circles). The parallel momenta were fitted using Equation 4.8 (solid curves) to determine the value of the reduced width. The dotted curves represent the standard deviation values of the reduced width. The predicted widths from ISABEL+GEMINI agree with the data within the uncertainties of the parallel momentum widths from the current work. The values of the reduced widths from the current work are listed in Table 4.4 and were found to lie in a range between 70 - 105 MeV/nucleon. These values are independent of the target and

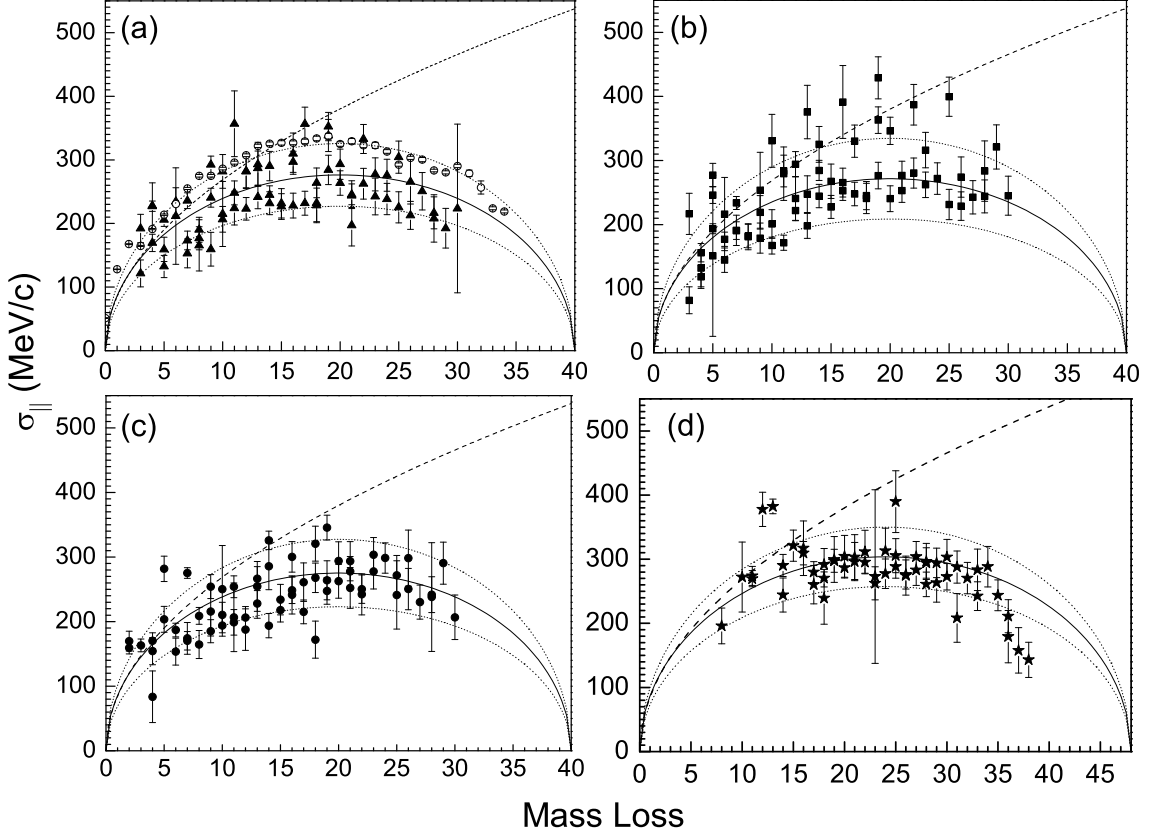


Figure 4.5: The parallel momentum widths from the reaction of  $^{40}\text{Ar}$  in (a) $^{9}\text{Be}$ , (b) $^{nat}\text{Ni}$ , and (c) $^{181}\text{Ta}$  and (d)  $^{48}\text{Ca}$  in  $^{181}\text{Ta}$ . The dashed curves are the predicted momentum widths from a sequential emission of nucleons model using  $\sigma_o = 85 \text{ MeV}/c$  and the solid and the dotted curves are the fitted widths  $\pm\sigma$ , respectively, assuming a single emission of particles. The unfilled circles are the simulated widths from ISABEL+GEMINI.

projectile and are consistent with the literature values found for high bombarding energies, see the filled squares in Figure 4.4.

### 4.3 Parallel Momentum Transfer

The collision between the projectile and target nuclei results in a transfer of momentum to the nucleons. If the nucleons gain enough energy, they may break free of their potential well and escape, otherwise, the nucleons will remain bound to the nucleus dissipating their energy through collisions with other nucleons [38]. This interaction will alter the mean nuclear velocities of the prefragments. The changes in the ve-

Table 4.4: The reduced widths deduced from the present work.

	$\sigma_o(\text{MeV}/c)$ ( $^{40}\text{Ar}+^{9}\text{Be}$ )	$\sigma_o(\text{MeV}/c)$ ( $^{40}\text{Ar}+^{nat}\text{Ni}$ )	$\sigma_o(\text{MeV}/c)$ ( $^{40}\text{Ar}+^{181}\text{Ta}$ )	$\sigma_o(\text{MeV}/c)$ ( $^{48}\text{Ca}+^{181}\text{Ta}$ )
<b>sequential emission</b>	85	85	85	85
<b>simultaneous emission</b>	86(15)	85(20)	86(16)	87(13)
$P_F (\text{MeV}/c)$	193(34)	190(44)	192(36)	194(30)

locities that may arise from the breaking of the nuclear bonds to remove nucleons during the fragmentation process has been attributed to a friction phenomenon [101]. Nucleons receive a "kick" or transfer of momentum  $\mathbf{q}$  in the projectile rest frame during the projectile-target interaction. These nucleons may escape from the potential well of the nucleus with momentum  $\mathbf{q}'$ . Abul-magd et al. [101] suggested that the momentum gained in the transverse direction by a fragment is proportional to the momentum transferred. On average, there is no net contribution to the perpendicular component of the observed momentum distribution due to the equal probability of the projectile to interact on either side of the target nucleus (i.e.  $-(R_1 + R_2) < b < R_1 + R_2$ ). The parallel momentum transfer has been described by the equation:

$$\langle p_{||} \rangle = \frac{\Delta E}{c\beta} [1 + k(1 - \beta)^{1/2}], \quad (4.11)$$

where  $\Delta E$  is the energy transferred to the prefragment and the constant  $k$  ( $=\delta m/m_p$ ) is the rate at which the  $\langle p_{||} \rangle$  changes with the projectile velocity ( $\beta$ ) [102], see Table 4.5. The value of  $k$  varies for the different models. For proton-induced reactions, a value of  $k$  equals one is predicted from a collective tube model (CTM), while a  $k$  value of zero is obtained from a single fast neutron model (SFNM). It was also shown that

Table 4.5: A summary of the values for the parameters in Equation 4.11.

theory	$k$	$\Delta E/c$ ( $\text{MeV}/c/\text{nucleon}$ )	$m_p$
SNFM	0	13	all nucleons
CTM	1	8	interacting nucleons

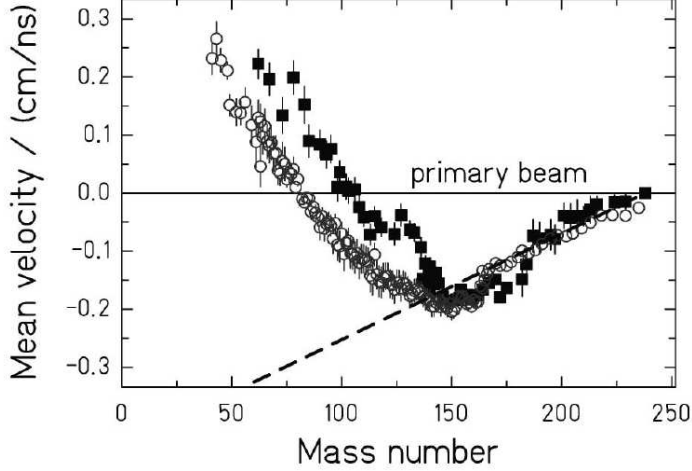


Figure 4.6: The velocity distribution of fragments from the fission-fragmentation reaction of  $^{238}\text{U}$  with Pb (black squares) and  $^{238}\text{U}$  with Ti (unfilled circles) at 1 GeV/nucleon. The figure is from reference [103].

the longitudinal momentum transferred by target fragmentation ( $\langle P_{\parallel}' \rangle$ ) is related to the average velocity of the fragment ( $\langle \beta_{\parallel} \rangle$ ) in the projectile's rest frame can be written as:

$$\langle P_{\parallel}' \rangle = m_{\text{targ}} \langle \beta_{\parallel} \rangle \frac{\beta\gamma}{\gamma+1} \quad (4.12)$$

where  $\beta\gamma/(\gamma+1)$  is a kinematic factor which depends on the incident velocity and the Lorentz factor of the projectile in the lab frame. A literature survey of  $\langle P_{\parallel}' \rangle$  available at the time showed an empirical relationship between the momentum transferred and the mass loss such that

$$\langle P_{\parallel}' \rangle = m\Delta A \quad (4.13)$$

where  $m$  was found to be approximately 8 MeV/c/nucleon, the average binding energy per nucleon for heavy nuclei. This linear trend has been termed the Morrissey systematics. At the time, large scattering in the momentum transfer were evident for large mass losses. Later work at GSI, showed large deviations from the Morrissey systematics for  $\Delta A < A/2$ , see Figure 4.6 [103]. The velocities of the fragments with  $\Delta A < A/2$  showed the opposite trend than the heavier fragments (i.e. fragments were slowing down instead of speeding up). This behavior is thought to be the result

Table 4.6: The slopes of the average parallel momentum transferred for fragment with masses greater than half the projectile's mass.

Target	$^{40}\text{Ar}$ Projectile	$^{48}\text{Ca}$ Projectile
$^9\text{Be}$	5.9(0.4)	-
$^{nat}\text{Ni}$	5.0(0.4)	-
$^{181}\text{Ta}$	6.3(0.5)	4.9(0.4)

of nuclear forces from the participant blast [104]. Friction between the nucleons works to slow the projectile nucleus while the interaction of the participants with the spectator nucleons will accelerate the prefragment. More nucleons can interact at small impact parameters and the transfer of momentum will be larger than the momentum lost through friction, thus the fragments will appear to be reaccelerated. The momentum transferred from the fragmentation of  $^{40}\text{Ar}$  with a)  $^9\text{Be}$ , b)  $^{nat}\text{Ni}$ , and  $^{181}\text{Ta}$  and d)  $^{181}\text{Ca}$  with  $^{181}\text{Ta}$  from the current work are shown in Figure 4.7. The velocities have been corrected for the energy straggling using Equations 4.3 and 4.4 with  $\delta = t/2$ . The linear trend predicted by Morrissey systematics is evident for  $A_P < A_F < A_P/2$ , but slopes smaller than the 8 MeV/c/nucleon (solid lines) were found. The values of the fitted slopes (dotted lines) are summarized in Table 4.6. The small variations between the slopes indicate that there is a small dependence on the target and projectile combination for fragment masses greater than half the projectile mass. Notani et al. found that only the light fragments produced in the reaction of  $^{40}\text{Ar}$  with  $^9\text{Be}$  are reaccelerated in the same manner as the data observed at GSI. They suggested that the rate at which the fragments are reaccelerated varies with the target-projectile due to the different impact parameters [105]. They found that the light fragments created in the reaction of  $^{40}\text{Ar}$  with  $^9\text{Be}$  were reaccelerated at a greater rate than the same fragments produced in the reaction of  $^{40}\text{Ar}$  with  $^{181}\text{Ta}$ . This effect is not clear in the current data due to the large scatter of the data.

The average isobaric velocities have been compared to the predicted velocities at the high and low projectile energies in an attempt to gain a better understanding of

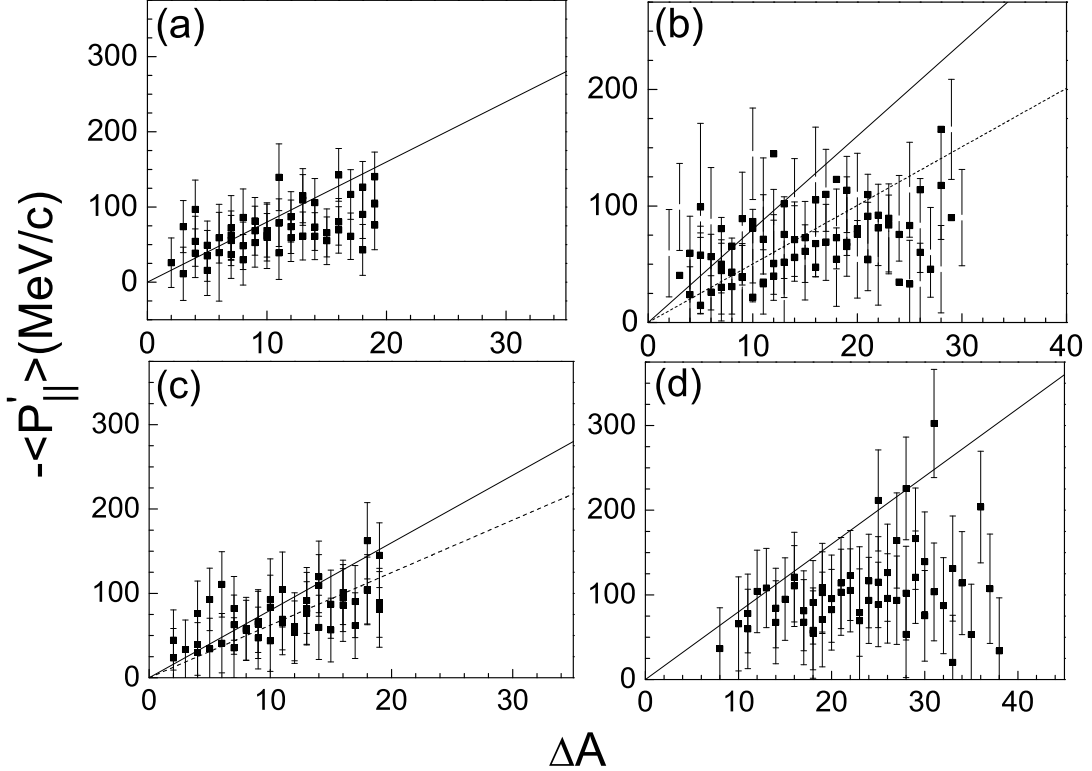


Figure 4.7: The average momentum transfer for  $A_f < A_p/2$  in the projectile frame for the reactions of  ${}^{40}\text{Ar}$  with a)  ${}^9\text{Be}$ , b)  $nat\text{Ni}$ , and c)  ${}^{181}\text{Ta}$  and d)  ${}^{181}\text{Ca}$  with  ${}^{181}\text{Ta}$  is fitted with a liner function (dashed line). A slope of 8 MeV/c/nucleon (solid line) is also shown for reference. The slopes of the lines are summarized in Table 4.6.

the reaction mechanism that creates these fragments. The velocities at the high and low bombarding energy were calculated from the Monte Carlo codes ISABEL [19, 20]+GEMINI [41] (unfilled circles) and deep inelastic transfer (DIT) [23]+GEMINI (unfilled triangles) and compared with the weighted average isobaric velocity in the lab frame from the current experiment (filled squares), see Figure 4.9. The dotted lines represent the primary beam velocities at the center of the target. Thirty thousand primary events (prefragments) were used in the INC calculation with the ISABEL code [19, 20]. The excited prefragments were then de-excited with the GEMINI code. Ten statistical decays were performed for each primary event to determine the final fragment distributions. The velocities of the fragments predicted by the ISABEL+GEMINI calculations were found to decrease linearly as mass was removed

from the projectile. The rate at which the fragment velocities decrease is proportional to the rate predicted by Morrissey systematics using a slope of 8 MeV/c/nucleon (solid line) while the rate at which the fragment velocities decrease due to the nucleon transfer process is small in the low energy limit. The simulations made by the DIT+GEMINI code were calculated using a 140 MeV/nucleon primary beam using 10,000 prefragment events. The velocities were Lorentz boosted into the projectile frame at the center of the target in order to correct for the energy straggling of the primary beams through half of the thicknesses of the targets. For light neutron-rich nuclei at intermediate energies, the corrected DIT+GEMINI velocities are similar to the observed velocities from this work. The overall agreement of the velocities with the DIT+GEMINI may be due to the small range of impact parameters necessary to create the fragments. Thus, a small change in the impact parameter can change the collision from a peripheral one to a central one. The agreement of the velocities with low energy reaction mechanism may indicate that the deep inelastic transfer process persists at an intermediate energy of  $\sim 130$  MeV/nucleon.

The momentum transfers may be sensitive to the target thickness. The energy losses for the thick targets used in the current work tend to be large and the deviation from the Morrissey systematics may be due to corrections for energy straggling. The velocities should be measured for thin targets where the energy losses of the fragments are small to determine whether or not this is the case. The velocities were also compared with work by Notani et al. (open circles) [74] and Mocko et al. (open triangle) [75] to determine if the velocities are sensitive to the energy loss corrections, see Figure 4.8. The trend of the momentum transfers from the current work from the reaction of  $^{40}\text{Ar}$  with  $^{9}\text{Be}$  and  $^{181}\text{Ta}$  agrees with the trend measured by Notani et al. for much thinner targets ( $94.6(0.1)$  mg/cm $^2$   $^{9}\text{Be}$  and  $17.0(0.1)$  mg/cm $^2$   $^{181}\text{Ta}$ ) (panels (a) and (c) in Figure 4.8, respectively). The momentum transfers of fragments produced from the reaction of  $^{48}\text{Ca}$  with  $^{181}\text{Ta}$  are shown in panel (d). A slope of  $5.38(0.07)$  MeV/c/nucleon and intercept of  $26.3(0.06)$  for the momentum transfer of

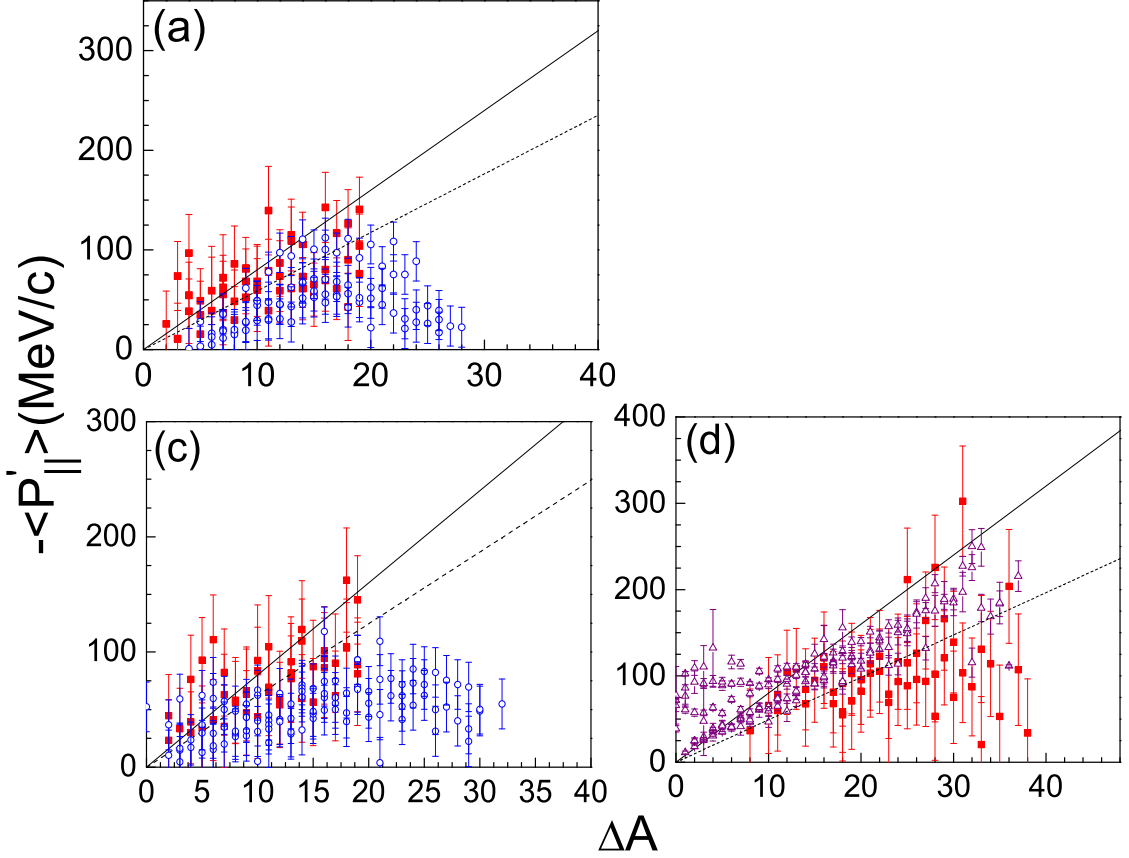


Figure 4.8: The momentum transfers of the fragments from this work are compared to the works by Notani et al. (open circles) [74] and Mocko et al. (open triangle) [75]. The reaction partners in each panel are the same as in Figure 4.7.

fragments with mass between  $A_P/2 \leq A_f \leq A_P$  was found from the data of Mocko et al. using a  $228 \text{ mg/cm}^2$  Ta target. This slope agrees with the value found in the current work (see Table 4.6). In addition to comparing the velocities, one has to compare other observables with predictions from the simulations to determine if the deep inelastic tranfer mechanism is the process that creates these nuclei. The third observable one can measure directly is the reaction cross sections of the fragments.

## 4.4 Cross sections

The cross sections are an important quantity that describes the possibility for a particular reaction to occur. This probability is dependent on the bombarding energy

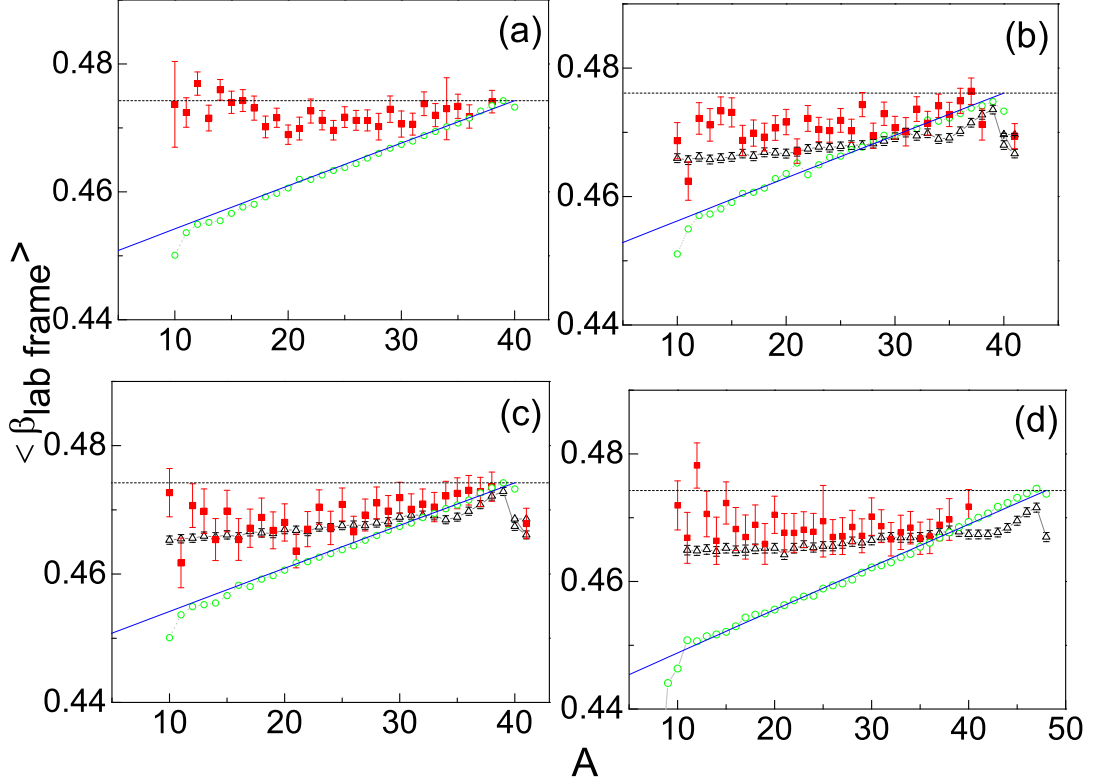


Figure 4.9: The average fragment velocities are plotted as a function of their mass number. Morrissey systematics (solid lines), the projectile bombarding velocities (dashed lines) and the velocities from ISABEL+GEMINI (unfilled circles) and DIT+GEMINI (unfilled triangles) are also shown. The reaction partners in each panel are the same as in Figure 4.7.

and spatial distribution. The reaction cross sections for fragments produced in the four reactions measured in this work were calculated using Equation 1.1 and by the numerical integration of Equation 3.8. The uncertainties in the cross sections were obtained from the propagation of errors and with the use of Leibniz rule in a similar fashion as outlined in reference [106] (see Appendix B for derivation). The cross sections from the reaction of  $^{140}\text{Ar}$  with  $^9\text{Be}$ ,  $^{nat}\text{Ni}$ , and  $^{181}\text{Ta}$  and  $^{48}\text{Ca}$  with  $^{181}\text{Ta}$  are listed in Appendices C and D and are plotted in Figures 4.10, 4.11, 4.12, and 4.13, respectively, using filled squares. Comparisons with data measured by Notanti et al. at RIKEN for the fragmentation of  $^{40}\text{Ar}$  with  $^9\text{Be}$  and  $^{181}\text{Ta}$  at 90-94 MeV/nucleon [74] (filled stars), Mocko et al. at the NSCL using the A1900 at 140 MeV/nucleon [75]

(filled hexagon), EPAX [6, 7] (solid lines) and to simulations from DIT+GEMINI and ISABEL+GEMINI (open triangles and circles, respectively) are also shown. A statistical limit of  $\sim 1/10$  mb were obtained in the simulations for  $10^6$  events. Smaller cross sections may be obtained by increasing the number of prefragments generated, but larger CPU times are required. For example, approximately three months would be required to calculate a cross section of  $10^{-7}$  mb. Thus, only cross sections for the nuclei near stability are shown. The rates of nuclei near the peaks of the cross sections distributions were not measured during this experiment in order to focus on the production of the most neutron-rich elements.

The log of the ratio of the cross sections from simulations and RIKEN with the current work are plotted in Figures 4.14 and 4.15. Smaller values for the fragment cross section from the reaction of  $^{48}\text{Ca}$  with  $^{181}\text{Ta}$  were found in the work Mocko et al. (approximately one and a half times smaller). Small deviations can be contributed to the neglecting of secondary interactions with the target and detector (up to 1%) and the transmission uncertainties (up to 2%) in the analysis of Mocko et al. work. The experimental results from RIKEN and the results from the current work for the fragmentation of  $^{40}\text{Ar}$  with  $^9\text{Be}$  in Figure 4.14 (a) and  $^{181}\text{Ta}$  Figure 4.15 (c) show no dependence of the cross section on the bombarding energies and the two simulations and EPAX are able to predict the correct magnitude for the cross sections for nuclei lighter than the projectile. EPAX under predicts the cross sections for masses heavier than the projectile and ISABEL tends to over predict the cross sections by a factor of three on average for all but one reaction.

The overestimation by ISABEL may be due to the smaller binding energies of these light fragments, see Figure 4.16. Larger excitation energies maybe obtained by lowering the cutoff energies and thus shifting the distributions towards stability. The variation in the binding energy with atomic mass is not taken into account in the current version of ISABEL.

The effect of the target neutron excess on the N/Z of the fragments can be mea-

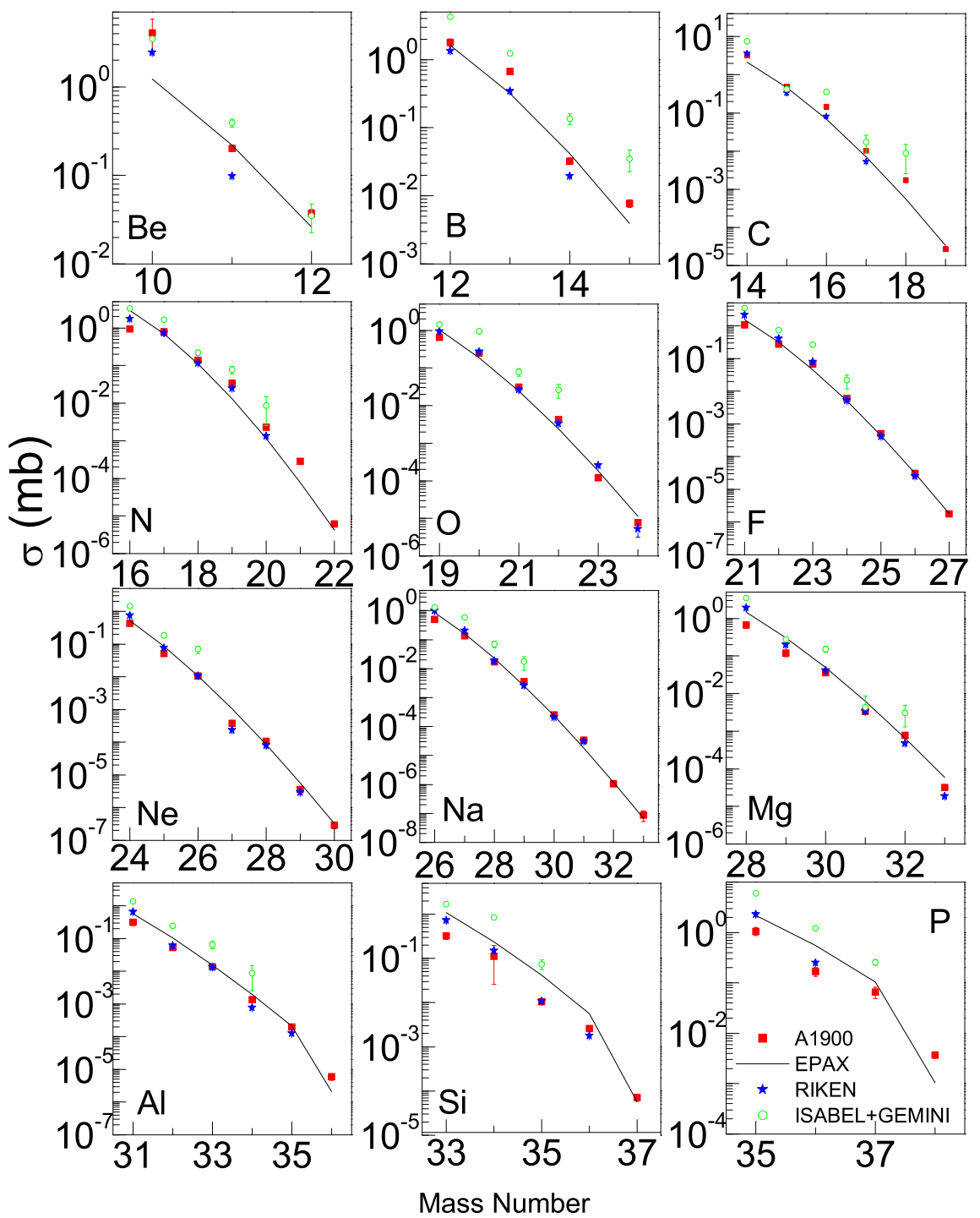


Figure 4.10: Comparison of the cross sections of fragments produced from the reaction of  $^{40}\text{Ar}$  with  $^9\text{Be}$ . The solid lines are the predicted values from EPAX 2.15, and the filled squares and stars are the cross sections measured in this work and from RIKEN, respectively, and the unfilled circles are predictions made by ISABEL+GEMINI.

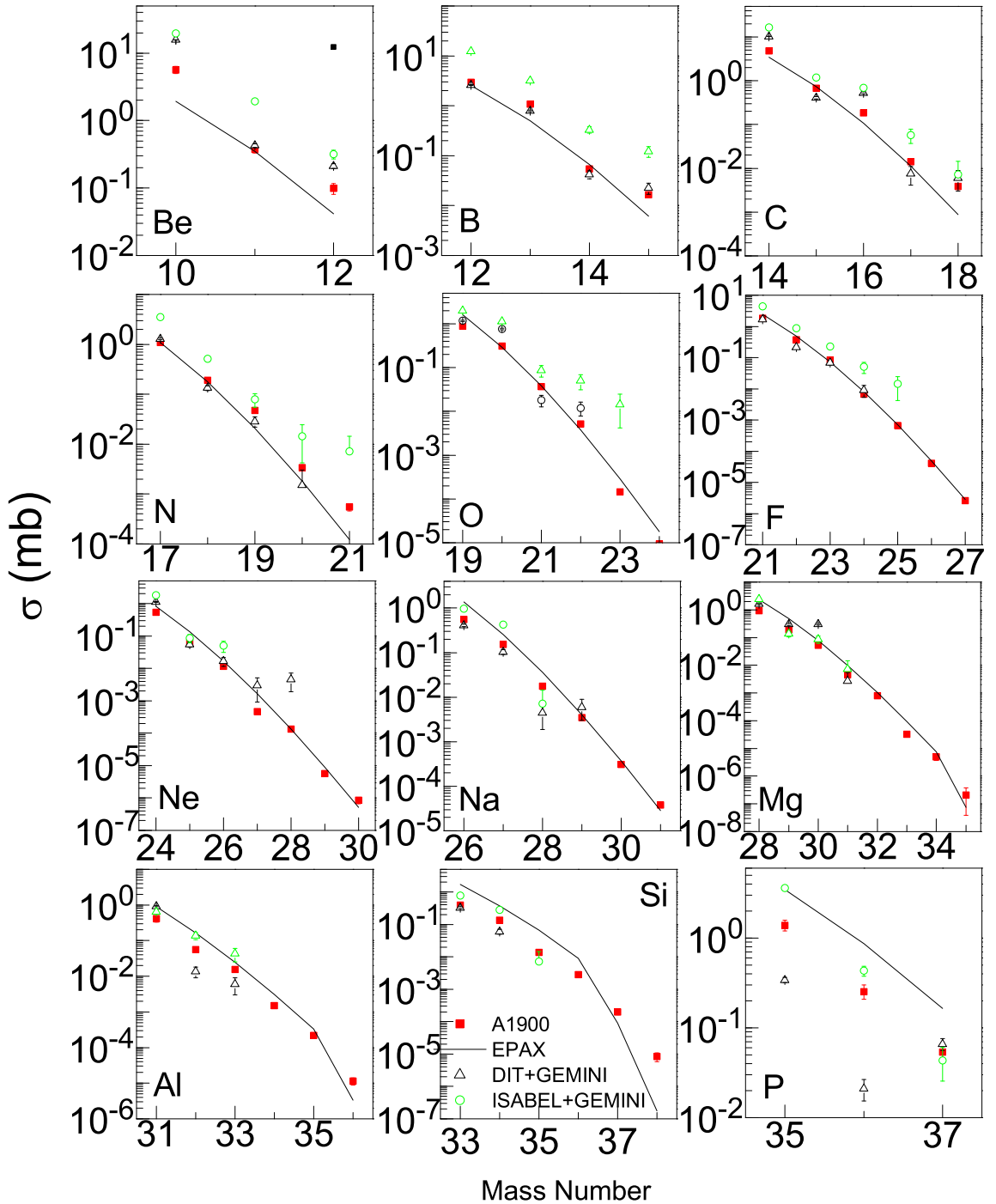


Figure 4.11: The cross sections of fragments produced from the reaction of  $^{40}\text{Ar}$  with  $^{nat}\text{Ni}$ . The unfilled triangles are the simulated cross sections from the DIT+GEMINI codes. The other symbols have the same meaning as in Figure 4.10.

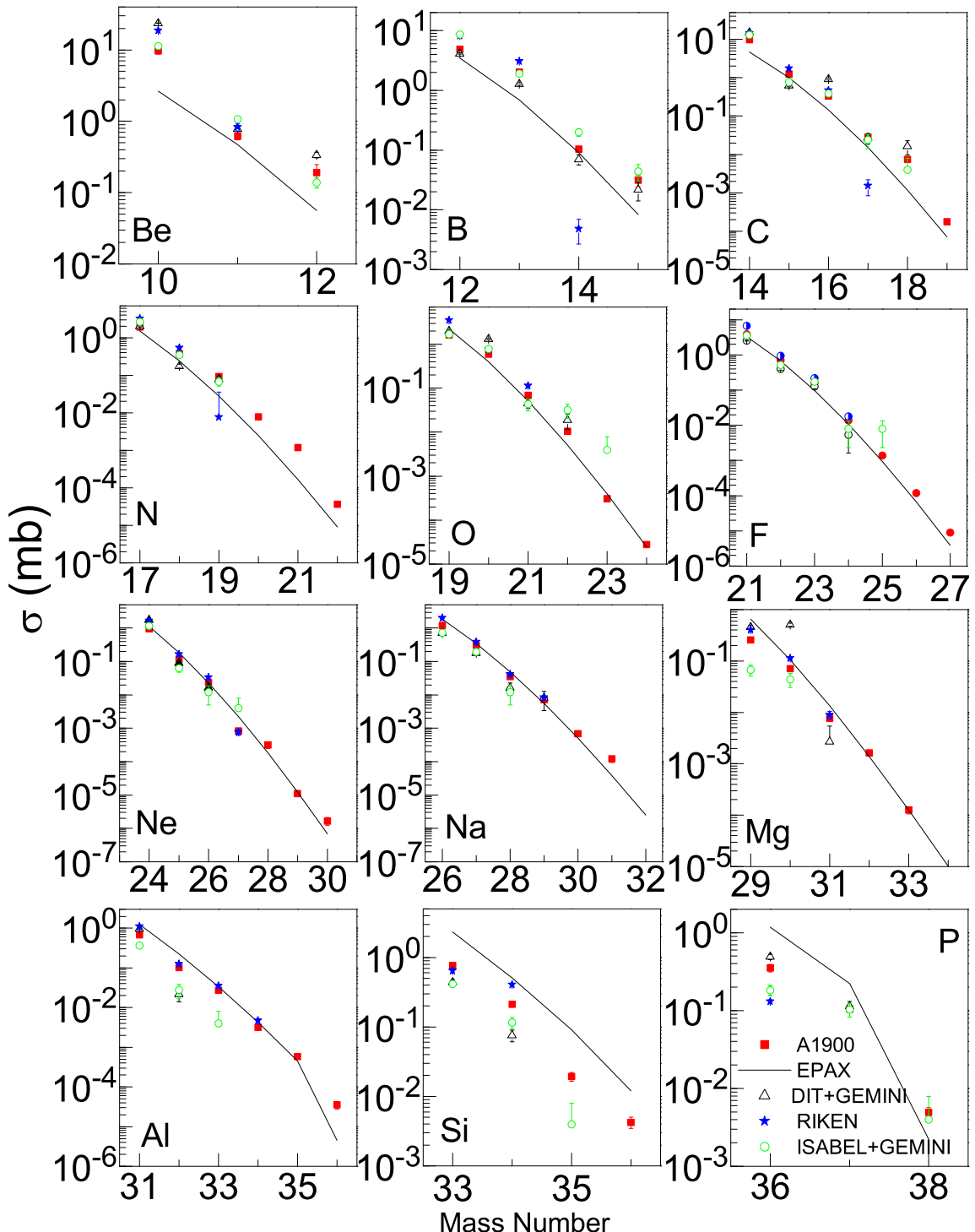


Figure 4.12: The cross sections of fragments produced from the reaction of  $^{40}\text{Ar}$  with  $^{181}\text{Ta}$ . The symbols are the same as in Figures 4.10 and 4.11.

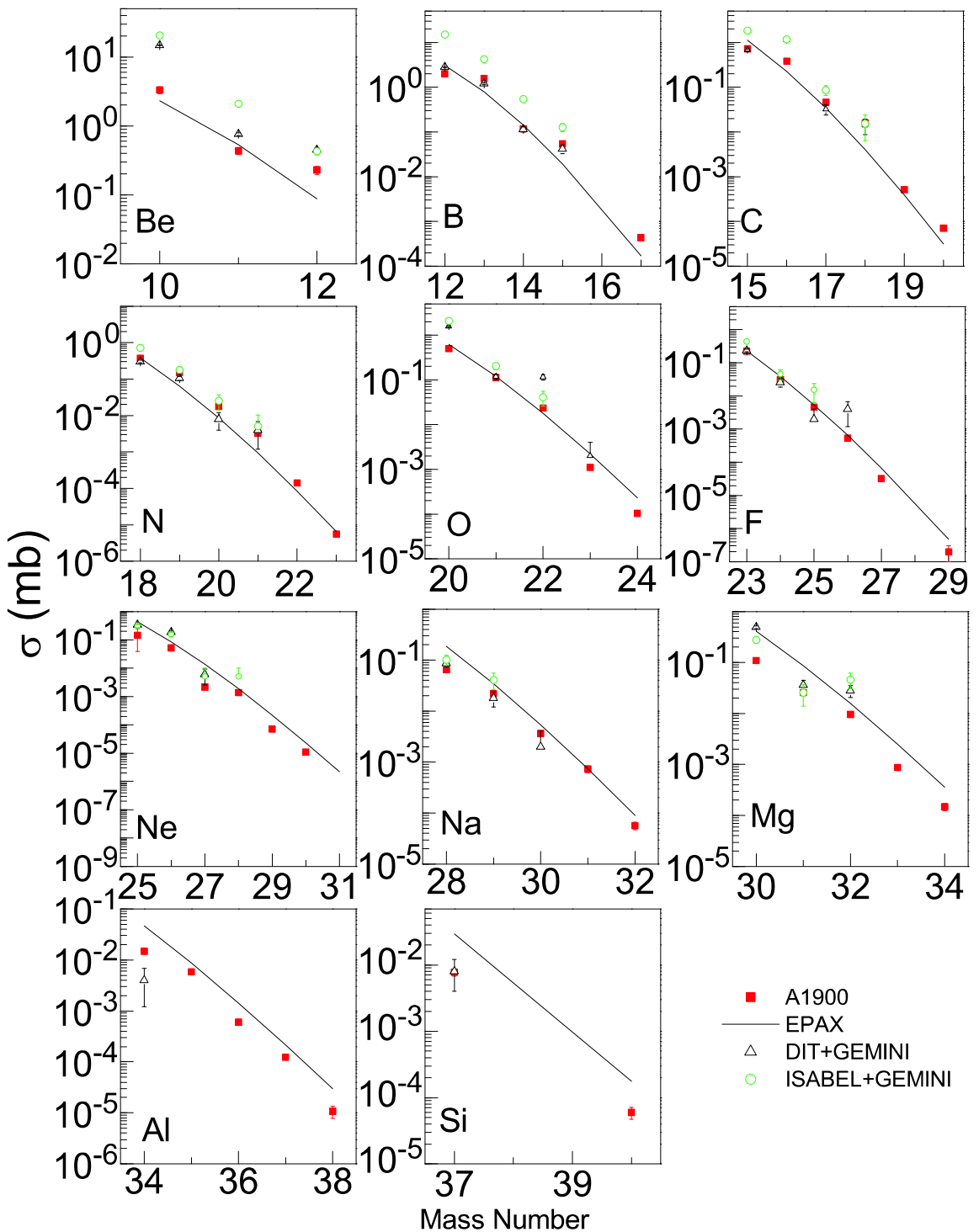


Figure 4.13: The cross sections of fragments produced from the reaction of  $^{48}\text{Ca}$  with  $^{181}\text{Ta}$ . The filled hexagon are cross sections from the work of Mocko et al. [75] and the other symbols are the same as in Figures 4.10 and 4.11.

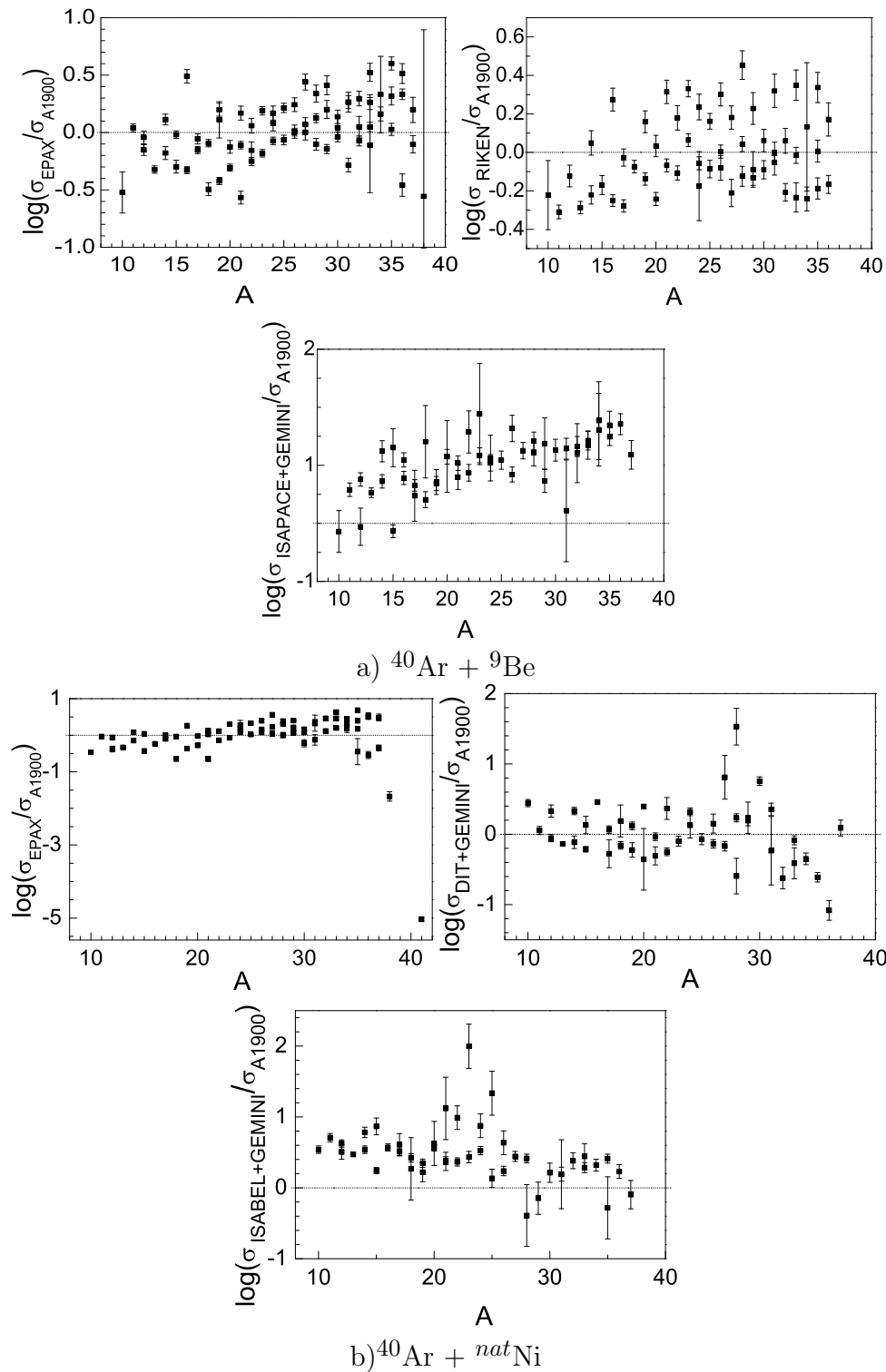


Figure 4.14: The logarithmic ratios of the cross sections of nuclei produced in the reaction of  $^{40}\text{Ar}$  with a)  $^9\text{Be}$  and b)  $^{nat}\text{Ni}$  predicted by EPAX, DIT/GEMINI, and RIKEN relative to data obtained in this work.

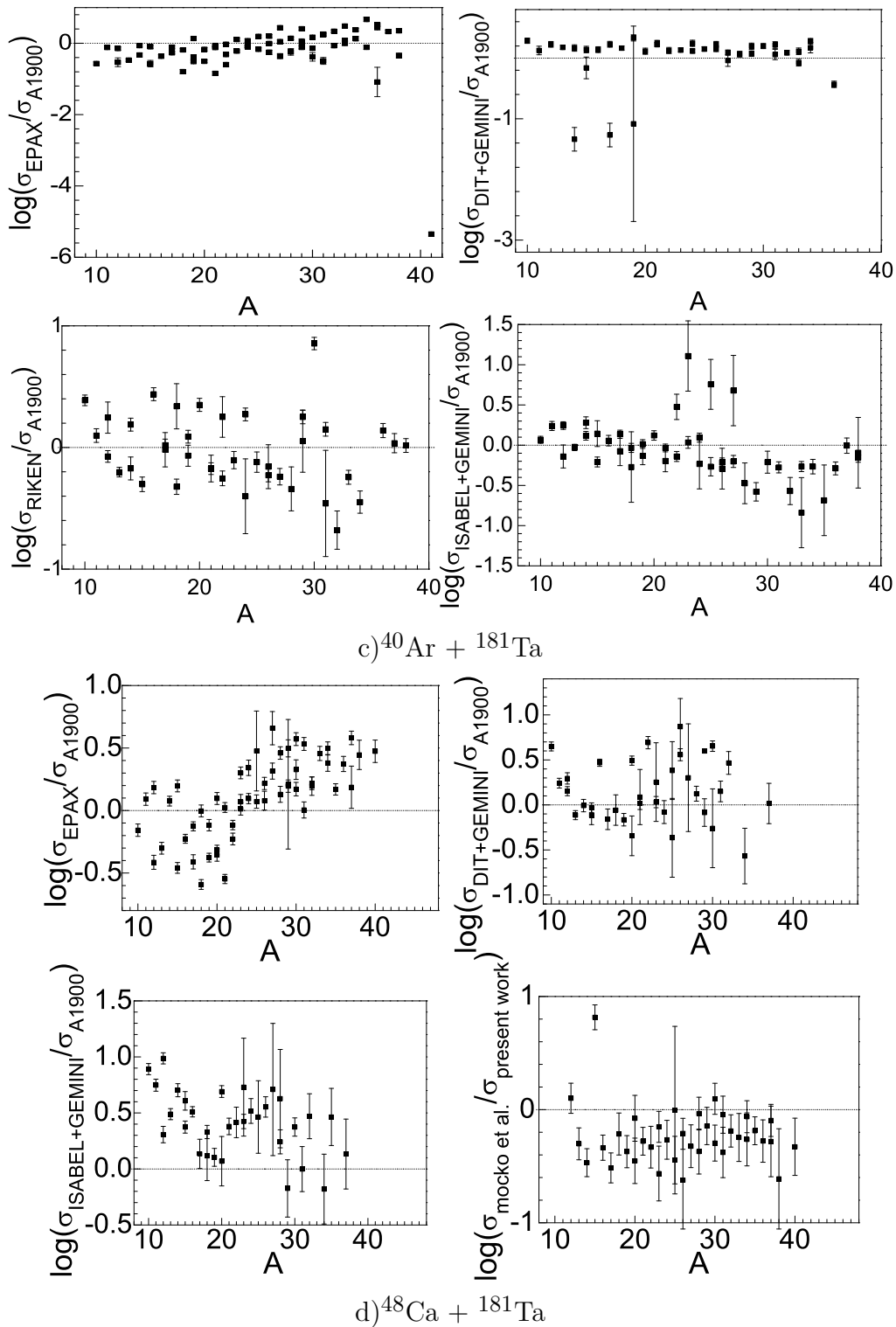


Figure 4.15: The logarithmic ratios of the cross sections of nuclei produced in the reaction of c)  $^{40}\text{Ar}$  and d)  $^{48}\text{Ca}$  with  $^{181}\text{Ta}$  predicted by EPAX, DIT+GEMINI, NSCL and RIKEN relative to data obtained in this work.

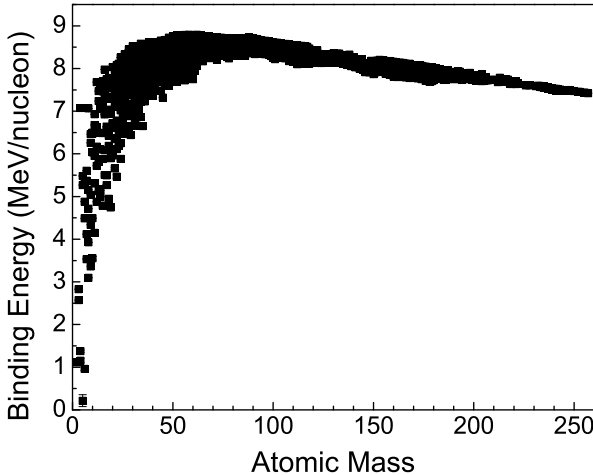


Figure 4.16: The nuclear binding energies per nucleon. The data is from reference [107].

sured by a comparison of the fragment cross sections produced in the different targets. The cross sections of the fragments produced from the reaction of  $^{40}\text{Ar}$  with  $^{nat}\text{Ni}$  and  $^{181}\text{Ta}$  are compared to those produced in  $^9\text{Be}$  Figure 4.17. The ratios of the cross sections have been normalized to the geometric ratios calculated from Equation 4.1 in order to remove the size dependence and are plotted as a function of the fragment's neutron excess relative to  $\beta$ -stability. At intermediate bombarding energies of  $E/A \sim 130$  MeV/nucleon, nuclei near  $\beta$ -stability have no dependence on the target's neutron excess while the yields of most neutron-rich nuclei appear to enhanced. This enhancement suggested that neutron-rich targets are more likely to produce rare isotopes along the neutron-drip-line, thus a  $^{181}\text{Ta}$  target was chosen for the search for the heaviest fluorine isotope in the second measurement.

In the second experiment, an attempt was made to determine the location of the drip-line above oxygen. The nuclei observed along the drip-line are shown in the particle identification plot, Figure 4.18. The heaviest nuclei in the isotopic chain are labeled. Eight  $^{31}\text{F}$  ions were observed from the fragmentation of a  $\sim 8.5$  pnA  $^{48}\text{Ca}$  projectile with a  $^{181}\text{Ta}$  target during two days with the A1900 optimized for  $^{31}\text{F}$  and

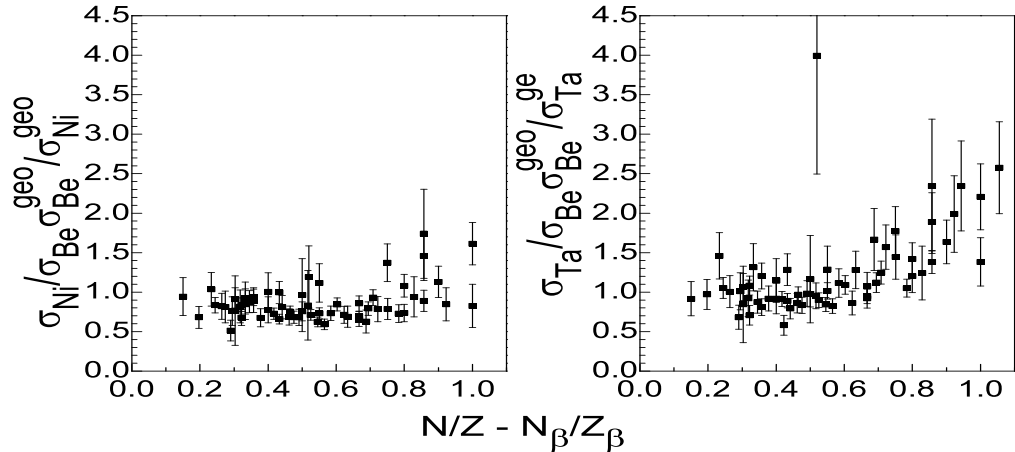


Figure 4.17: The ratios of the cross sections of fragments produced in the fragmentation of  $^{40}\text{Ar}$  with  $^{nat}\text{Ni}$  and  $^{181}\text{Ta}$  are compared with the fragment cross sections from the reaction  $^{40}\text{Ar}$  in  $^9\text{Be}$ .

$^{32}\text{F}$  (five and three particles for the  $^{31}\text{F}$  and  $^{32}\text{F}$  setting, respectively). The presence of the  $N = 2Z$  line and the absence of  $^{13}\text{Be}$ ,  $^{16,18}\text{B}$ ,  $^{21}\text{C}$  and  $^{28,30}\text{F}$  allowed the unambiguous identification of  $^{31}\text{F}$ . No new nuclei were observed. The differential cross sections were fitted with a Gaussian function using the characteristics determined from the fits to the other nuclei. The measured cross sections from GANIL [11] (open triangle), RIKEN [10, 105] (open circles) and the NSCL (present work given by the filled square) are plotted in Figure 4.19(b).

The cross section of  $^{31}\text{F}$  produced in the reaction of  $^{40}\text{Ar}$  with  $^{181}\text{Ta}$  (Figure 4.18(a)) and the predicted cross sections made by EPAX (dashed lines) for the fragmentation of  $^{40}\text{Ar}$  and  $^{48}\text{Ca}$  with  $^{181}\text{Ta}$  (dashed lines) are also shown for reference. No uncertainties were reported in reference [11], statistical errors were assumed for the cross section. The current experiment and the values obtained from RIKEN and GANIL indicate that  $^{31}\text{F}$  has a cross section of about 1 pb independent of the projectile energy. This small cross section demonstrates the difficulty of producing and observing very neutron-rich nuclei even for light elements and this is why the drip-line is only known for the lightest elements.

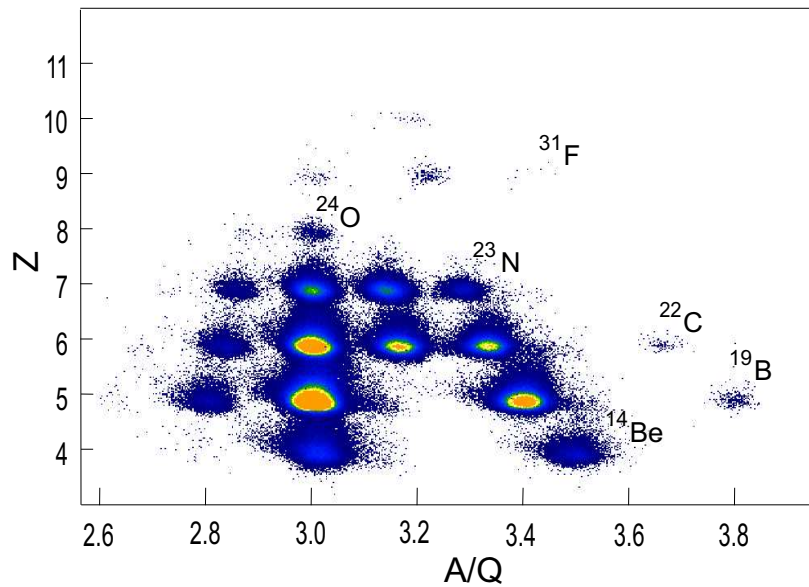


Figure 4.18: Eight  $^{31}\text{F}$  ions were observed at two A1900  $B\rho$  settings optimized for the transmission of  $^{31}\text{F}$  and  $^{32}\text{F}$ . The heaviest isotopes observed in the chart of the nuclides are labeled up to fluorine. Twenty-six isotopes were observed in these runs.

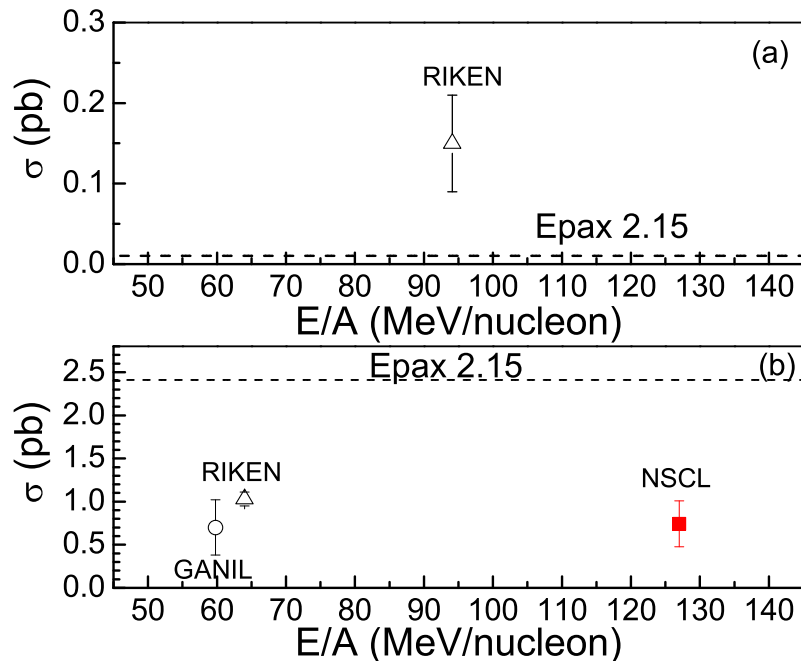


Figure 4.19: The cross sections of  $^{31}\text{F}$  produced in the reactions of (a) $^{40}\text{Ar}$  with  $^{181}\text{Ta}$  and (b) $^{48}\text{Ca}$  with  $^{181}\text{Ta}$  measured at GANIL (open circle), RIKEN (open triangles), and the NSCL (the present work, filled square). The dashed lines are the predicted cross sections made by EPAX 2.15.

# Chapter 5

## Summary

Two experiments were performed at the NSCL using the A1900 fragment separator to produce fragments near the neutron drip-line. The establishment of the limits of stability is important in the understanding of isospin asymmetries and how the shell structure changes as one moves away from  $\beta$  stability. The yields of nuclei produced in the fragmentation of  $^{40}\text{Ar}$  with  $^9\text{Be}$ ,  $^{nat}\text{Ni}$ , and  $^{181}\text{Ta}$  and  $^{48}\text{Ca}$  with  $^{181}\text{Ta}$  were measured using the A1900 fragment separator. An asymmetric Gaussian (Gaussian + asymmetric tail on the low momentum side) was found to describe the momentum distributions of fragments and the asymmetric factor was found to be independent of the fragment mass, see Appendices C and D. The parallel momentum widths, parallel momentum transfers, and fragmentation cross sections were extracted from the parameters of the asymmetric Gaussian and the observables from the current work were compared with an intranuclear cascade code ISABEL and a deep inelastic transfer code (DIT) both coupled to a deexcitation code GEMINI in an attempt to understand the reaction mechanism.

The cross sections for 255 isotopes (201 from the fragmentation of  $^{40}\text{Ar}$  and 54 from the fragmentation of  $^{48}\text{Ca}$ ) were measured in the current work. The parallel momentum widths of light neutron-rich nuclei produced from projectile fragmentation at intermediate energies are consistent with the predicted momentum widths from the si-

multaneous emission of nucleons and the momentum widths from ISABEL+GEMINI. The reduced widths from the present work were found to be  $\sim 85$  MeV/c (Fermi momentum  $\sim 190$  MeV/c) independent of the target and projectile combination. This value agrees with literature values for higher bombarding energies. The momentum transfer due to the breaking of the nuclear bonds during the emission of the cluster has been observed to follow the linear trend predicted by Morrissey systematics for fragments with  $\Delta A < A_p/2$ , but with smaller slopes. This behavior was also observed in the dissertation work of Notani et al. for the fragmentation of  $^{40}\text{Ar}$  with much thinner  $^9\text{Be}$  and  $^{181}\text{Ta}$  targets. No conclusions about the reacceleration phenomena of light fragments ( $A_F < A_P/2$ ) observed at GSI could be made due to the large scatter of the data. The average fragment velocities were also compared with simulations valid at the high and low energy regimes, ISABEL+GEMINI and DIT+GEMINI, respectively. The predicted velocities of fragments from ISABEL+GEMINI were found to have velocities similar to the velocities predicted by Morrissey systematics, but disagreed with the average velocities of the light fragments measured in the current work. The velocities were found to be similar to the velocities predicted by a deep inelastic transfer code (DIT) code. The velocities were also compared with fragments produced from the fragmentation of  $^{40}\text{Ar}$  and  $^{48}\text{Ca}$  with thin targets to determine if the thick targets used in the present work distorted the transfer mechanism. Similar trends from data taken at RIKEN and the NSCL indicated that the momentum transfer of fragments produced in the current work may be different than the trend seen for heavier projectiles (i.e. the Morrissey systematics). This effect may be due to the small impact parameters required to create these fragments.

The high predictive power of the two Monte Carlo codes DIT+GEMINI and ISABEL+GEMINI for the cross sections of the neutron deficient nuclei in the present experiment has been demonstrated (i.e. the simulations are able to predict the cross sections to within a factor of ten). The excitation energies of the prefragments from ISABEL were found to depend on the target and the number of nucleons abraded

from the projectile and become significantly larger than the 8 MeV/nucleon excitation energy used in LISE. The different excitation energies and distributions of the pre-fragment predicted ISABEL and LISE were found to lead to very similar predictions of the cross sections. This indicates that the cross sections of the final fragments are largely dependent on the excitation energy, prefragment distribution, and the decay widths of the products. The similar cross sections and fragment velocities from the DIT+GEMINI codes with the present work indicates that the low energy mechanism is most likely the dominant factor in creating light neutron-rich nuclei near the drip-line.

The existence of  $^{31}\text{F}$  was reconfirmed and no new nuclei along the neutron drip-line were observed. A cross section of  $\sim 1$  pb from the fragmentation of  $^{48}\text{Ca}$  with  $^{181}\text{Ta}$  for  $^{31}\text{F}$  has been measured at RIKEN, GANIL, and the NSCL independent of projectile energy. No conclusions about the existence of  $^{32,33}\text{F}$  could be drawn under the running conditions of the current work. The current work extends the measured cross sections to the most neutron rich nuclei along the drip-line and can be used to improve on the extrapolation for the cross sections heavier neutron-rich nuclei. The cross sections of nuclei produced from the reaction of  $^{40}\text{Ar}$  with  $^9\text{Be}$  and  $^{181}\text{Ta}$  were observed to be independent of the bombarding energy in the energy range of 60 - 130 MeV/nucleon. This suggests that the “limiting fragmentation” energy regime has been reached and that the EPAX formulation should be valid. The empirical formula in EPAX has been shown to be able to predict the cross sections of all nuclei produced by fragmentation (i.e.  $A_f \leq A_P$ ) including the most neutron-rich nuclei in this work to within a factor of ten. It has been found that EPAX overpredicts the yields of nuclei near the drip-line by a factor of two in the case of  $^{31}\text{F}$ .

The cross sections of nuclei produced from the fragmentation of  $^{40}\text{Ar}$  were compared with each other to determine the effect of the N/Z ratio of the target on the fragmentation yields. There was a strong indication that the target’s neutron-excess does enhance the yields of the most neutron-rich nuclei and that the target with larger

neutron-excess has a larger effect. This effect becomes important when searching for new nuclei where time constraints are an issue. More work in this region is necessary to determine the exact locations of the drip-line. The cross sections in this work may be incorporated into EPAX to improve on the reliability of the predictions near the neutron-drip line. A recent upgrade in the  $^{48}\text{Ca}$  beam intensity ( $\sim 15$  times the intensities used in the present work) would allow the search for new particle bound nuclei in this region. With higher beam intensities, new challenges arise, such as managing the heat load on the production target. One must be able to circumvent these challenges in order to extend the known limits of existence.

## **Appendix A**

### **Input Parameters for ISABEL and GEMINI**

The following tables are sample input files used in ISABEL (Table A.1) and GEMINI (Table A.2) codes for the reaction of  $^{48}\text{Ca} + ^{181}\text{Ta}$  at  $\sim 127$  MeV/nucleon. Similar input files were used for the other three reactions with the  $^{40}\text{Ar}$  projectile.

Table A.1: Input parameters used in ISABEL.

0	projectile type
1059.3	incident energy (MeV/n) + 931.5
181.0	A target
73.0	Z target
8.02	binding energy per nucleon in target
10000	number of cascades
8.666	binding energy per nucleon in projectile
0	cutoffa(1)
0	cutoffa(2)
0	cutoffa(3)
0	cutoffa(4)
0	cutoffa(10)
0	cutoffa(11)
73	model used
0	vpion
0	isonsw
0	mprint (print option)
20.	timef
3	ntdel
3.0	rcas
48.0	A projectile
20.0	Z projectile
-99	yp (impact parameter)
3	jkey (option for evaporation file)
1	option for Pauli principle IPAULI
1	option to restrict distance NP
2	type of restriction of distance
1.1	gapl
-2.5 1.0 0.6 0.6 0.6 0.6 0.6 1.0	dx(1-8)
-2.5 1.0 0.9 0.6 0.3 0.2 0.2 0.2 0.3 0.3 0.4 0.4 0.4 0.4 0.4 0.4 0.4 dxp(1-16)	
7	iden (option radial density)
0.	vap (amplitude of potential anti-pr)
0	nopot
0	kaskew
0.	gamiso
6000000	nzman (variable to stop program, in 1/100 s)
5564350	irand

Table A.2: Input parameters used in GEMINI.

```
***** output choices *****
.false.      ,diagnostics, true=events typed out
.false.      ,time_flag=.true. emission times written out on event file
.false.      ,J_flag
.FALSE.     ,ex_flag
.true.       ,I_angle=switch to calculate angles,
.false.      ,true=quantum treatment of angles, false=semi-classical
***** fission and IMF parameters *****
2           ,imf_option,1=symmetric fission,2=all asymmetries,0=no imf
0.          ,t_delay=fission delay time in 10E-21 seconds
0.          ,sig_delay = first moment of delay as function of eta
.TRUE.      ,sharp_delay, gamma(t) = 0 (T) or gamma_0*t/t_delay(F)
5           ,Z_imf_min, minimum imf charge considered,
0.0         ,Kramers factor (only for IMF_option=1)
.FALSE.     ,LESTONE
1.          ,b_scale
***** evaporation + gamma emission*****
.true.      ,tl_iwbc, true=tl's from IWBC model, False=sharp cut-off
.FALSE.     ,k_sum,
.false.      ,polarization
2           ,exotic_index
-1.0        ,ratio
2           ,mass_option,0=liquid drop,1=experimental,2=shell fadeout
50.0        ,E2 strength in Weiskopf units (default=50)
0.1         ,E1_strength
1e-5        ,threshold
***** level density *****
0           ,aden_type
8.5         ,aden_0=level density constant (k=A/a)
1.00        ,a_scale
```

# Appendix B

## Derivations

### B.1 Calculating uncertainties in the cross-sections

Numerical integration of the asymmetric Gaussian

$$y = y_0 \text{Exp}\left[-\frac{(x - x_0)^2}{a^2(1 + (x_0 - x)\delta/a)}\right] \quad (\text{B.1})$$

where

$$\delta = \begin{cases} 0 & x \geq x_0 \\ 1 & x < x_0 \end{cases} \quad (\text{B.2})$$

has been used to determine the cross-sections listed in Appendices C and D. The errors associated with function B.1 were determined using Leibnitz Theorem in a similar manner as outlined in reference [106]. Leibnitz Theorem states that the derivative of an integral can be written as

$$\frac{d}{dx} \int_m^n f(x, y) dy = f(x, n) \frac{dn}{dx} - f(x, m) \frac{dm}{dx} + \int_n^m \frac{\delta f(x, y)}{\delta x} dy \quad (\text{B.3})$$

where  $f(x,y)$  is an function of  $x$  and  $y$ . Thus, it can be shown that the uncertainty in equation B.1 may be calculated by the following function

$$\begin{aligned}\delta y^2 = & \int \left( \frac{\delta y}{\delta y_o} \sigma^2(y_o) \right)^2 + \left( \frac{\delta y}{\delta x_o} \sigma^2(x_o) \right)^2 + \left( \frac{\delta y}{\delta a} \sigma^2(a) \right)^2 + \left( \frac{\delta y}{\delta b} \sigma^2(b) \right)^2 \\ & + 2 \frac{\delta y}{\delta y_o} \sigma(y_o) \left( \frac{\delta y}{\delta x_o} \sigma(x_o) + \frac{\delta y}{\delta a} \sigma(a) + \frac{\delta y}{\delta b} \sigma(b) \right) \\ & + 2 \frac{\delta y}{\delta x_o} \sigma(x_o) \left( \frac{\delta y}{\delta a} \sigma(a) + \frac{\delta y}{\delta b} \sigma(b) \right) + 2 \frac{\delta y}{\delta a} \frac{\delta y}{\delta b} \sigma(a) \sigma(b)\end{aligned}\quad (\text{B.4})$$

The partial derivatives of the asymmetric Gaussian are given by:

$$\frac{\delta y}{\delta y_o} = \text{Exp} \left[ -\frac{(x - x_o)^2}{a^2 \left( 1 + \frac{b(-x+x_o)}{a} \right)} \right] \quad (\text{B.5})$$

$$\frac{\delta y}{\delta x_o} = \frac{A \left( \frac{b(x-x_o)^2}{a^3 \left( 1 + \frac{b(-x+x_o)}{a} \right)^2} + \frac{2(x-x_o)}{a^2 \left( 1 + \frac{b(-x+x_o)}{a} \right)} \right)}{\text{Exp} \left[ \frac{(x-x_o)^2}{a^2 \left( 1 + \frac{b(-x+x_o)}{a} \right)} \right]} \quad (\text{B.6})$$

$$\frac{\delta y}{\delta a} = \frac{A \left( -\frac{b(x-x_o)^2(-x+x_o)}{a^4 \left( 1 + \frac{b(-x+x_o)}{a} \right)^2} + \frac{2(x-x_o)^2}{a^3 \left( 1 + \frac{b(-x+x_o)}{a} \right)} \right)}{\text{Exp} \left[ \frac{(x-x_o)^2}{a^2 \left( 1 + \frac{b(-x+x_o)}{a} \right)} \right]} \quad (\text{B.7})$$

$$\frac{\delta y}{\delta b} = \frac{A (x - x_o)^2 (-x + x_o)}{\text{Exp} \left[ \frac{(x-x_o)^2}{a^2 \left( 1 + \frac{b(-x+x_o)}{a} \right)} \right] a^3 \left( 1 + \frac{b(-x+x_o)}{a} \right)^2} \quad (\text{B.8})$$

# Appendix C

## Data from the Fragmenation of $^{40}\text{Ar}$

The following tables list the isotropic cross sections in mb for the reaction of a~128 MeV/nucleon  $^{40}\text{Ar}$  projectile with  $^9\text{Be}$  (Table C.1),  $^{nat}\text{Ni}$  (Table C.5), and  $^{181}\text{Ta}$  (Table C.9). Only momentum distributions that could be fitted are listed below. The uncertainties quoted for the two simulations are statistical.

### C.1 Fragments produced from the fragmentation of $^{40}\text{Ar} + ^9\text{Be}$

#### C.1.1 Cross Section

Table C.1: Reaction Cross Sections of  $^{40}\text{Ar} + ^9\text{Be}$ .

Z	A	$\sigma$	EPAX	ISABEL+GEMINI
4	10	4.09(1.69)E+0	1.23E+00	3.48(0.12)E+0
4	11	2.01(1.62)E-1	2.20E-01	3.92(0.41)E-1
4	12	3.72(3.99)E-2	2.62E-02	3.48(1.23)E-2
5	12	1.79(2.31)E+0	1.62E+00	4.28(0.14)E+0
5	13	6.70(4.93)E-1	3.19E-01	1.23(0.07)E+0
5	14	3.23(3.48)E-2	4.19E-02	1.35(0.24)E-1
5	15	7.76(9.98)E-3	3.91E-03	3.48(1.23)E-2

Table C.1 – continued from previous page

Z	A	$\sigma$	EPAX	ISABEL+GEMINI
6	14	3.26(4.25)E+0	2.16E+00	7.49(0.18)E+0
6	15	4.88(3.66)E-1	4.68E-01	4.18(0.43)E-1
6	16	1.45(1.00)E-1	6.81E-02	3.57(0.39)E-1
6	17	1.01(7.23)E-2	7.09E-03	1.74(0.87)E-2
6	18	1.72(2.22)E-3	5.53E-04	8.70(6.15)E-3
6	19	2.59(0.41)E-5	3.34E-05	-(-)
7	16	9.36(1.28)E-1	2.89E+00	3.29(0.12)E+0
7	17	7.87(8.06)E-1	6.93E-01	1.67(0.09)E+0
7	18	1.39(1.03)E-1	1.12E-01	2.22(0.31)E-1
7	19	3.45(2.51)E-2	1.30E-02	7.83(1.85)E-2
7	20	2.31(1.65)E-3	1.14E-03	8.70(6.15)E-3
7	21	2.87(3.68)E-4	7.78E-05	-(-)
7	22	6.09(1.04)E-6	4.25E-06	-(-)
8	19	6.54(8.55)E-1	1.03E+00	1.44(0.08)E+0
8	20	2.48(3.17)E-1	1.86E-01	9.31(0.64)E-1
8	21	3.12(2.38)E-2	2.42E-02	7.83(1.85)E-2
8	22	4.26(3.55)E-3	2.38E-03	2.61(1.07)E-2
8	23	1.19(1.02)E-4	1.84E-04	1.04(1.04)E-3
8	24	7.72(1.09)E-6	1.14E-05	-(-)
9	21	1.05(1.47)E+0	1.54E+00	3.46(0.12)E+0
9	22	2.71(3.96)E-1	3.11E-01	7.40(0.57)E-1
9	23	6.88(5.16)E-2	4.54E-02	2.65(0.34)E-1
9	24	5.96(4.54)E-3	5.03E-03	2.18(0.97)E-2
9	25	5.10(4.96)E-4	4.39E-04	-(-)
9	26	3.05(4.01)E-5	3.10E-05	-(-)
9	27	1.80(2.80)E-6	1.81E-06	-(-)
10	24	4.32(6.64)E-1	5.21E-01	1.44(0.08)E+0
10	25	5.22(4.85)E-2	8.55E-02	1.83(0.28)E-1
10	26	1.06(8.24)E-2	1.07E-02	6.96(1.74)E-2
10	27	3.85(6.15)E-4	1.06E-03	-(-)
10	28	1.07(1.28)E-4	8.49E-05	-(-)
10	29	3.58(6.46)E-6	5.69E-06	-(-)
10	30	2.93(0.64)E-7	3.24E-07	-(-)
11	26	5.00(6.85)E-1	8.73E-01	1.32(0.08)E+0
11	27	1.38(1.91)E-1	1.61E-01	5.83(0.50)E-1
11	28	1.71(1.52)E-2	2.28E-02	6.96(1.74)E-2
11	29	3.57(3.26)E-3	2.56E-03	1.74(0.87)E-2
11	30	2.56(2.57)E-4	2.35E-04	-(-)
11	31	3.46(4.77)E-5	1.80E-05	-(-)
11	32	1.05(2.19)E-6	1.18E-06	-(-)
11	33	8.86(3.67)E-8	6.88E-08	-(-)
12	28	6.69(1.14)E-1	1.46E+00	3.43(0.12)E+0
12	29	1.18(2.24)E-1	3.05E-01	2.74(0.35)E-1
12	30	3.57(4.78)E-2	4.89E-02	1.52(0.26)E-1

**Table C.1 – continued from previous page**

Z	A	$\sigma$	EPAX	ISABEL+GEMINI
12	31	3.39(4.44)E-3	6.24E-03	4.35(4.35)E-3
12	32	7.73(7.84)E-4	6.53E-04	3.11(1.79)E-3
12	33	3.19(4.72)E-5	5.86E-05	-(-)
13	31	3.12(6.20)E-1	5.73E-01	1.37(0.08)E+0
13	32	5.31(7.85)E-2	1.05E-01	2.44(0.33)E-1
13	33	1.39(1.33)E-2	1.55E-02	6.53(1.69)E-2
13	34	1.36(1.90)E-3	1.97E-03	8.70(6.15)E-3
13	35	1.97(2.39)E-4	2.10E-04	-(-)
13	36	6.03(1.35)E-6	2.10E-06	-(-)
14	33	3.25(5.89)E-1	1.09E+00	1.68(0.09)E+0
14	34	1.11(8.49)E-1	2.37E-01	8.49(0.61)E-1
14	35	1.05(1.38)E-2	4.21E-02	7.40(1.79)E-2
14	36	2.61(2.78)E-3	5.62E-03	-(-)
14	37	7.12(1.24)E-5	5.62E-05	-(-)
15	35	1.06(1.91)E+0	2.20E+00	5.95(0.16)E+0
15	36	1.69(3.35)E-1	5.50E-01	1.21(0.07)E+0
15	37	6.60(1.67)E-2	1.04E-01	2.57(0.33)E-1
15	38	3.74(5.44)E-3	1.04E-03	-(-)

### C.1.2 Parallel Momentum Widths

Table C.2: Parallel momentum widths from the reaction of  $^{40}\text{Ar} + ^9\text{Be}$ .

Z	A	Lab Frame				Projectile Frame
		$\sigma(P)$ (MeV/c)	$\sigma(E)$ (MeV)	$\sigma_{dE}$ MeV	${}^1\sigma_N(E)$ MeV	${}^1\sigma_N(P)$ (MeV/c)
4	10	306(43)	144(16)	80.9(0.4)	119(20)	253(112)
4	11	292(6)	137(10)	91.0(0.4)	102(13)	218(18)
4	12	322(16)	146(10)	101.1(0.5)	106(14)	233(24)
5	12	311(4)	147(9)	89.9(0.4)	116(12)	246(12)
5	13	355(7)	166(10)	99.9(0.5)	132(12)	283(17)
5	14	382(18)	177(10)	110.0(0.5)	139(13)	300(23)
5	15	431(11)	197(10)	120.1(0.6)	156(12)	342(10)
6	14	316(3)	148(8)	96.3(0.4)	113(11)	241(10)
6	15	342(4)	160(8)	106.4(0.5)	119(11)	255(13)
6	16	400(7)	185(9)	116.5(0.5)	144(11)	311(13)
6	17	416(7)	192(9)	126.6(0.6)	144(12)	313(13)
						277(17)

Table C.2 – continued from previous page

Z	A	$\sigma(P)$ (MeV/c)	$\sigma(E)$ (MeV)	$\sigma_{dE}$ MeV	${}^1\sigma_N(E)$ MeV	${}^1\sigma_N(P)$ (MeV/c)	$\sigma_N(P)$ (MeV/c)
6	18	478(10)	220(9)	136.7(0.6)	172(12)	375(8)	333(11)
6	19	389(30)	179(8)	146.7(0.7)	102(13)	222(19)	197(23)
7	16	345(7)	161(8)	100.3(0.5)	126(10)	270(15)	238(17)
7	17	362(7)	169(8)	110.4(0.5)	127(11)	274(19)	243(22)
7	18	394(7)	182(8)	120.5(0.6)	137(10)	296(13)	262(16)
7	19	395(4)	183(7)	130.6(0.6)	129(10)	277(10)	245(12)
7	20	450(7)	207(8)	140.6(0.6)	152(11)	330(12)	293(15)
7	21	515(11)	236(8)	150.7(0.7)	181(11)	396(9)	352(11)
7	22	437(38)	201(7)	160.8(0.7)	120(12)	261(17)	232(20)
8	19	366(3)	169(7)	111.9(0.5)	127(9)	275(8)	244(10)
8	20	398(3)	183(7)	122.0(0.6)	136(9)	297(8)	264(10)
8	21	430(8)	197(7)	132.0(0.6)	147(10)	320(13)	284(15)
8	22	428(9)	197(7)	142.1(0.7)	137(10)	297(13)	264(15)
8	23	521(23)	239(8)	152.2(0.7)	184(11)	401(16)	357(19)
8	24	497(33)	227(8)	162.3(0.7)	159(11)	348(22)	310(26)
9	21	451(26)	207(8)	110.9(0.5)	175(9)	381(16)	338(19)
9	22	367(7)	170(6)	121.0(0.6)	119(9)	258(19)	228(22)
9	23	386(4)	178(6)	131.1(0.6)	121(9)	261(9)	232(11)
9	24	400(5)	184(6)	141.1(0.6)	119(9)	257(9)	228(11)
9	25	419(10)	193(6)	151.2(0.7)	121(10)	261(13)	232(15)
9	26	480(11)	220(7)	161.3(0.7)	150(10)	326(13)	290(16)
9	27	499(26)	228(7)	171.4(0.8)	151(11)	330(25)	293(29)
10	24	421(14)	193(6)	117.5(0.5)	153(8)	334(8)	297(10)
10	25	377(6)	174(6)	127.6(0.6)	118(8)	255(12)	227(14)
10	26	397(5)	183(5)	137.6(0.6)	120(8)	261(8)	232(11)
10	27	457(13)	209(6)	147.7(0.7)	147(9)	323(18)	287(22)
10	28	468(20)	215(6)	157.8(0.7)	146(9)	317(18)	282(21)
10	29	545(44)	248(8)	167.9(0.8)	182(11)	400(42)	357(48)
10	30	455(40)	210(7)	178.0(0.8)	112(13)	242(40)	215(46)
11	26	368(5)	168(5)	111.5(0.5)	126(7)	276(7)	245(8)
11	27	380(7)	174(5)	121.6(0.6)	125(7)	272(11)	241(13)
11	28	381(6)	175(5)	131.7(0.6)	115(8)	251(10)	223(12)
11	29	417(9)	191(5)	141.8(0.7)	128(8)	279(11)	248(13)
11	30	404(10)	186(5)	151.8(0.7)	107(9)	232(11)	206(14)
11	31	394(15)	182(5)	161.9(0.7)	83(11)	180(15)	159(19)
11	32	419(39)	192(6)	172.0(0.8)	85(13)	186(29)	166(33)
12	28	389(19)	177(5)	103.1(0.5)	144(7)	317(20)	282(23)
12	29	353(17)	162(5)	113.1(0.5)	116(7)	252(20)	224(24)
12	30	416(16)	190(5)	123.2(0.6)	145(7)	317(20)	282(23)
12	31	398(7)	182(5)	133.3(0.6)	123(7)	270(8)	241(9)
12	32	370(8)	170(4)	143.4(0.7)	91(8)	199(10)	177(12)
12	33	376(13)	173(4)	153.5(0.7)	79(10)	172(13)	153(15)
13	31	398(18)	181(5)	102.2(0.5)	149(5)	328(8)	292(9)

**Table C.2 – continued from previous page**

Z	A	$\sigma(P)$ (MeV/c)	$\sigma(E)$ (MeV)	$\sigma_{dE}$ MeV	${}^1\sigma_N(E)$ MeV	${}^1\sigma_N(P)$ (MeV/c)	$\sigma_N(P)$ (MeV/c)
13	32	325(10)	149(4)	112.3(0.5)	98(6)	214(14)	190(16)
13	33	330(8)	152(4)	122.3(0.6)	89(6)	195(8)	173(10)
13	34	392(19)	179(5)	132.4(0.6)	121(7)	264(16)	235(18)
13	35	359(13)	165(4)	142.5(0.7)	82(8)	179(11)	159(13)
13	36	422(36)	192(5)	152.6(0.7)	116(9)	256(28)	228(33)
14	33	329(9)	150(4)	88.7(0.4)	120(4)	265(8)	236(10)
14	34	322(50)	147(6)	98.8(0.5)	109(9)	238(65)	212(74)
14	35	280(11)	129(3)	108.9(0.5)	68(6)	149(12)	132(14)
14	36	322(10)	148(3)	119.0(0.5)	87(6)	191(8)	169(9)
14	37	356(25)	162(4)	129.1(0.6)	98(7)	216(17)	192(19)
15	35	281(10)	128(3)	72.8(0.3)	105(4)	231(7)	206(8)
15	36	313(7)	142(3)	82.9(0.4)	116(4)	255(4)	227(5)
15	37	244(12)	112(3)	93.0(0.4)	63(5)	137(16)	121(19)

### C.1.3 Parallel Momentum Transfer

Table C.3: Parallel momentum transferred from the reaction of  ${}^{40}\text{Ar} + {}^9\text{Be}$ . All units are in MeV.

Z	A	Lab Frame		Projectile Frame	
		$\langle P \rangle$	${}^1\langle P^{corr} \rangle$	${}^1\langle P^{corr} \rangle$	${}^1\langle P' \rangle$
4	10	4952(93)	5010(69)	-31(84)	-31(85)
4	11	5434(16)	5492(26)	-51(41)	-47(37)
4	12	5690(22)	5753(31)	-266(47)	-224(40)
5	12	5983(12)	6072(22)	16(39)	13(33)
5	13	6384(18)	6475(27)	-73(45)	-57(35)
5	14	6836(26)	6929(33)	-118(51)	-85(37)
5	15	7188(12)	7285(31)	-249(52)	-168(35)
6	14	6929(11)	7059(23)	-4(44)	-3(32)
6	15	7395(16)	7525(27)	-37(48)	-25(33)
6	16	7764(16)	7899(29)	-152(52)	-96(33)
6	17	8251(18)	8386(32)	-168(56)	-100(34)
6	18	8661(11)	8798(33)	-249(59)	-140(33)
6	19	9146(28)	9283(41)	-266(67)	-142(35)
7	16	7871(19)	8049(28)	-20(51)	-13(32)
7	17	8325(26)	8505(33)	-63(57)	-37(34)

<sup>1</sup> Widths are corrected for the broadening due to energy straggling.

**Table C.3 – continued from previous page**

Z	A	Lab Frame		Projectile Frame	
		$\langle P \rangle$	${}^1\langle P^{corr} \rangle$	${}^1\langle P^{corr} \rangle$	${}^1\langle P' \rangle$
7	18	8751(19)	8933(31)	-130(57)	-73(32)
7	19	9275(15)	9456(32)	-114(59)	-61(32)
7	20	9672(19)	9857(35)	-205(64)	-104(32)
7	21	10076(14)	10264(37)	-292(67)	-141(32)
7	22	10601(29)	10788(43)	-275(74)	-126(34)
8	19	9228(12)	9465(29)	-106(58)	-56(31)
8	20	9651(13)	9892(31)	-175(61)	-88(31)
8	21	10107(21)	10350(36)	-216(66)	-104(32)
8	22	10636(22)	10876(38)	-196(70)	-90(32)
8	23	11060(29)	11303(42)	-265(75)	-117(33)
8	24	11479(41)	11725(50)	-338(83)	-143(35)
9	21	10111(27)	10415(39)	-158(68)	-76(33)
9	22	10694(33)	10993(43)	-93(73)	-43(34)
9	23	11144(16)	11446(36)	-139(70)	-61(31)
9	24	11619(17)	11921(38)	-165(73)	-69(31)
9	25	12127(25)	12429(42)	-162(79)	-66(32)
9	26	12502(26)	12809(44)	-272(82)	-106(32)
9	27	12966(53)	13274(59)	-307(96)	-115(36)
10	24	11515(14)	11892(38)	-190(74)	-80(31)
10	25	12085(24)	12458(42)	-136(78)	-55(32)
10	26	12528(17)	12903(41)	-188(80)	-73(31)
10	27	12909(39)	13291(52)	-291(90)	-109(34)
10	28	13476(40)	13853(53)	-240(93)	-87(33)
10	29	13792(94)	14178(90)	-400(127)	-139(44)
10	30	14555(95)	14927(91)	-183(129)	-62(44)
11	26	12484(14)	12939(42)	-157(80)	-61(31)
11	27	12981(24)	13435(46)	-164(85)	-61(32)
11	28	13488(22)	13941(46)	-163(87)	-59(31)
11	29	13917(24)	14373(48)	-226(91)	-79(32)
11	30	14482(26)	14934(50)	-177(94)	-60(32)
11	31	15006(38)	15457(56)	-161(100)	-53(33)
11	32	15379(72)	15835(78)	-272(120)	-86(38)
11	33	15928(100)	16381(98)	-235(140)	-72(43)
12	28	13348(44)	13894(60)	-204(98)	-74(36)
12	29	13967(47)	14503(62)	-112(102)	-39(35)
12	30	14361(47)	14904(63)	-203(104)	-69(35)
12	31	14812(18)	15358(51)	-248(96)	-81(32)
12	32	15433(24)	15970(53)	-153(100)	-48(32)
12	33	15877(33)	16417(57)	-203(105)	-62(32)
13	31	14760(19)	15401(55)	-210(99)	-68(33)
13	32	15409(36)	16037(61)	-94(106)	-30(34)
13	33	15882(21)	16512(56)	-120(104)	-37(32)
13	34	16292(42)	16928(66)	-198(113)	-59(34)

**Table C.3 – continued from previous page**

Z	A	<b>Lab Frame</b>		<b>Projectile Frame</b>	
		$\langle P \rangle$	${}^1\langle P_{corr} \rangle$	${}^1\langle P_{corr} \rangle$	${}^1\langle P' \rangle$
13	35	16833(31)	17465(61)	-169(112)	-49(32)
13	36	17125(79)	17771(90)	-344(138)	-97(39)
14	33	15701(21)	16443(62)	-181(108)	-55(33)
14	34	16268(173)	17003(171)	-132(216)	-39(64)
14	35	16870(33)	17596(66)	-54(115)	-16(33)
14	36	17273(22)	18006(63)	-137(115)	-39(32)
14	37	17615(47)	18360(75)	-270(127)	-74(35)
15	35	16674(19)	17520(68)	-121(117)	-35(34)
15	36	17089(11)	17942(68)	-193(118)	-54(33)
15	37	17785(48)	18620(80)	-41(130)	-11(36)
15	38	18221(21)	19060(69)	-97(123)	-26(33)

#### C.1.4 Asymmetric factor

Table C.4: The asymmetric term to the parallel momentum widths from the reaction of  ${}^{40}\text{Ar} + {}^9\text{Be}$ .

Z	A	a	Z	A	a
4	10	-(-)	10	25	364(90)
4	11	618(147)	10	26	265(81)
4	12	117(152)	10	27	771(606)
5	12	-(-)	10	28	220(294)
5	13	178(131)	10	29	-(-)
5	14	523(222)	10	30	-(-)
5	15	-(-)	11	26	-(-)
6	14	-(-)	11	27	-(-)
6	15	354(91)	11	28	371(114)
6	16	126(60)	11	29	519(134)
6	17	270(91)	11	30	413(152)
6	18	-(-)	11	31	683(317)
6	19	-(-)	11	32	-(-)
7	16	-(-)	12	28	-(-)
7	17	296(155)	12	29	566(224)
7	18	215(77)	12	30	116(246)
7	19	648(107)	12	31	-(-)
7	20	192(81)	12	32	563(151)

<sup>1</sup> Corrected for the broadening due to energy straggling.

**Table C.4 – continued from previous page**

Z	A	a	Z	A	a
7	21	-(-)	12	33	-(-)
7	22	-(-)	13	31	-(-)
8	19	-(-)	13	32	447(111)
8	20	-(-)	13	33	297(78)
8	21	169(94)	13	34	454(367)
8	22	457(119)	13	35	362(162)
8	23	134(178)	13	36	-(-)
8	24	-(-)	14	33	-(-)
9	21	-(-)	14	34	217(404)
9	22	448(163)	14	35	336(107)
9	23	293(64)	14	36	212(101)
9	24	436(88)	14	37	-(-)
9	25	639(190)	15	35	-(-)
9	26	-(-)	15	36	-(-)
9	27	-(-)	15	37	414(203)
10	24	-(-)			

## C.2 Fragments produced from the fragmentation

of  $^{40}\text{Ar} + ^{nat}\text{Ni}$

### C.2.1 Cross Section

Table C.5: Reaction Cross Sections of  $^{40}\text{Ar} + ^{nat}\text{Ni}$ .

Z	A	$\sigma$	EPAX	DIT+GEMINI	ISBEL+GEMINI
4	10	5.66(0.67)E+0	1.94E+00	1.57(0.02)E+01	1.96(0.04)E+1
4	11	3.76(0.45)E-1	3.48E-01	4.26(0.25)E-01	1.92(0.12)E+0
4	12	9.87(1.78)E-2	4.14E-02	2.12(0.18)E-01	3.16(0.48)E-1
5	12	2.94(0.35)E+0	2.56E+00	2.60(0.06)E+00	1.24(0.03)E+1
5	13	1.08(0.06)E+0	5.04E-01	7.91(0.34)E-01	3.21(0.15)E+0
5	14	5.46(0.44)E-2	6.62E-02	4.20(0.79)E-02	3.31(0.49)E-1
5	15	1.66(0.20)E-2	6.19E-03	2.25(0.58)E-02	1.22(0.30)E-1
6	14	4.79(0.57)E+0	3.41E+00	1.03(0.01)E+01	1.65(0.03)E+1
6	15	6.74(0.45)E-1	7.40E-01	4.13(0.25)E-01	1.18(0.09)E+0
6	16	1.84(0.11)E-1	1.08E-01	5.28(0.28)E-01	6.83(0.70)E-1
6	17	1.42(0.10)E-2	1.12E-02	7.50(3.40)E-03	5.75(2.03)E-2
6	18	3.88(0.59)E-3	8.74E-04	6.00(3.00)E-03	7.19(7.19)E-3
7	17	1.10(0.13)E+0	1.10E+00	1.28(0.04)E+00	3.53(0.16)E+0

Table C.5 – continued from previous page

Z	A	$\sigma$	EPAX	DIT+GEMINI	ISABEL+GEMINI
7	18	1.92(0.12)E-1	1.77E-01	1.34(0.14)E-01	5.11(0.61)E-1
7	19	4.76(0.27)E-2	2.06E-02	2.85(0.65)E-02	7.91(2.39)E-2
7	20	3.41(0.40)E-3	1.80E-03	1.50(1.50)E-03	1.44(1.02)E-2
7	21	5.45(0.90)E-4	1.23E-04	-(-)	7.19(7.19)E-3
8	19	8.91(1.06)E-1	1.63E+00	1.17(0.04)E+00	1.98(0.12)E+0
8	20	3.09(0.20)E-1	2.94E-01	7.64(0.34)E-01	1.13(0.09)E+0
8	21	3.65(0.21)E-2	3.83E-02	1.80(0.52)E-02	8.63(2.49)E-2
8	22	5.15(0.35)E-3	3.77E-03	1.20(0.42)E-02	5.03(1.90)E-2
8	23	1.45(0.18)E-4	2.91E-04	-(-)	1.44(1.02)E-2
8	24	9.42(2.72)E-6	1.80E-05	-(-)	-(-)
9	21	1.83(0.22)E+0	2.44E+00	1.68(0.05)E+00	4.41(0.18)E+0
9	22	3.78(0.36)E-1	4.92E-01	2.13(0.18)E-01	8.77(0.79)E-1
9	23	8.46(0.50)E-2	7.18E-02	6.75(1.01)E-02	2.30(0.41)E-1
9	24	6.71(0.52)E-3	7.95E-03	9.00(3.70)E-03	5.03(1.90)E-2
9	25	6.64(0.67)E-4	6.94E-04	-(-)	1.44(1.02)E-2
9	26	4.10(0.53)E-5	4.90E-05	-(-)	-(-)
9	27	2.58(0.45)E-6	2.87E-06	-(-)	-(-)
10	24	5.38(0.65)E-1	8.23E-01	1.12(0.04)E+00	1.80(0.11)E+0
10	25	6.32(0.44)E-2	1.35E-01	5.40(0.90)E-02	8.63(2.49)E-2
10	26	1.16(0.08)E-2	1.69E-02	1.65(0.50)E-02	5.03(1.90)E-2
10	27	4.64(0.69)E-4	1.67E-03	3.00(2.10)E-03	-(-)
10	28	1.33(0.22)E-4	1.34E-04	4.50(2.60)E-03	-(-)
10	29	5.70(1.04)E-6	8.99E-06	-(-)	-(-)
10	30	8.50(1.90)E-7	5.12E-07	-(-)	-(-)
11	26	5.57(0.70)E-1	1.38E+00	4.08(0.25)E-01	9.64(0.83)E-1
11	27	1.53(0.15)E-1	2.55E-01	1.04(1.32)E-01	4.24(0.55)E-1
11	28	1.77(0.12)E-2	3.61E-02	4.50(2.60)E-03	7.19(7.19)E-3
11	29	3.49(0.37)E-3	4.05E-03	6.00(3.00)E-03	-(-)
11	30	3.10(0.37)E-4	3.71E-04	-(-)	-(-)
11	31	3.81(0.54)E-5	2.84E-05	-(-)	-(-)
12	28	9.45(1.22)E-1	2.30E+00	1.62(0.05)E+0	2.45(0.13)E+0
12	29	1.92(0.24)E-1	4.82E-01	2.99(0.21)E-01	1.37(0.31)E-1
12	30	5.28(0.63)E-2	7.73E-02	3.02(0.21)E-01	8.63(2.49)E-2
12	31	4.62(2.33)E-3	9.86E-03	2.70(2.70)E-03	7.19(7.19)E-3
12	32	7.85(0.82)E-4	1.03E-03	-(-)	-(-)
12	33	3.24(0.51)E-5	9.27E-05	-(-)	-(-)
12	34	4.92(1.22)E-6	7.49E-06	-(-)	-(-)
12	35	2.10(1.72)E-7	7.49E-08	-(-)	-(-)
13	31	4.10(0.82)E-1	9.07E-01	9.26(0.37)E-01	6.40(0.68)E-1
13	32	5.66(0.67)E-2	1.65E-01	1.35(0.45)E-02	1.37(0.31)E-1
13	33	1.55(0.13)E-2	2.45E-02	6.00(3.00)E-03	4.31(1.76)E-2
13	34	1.51(0.18)E-3	3.11E-03	-(-)	-(-)
13	35	2.20(0.34)E-4	3.32E-04	-(-)	-(-)
13	36	1.15(0.26)E-5	3.32E-06	-(-)	-(-)

Table C.5 – continued from previous page

Z	A	$\sigma$	EPAX	DIT+GEMINI	ISABEL+GEMINI
14	33	3.99(0.52)E-1	1.72E+00	3.27(0.22)E-01	7.69(0.74)E-1
14	34	1.34(0.14)E-1	3.74E-01	6.00(0.95)E-02	2.80(0.45)E-1
14	35	1.38(0.18)E-2	6.66E-02	-(-)	7.19(7.19)E-3
14	36	2.83(0.40)E-3	8.89E-03	-(-)	-(-)
14	37	1.98(0.36)E-4	8.89E-05	-(-)	-(-)
14	38	8.37(2.49)E-6	1.78E-07	-(-)	-(-)
15	35	1.39(0.19)E+0	3.47E+00	3.41(0.23)E-0	3.59(0.16)E+0
15	36	2.54(0.46)E-1	8.69E-01	2.10(0.56)E-02	4.31(0.56)E-1
15	37	5.37(1.14)E-2	1.64E-01	6.60(0.99)E-02	4.31(1.76)E-2
16	41	2.11(0.32)E-3	1.97E-08	-(-)	-(-)

## C.2.2 Parallel Momentum Width

 Table C.6: Parallel momentum width from the reaction of  $^{40}\text{Ar} + \text{natNi}$ .

Z	A	Lab Frame				Projectile Frame
		$\sigma(P)$ (MeV/c)	$\sigma(E)$ (MeV)	$\sigma_{dE}$ MeV	${}^1\sigma_N(E)$ MeV	
4	10	324(4)	151(11)	78.6(0.3)	128(13)	277(16)
4	11	409(9)	188(13)	88.4(0.4)	165(15)	361(19)
4	12	384(41)	177(12)	98.2(0.4)	148(15)	320(34)
5	12	333(4)	156(10)	87.3(0.3)	129(12)	276(13)
5	13	344(4)	160(9)	97.1(0.4)	128(12)	274(13)
5	14	386(10)	179(10)	106.9(0.4)	144(13)	310(19)
5	15	516(18)	238(12)	116.7(0.5)	208(14)	450(15)
6	14	327(3)	153(8)	93.6(0.4)	121(10)	259(10)
6	15	343(4)	160(8)	103.4(0.4)	122(11)	262(12)
6	16	392(6)	181(9)	113.2(0.4)	142(11)	307(12)
6	17	445(11)	206(9)	123.0(0.5)	165(12)	357(15)
6	18	522(47)	243(11)	132.8(0.5)	204(13)	438(19)
7	17	376(3)	174(8)	107.2(0.4)	136(10)	295(8)
7	18	405(7)	187(8)	117.0(0.5)	146(10)	316(12)
7	19	416(5)	192(8)	126.8(0.5)	144(10)	312(11)
7	20	490(7)	225(8)	136.6(0.5)	179(11)	390(8)
7	21	578(51)	268(10)	146.4(0.6)	225(12)	484(21)
8	19	370(4)	171(7)	108.7(0.4)	132(9)	285(8)
8	20	373(4)	173(7)	118.5(0.5)	125(9)	271(10)
						240(13)

Table C.6 – continued from previous page

Z	A	$\sigma(P)$ (MeV/c)	$\sigma(E)$ (MeV)	$\sigma_{dE}$ MeV	${}^1\sigma_N(E)$ MeV	${}^1\sigma_N(P)$ (MeV/c)	$\sigma_N(P)$ (MeV/c)
8	21	418(6)	192(7)	128.3(0.5)	143(9)	311(10)	277(13)
8	22	407(7)	188(7)	138.1(0.5)	127(10)	276(11)	245(14)
8	23	492(12)	226(8)	147.9(0.6)	170(10)	372(15)	330(18)
8	24	559(136)	256(10)	157.7(0.6)	202(13)	440(46)	391(52)
9	21	471(17)	215(8)	107.7(0.4)	186(9)	408(11)	363(13)
9	22	372(8)	172(6)	117.5(0.5)	125(9)	271(16)	241(18)
9	23	393(5)	181(6)	127.3(0.5)	129(8)	279(9)	248(11)
9	24	422(11)	194(6)	137.1(0.5)	138(9)	299(13)	265(16)
9	25	439(20)	202(7)	146.9(0.6)	139(10)	302(18)	268(21)
9	26	501(18)	230(7)	156.7(0.6)	168(10)	366(19)	325(22)
9	27	556(50)	257(8)	166.5(0.7)	196(11)	424(32)	376(37)
10	24	378(4)	173(5)	114.1(0.5)	130(7)	284(6)	253(8)
10	25	372(6)	171(5)	123.9(0.5)	118(8)	256(10)	228(12)
10	26	400(7)	184(5)	133.7(0.5)	127(8)	275(10)	245(12)
10	27	418(16)	192(6)	143.5(0.6)	128(9)	279(20)	247(24)
10	28	429(31)	198(6)	153.3(0.6)	125(10)	271(25)	241(29)
10	29	475(43)	218(7)	163.1(0.6)	144(11)	314(32)	280(37)
10	30	532(90)	242(7)	172.9(0.7)	169(10)	371(32)	331(37)
11	26	398(8)	182(5)	108.3(0.4)	146(7)	320(9)	285(10)
11	27	339(8)	157(5)	118.1(0.5)	103(7)	223(13)	198(15)
11	28	374(6)	172(5)	127.9(0.5)	115(7)	250(8)	222(10)
11	29	438(19)	201(6)	137.7(0.5)	146(8)	319(18)	284(20)
11	30	392(14)	181(5)	147.5(0.6)	104(9)	226(14)	201(17)
11	31	396(23)	183(5)	157.3(0.6)	93(10)	202(14)	179(17)
12	28	397(12)	180(5)	100.1(0.4)	150(6)	330(14)	294(16)
12	29	308(5)	141(4)	109.9(0.4)	89(6)	193(4)	172(6)
12	30	322(8)	147(4)	119.7(0.5)	86(6)	188(5)	167(7)
12	31	402(64)	183(7)	129.5(0.5)	130(9)	285(50)	254(57)
12	32	365(12)	168(4)	139.3(0.6)	94(8)	204(13)	181(15)
12	33	388(22)	179(5)	149.1(0.6)	99(8)	215(16)	191(19)
12	34	424(69)	194(6)	158.9(0.6)	111(11)	243(47)	216(54)
12	35	406(169)	186(9)	168.7(0.7)	78(22)	170(105)	151(120)
13	31	328(27)	150(4)	99.3(0.4)	113(6)	247(21)	219(24)
13	32	314(10)	144(4)	109.1(0.4)	94(6)	205(13)	182(15)
13	33	336(9)	154(4)	118.9(0.5)	98(6)	214(8)	191(9)
13	34	324(11)	149(4)	128.6(0.5)	75(7)	163(12)	145(14)
13	35	434(34)	199(5)	138.4(0.5)	143(6)	312(12)	277(14)
13	36	356(36)	163(4)	148.2(0.6)	68(10)	148(20)	132(23)
14	33	324(5)	147(3)	86.2(0.3)	119(4)	262(6)	234(7)
14	34	289(7)	132(3)	96.0(0.4)	91(4)	199(7)	177(8)
14	35	361(14)	165(4)	105.8(0.4)	126(5)	277(8)	246(10)
14	36	285(13)	131(3)	115.6(0.5)	61(7)	133(12)	119(14)
14	37	369(36)	167(4)	125.4(0.5)	110(7)	243(26)	217(30)

**Table C.6 – continued from previous page**

Z	A	$\sigma(P)$ (MeV/c)	$\sigma(E)$ (MeV)	$\sigma_{dE}$ MeV	${}^1\sigma_N(E)$ MeV	${}^1\sigma_N(P)$ (MeV/c)	$\sigma_N(P)$ (MeV/c)
15	35	267(10)	121(3)	70.7(0.3)	99(3)	217(4)	193(5)
15	36	249(13)	114(3)	80.5(0.3)	80(4)	176(11)	156(13)
15	37	217(13)	100(3)	90.3(0.4)	42(6)	92(15)	82(18)
16	41	247(16)	111(2)	92.0(0.4)	63(4)	139(9)	124(10)

### C.2.3 Parallel Momentum Transfer

Z	A	Lab Frame		Projectile Frame	
		$\langle P \rangle$	${}^1\langle P^{corr} \rangle$	${}^1\langle P^{corr} \rangle$	${}^1\langle P' \rangle$
4	10	4883(13)	4942(29)	-89(41)	-90(41)
4	11	5298(18)	5359(34)	-166(47)	-153(43)
4	12	5860(45)	5920(44)	-116(58)	-98(49)
5	12	5899(12)	5990(30)	-54(44)	-46(37)
5	13	6336(10)	6430(34)	-112(49)	-87(38)
5	14	6755(23)	6850(40)	-185(56)	-134(41)
5	15	7279(18)	7373(43)	-169(60)	-114(41)
6	14	6857(16)	6989(32)	-63(49)	-45(36)
6	15	7291(12)	7426(35)	-122(53)	-83(36)
6	16	7764(11)	7900(38)	-150(57)	-95(36)
6	17	8254(17)	8389(42)	-162(63)	-97(37)
6	18	8842(35)	8974(50)	-91(71)	-51(40)
7	17	8240(12)	8424(36)	-132(57)	-78(34)
7	18	8726(12)	8910(39)	-148(61)	-83(34)
7	19	9157(10)	9343(42)	-211(65)	-113(35)
7	20	9655(12)	9841(45)	-217(70)	-110(35)
7	21	10238(37)	10420(54)	-150(79)	-72(38)
8	19	9183(16)	9423(38)	-140(62)	-75(33)
8	20	9654(12)	9895(40)	-168(65)	-85(33)
8	21	10159(12)	10399(43)	-169(69)	-82(33)
8	22	10610(14)	10852(46)	-214(74)	-99(34)
8	23	11064(27)	11307(52)	-258(80)	-113(35)
8	24	11530(86)	11774(78)	-291(106)	-123(45)
9	21	10022(18)	10332(41)	-228(68)	-110(33)
9	22	10600(12)	10905(42)	-167(70)	-77(32)
9	23	11084(13)	11389(44)	-185(74)	-82(32)

<sup>1</sup> Widths are corrected for the broadening due to energy straggling.

**Table C.7 – continued from previous page**

Z	A	<b>Lab Frame</b>		<b>Projectile Frame</b>	
		$\langle P \rangle$	${}^1\langle P^{corr} \rangle$	${}^1\langle P^{corr} \rangle$	${}^1\langle P' \rangle$
9	24	11605(14)	11909(47)	-172(78)	-73(33)
9	25	12103(21)	12407(51)	-178(82)	-72(33)
9	26	12498(38)	12806(59)	-270(91)	-105(35)
9	27	13131(70)	13432(74)	-163(106)	-61(40)
10	24	11526(15)	11904(45)	-176(76)	-74(32)
10	25	12025(15)	12402(47)	-182(79)	-74(32)
10	26	12509(15)	12886(49)	-199(83)	-78(32)
10	27	13013(38)	13390(58)	-200(92)	-75(34)
10	28	13583(31)	13955(57)	-146(93)	-53(33)
10	29	13914(74)	14295(78)	-292(113)	-102(39)
10	30	14256(74)	14643(80)	-429(116)	-145(39)
11	26	12452(21)	12910(50)	-178(83)	-69(32)
11	27	12993(15)	13447(50)	-150(85)	-56(32)
11	28	13473(16)	13928(52)	-170(88)	-61(32)
11	29	13940(19)	14396(54)	-202(92)	-71(32)
11	30	14472(26)	14926(58)	-180(96)	-61(33)
11	31	15064(34)	15458(62)	-155(101)	-51(33)
12	28	13301(1)	13852(51)	-237(87)	-86(32)
12	29	13961(10)	14500(52)	-111(90)	-39(31)
12	30	14365(12)	14909(55)	-194(94)	-66(32)
12	31	14868(17)	15411(57)	-196(97)	-64(32)
12	32	15421(24)	15960(60)	-157(101)	-50(32)
12	33	16005(54)	16538(73)	-92(113)	-28(35)
12	34	16270(125)	16817(116)	-291(156)	-87(46)
12	35	16754(287)	17302(232)	-308(283)	-89(82)
13	31	14833(14)	15470(57)	-145(98)	-47(32)
13	32	15378(20)	16010(60)	-113(101)	-36(32)
13	33	15847(18)	16481(61)	-142(104)	-44(32)
13	34	16308(20)	16944(63)	-179(107)	-53(32)
13	35	16867(33)	17499(68)	-134(112)	-39(32)
13	36	17292(56)	17928(78)	-201(123)	-57(35)
14	33	15684(14)	16429(63)	-188(105)	-58(32)
14	34	16303(15)	17037(64)	-97(107)	-29(32)
14	35	16738(23)	17476(67)	-154(112)	-45(32)
14	36	17286(18)	18020(67)	-120(113)	-34(32)
14	37	17493(74)	18249(91)	-362(137)	-99(37)
14	38	18170(79)	18911(95)	-223(141)	-60(38)
15	35	16641(12)	17493(68)	-140(113)	-40(33)
15	36	17189(22)	18035(71)	-106(117)	-30(33)
15	37	17760(34)	18599(75)	-54(121)	-15(33)
16	41	19317(27)	20303(82)	-330(135)	-81(33)

### C.2.4 Asymmetric factor

Table C.8: The asymmetric term to the parallel momentum widths from the reaction of  $^{40}\text{Ar} + ^{nat}\text{Ni}$ .

Z	A	a	Z	A	a
4	10	-(-)	10	28	532.09(455.14)
4	11	-(-)	10	29	-(-)
4	12	505.75(282.47)	10	30	-(-)
5	12	-(-)	11	26	-(-)
5	13	403.75(96.57)	11	27	796.77(142.15)
5	14	582.96(169.55)	11	28	148.32(92.23)
5	15	-(-)	11	29	-(-)
6	14	-(-)	11	30	516.75(293.24)
6	15	688.53(135.19)	11	31	-(-)
6	16	194.16(85.41)	12	28	-(-)
6	17	369.6(113.79)	12	29	-(-)
6	18	213.1(171.79)	12	30	-(-)
7	17	-(-)	12	31	-(-)
7	18	226.15(85.85)	12	32	552.09(171.56)
7	19	314.86(75.72)	12	33	-(-)
7	20	-(-)	12	34	-(-)
7	21	118.71(185.44)	12	35	-(-)
8	19	-(-)	13	31	612.39(240.02)
8	20	471(87.12)	13	32	437.36(119.24)
8	21	118.48(84.1)	13	33	306.36(103.15)
8	22	397.08(102.22)	13	34	577.97(214.4)
8	23	-(-)	13	35	-(-)
8	24	-(-)	13	36	-(-)
9	21	-(-)	14	33	-(-)
9	22	645.98(174.91)	14	34	352.12(74.52)
9	23	257.37(72.39)	14	35	-(-)
9	24	340.99(138.46)	14	36	489.36(284.97)
9	25	541.44(231.07)	14	37	-(-)
9	26	-(-)	14	38	-(-)
9	27	-(-)	15	35	-(-)
10	24	-(-)	15	36	515.66(93.43)
10	25	401.22(95.37)	15	37	700.16(202.09)
10	26	328.75(122.56)	16	41	-(-)
10	27	433.03(360.93)			

<sup>1</sup> Corrected for the broadening due to energy straggling.

### C.3 Fragments produced from the fragmentation of $^{40}\text{Ar} + ^{181}\text{Ta}$

#### C.3.1 Cross Section

Table C.9: Reaction Cross Sections of  $^{40}\text{Ar} + ^{181}\text{Ta}$ .

Z	A	$\sigma(\text{mb})$	EPAX	DIT+GEMINI	ISABEL+GEMINI
4	10	0.97(0.10)E+1	2.64E+00	2.37(0.03)E+01	1.13(0.02)E+1
4	11	6.20(0.71)E-1	4.72E-01	7.78(0.46)E-01	1.08(0.07)E+0
4	12	1.92(0.54)E-1	5.62E-02	3.38(0.3)E-01	1.39(0.23)E-1
5	12	4.89(0.53)E+0	3.48E+00	4.13(0.11)E+00	8.58(0.19)E+0
5	13	2.03(0.16)E+0	6.84E-01	1.27(0.59)E+00	1.90(0.09)E+0
5	14	1.04(0.10)E-1	8.99E-02	7.02(1.38)E-02	1.98(0.28)E-1
5	15	3.13(0.67)E-2	8.40E-03	2.16(0.76)E-02	4.36(1.32)E-2
6	14	9.89(1.21)E+0	4.63E+00	1.52(0.2)E+01	1.29(0.02)E+1
6	15	1.26(0.15)E+0	1.00E+00	6.26(0.41)E-01	7.78(0.56)E-1
6	16	3.38(0.37)E-1	1.46E-01	9.261(0.5)E-0	3.85(0.39)E-1
6	17	2.82(0.22)E-2	1.52E-02	2.7(0.85)E-02	2.38(0.97)E-2
6	18	7.42(0.98)E-3	1.19E-03	1.62(0.66)E-02	3.97(3.97)E-3
6	19	1.75(0.25)E-4	7.16E-05	-(-)	-(-)
7	17	1.91(0.21)E+0	1.49E+00	2(0.07)E+00	2.61(0.10)E+0
7	18	3.69(0.27)E-1	2.41E-01	1.76(0.22)E-01	3.41(0.37)E-1
7	19	9.15(0.67)E-2	2.80E-02	7.83(1.45)E-02	6.74(1.64)E-2
7	20	7.84(0.68)E-3	2.45E-03	-(-)	-(-)
7	21	1.17(0.14)E-3	1.67E-04	-(-)	-(-)
7	22	3.63(0.53)E-5	9.12E-06	-(-)	-(-)
8	19	1.63(0.19)E+0	2.22E+00	2(0.07)E+00	1.69(0.08)E+0
8	20	5.91(0.68)E-1	4.00E-01	1.33(0.06)E+00	7.82(0.56)E-1
8	21	6.84(0.51)E-2	5.20E-02	4.59(1.11)E-02	4.36(1.32)E-2
8	22	1.06(0.09)E-2	5.12E-03	1.89(0.71)E-02	3.17(1.12)E-2
8	23	3.09(0.31)E-4	3.94E-04	-(-)	3.97(3.97)E-3
8	24	2.79(0.40)E-4	2.45E-05	-(-)	-(-)
9	21	3.82(0.41)E+0	3.32E+00	2.56(0.82)E+00	3.53(0.12)E+0
9	22	7.12(0.80)E-1	6.67E-01	3.97(0.33)E-01	5.16(0.45)E-1
9	23	1.61(0.12)E-1	9.74E-02	1.27(0.19)E-01	1.75(0.26)E-1
9	24	1.36(0.11)E-2	1.08E-02	5.4(3.8)E-03	7.93(5.61)E-3
9	25	1.39(0.14)E-3	9.42E-04	-(-)	7.93(5.61)E-3
9	26	1.19(0.17)E-4	6.65E-05	-(-)	-(-)
9	27	8.91(1.47)E-6	3.89E-06	-(-)	-(-)
10	24	9.46(1.09)E-1	1.12E+00	1.77(0.07)E+00	1.17(0.07)E+0
10	25	1.18(0.10)E-1	1.83E-01	8.91(1.55)E-02	6.35(1.59)E-2
10	26	2.33(0.19)E-2	2.30E-02	1.62(0.66)E-02	1.19(0.69)E-2
10	27	8.32(0.99)E-4	2.27E-03	-(-)	3.97(3.97)E-3

**Table C.9 – continued from previous page**

Z	A	$\sigma$ (mb)	EPAX	DIT+GEMINI	ISABEL+GEMINI
10	28	3.18(0.68)E-4	1.82E-04	-(-)	-(-)
10	29	1.10(0.20)E-5	1.22E-05	-(-)	-(-)
10	30	1.67(0.46)E-6	6.94E-07	-(-)	-(-)
11	26	1.18(0.13)E+0	1.87E+00	6.99(4.42)E-01	7.22(0.54)E-1
11	27	3.10(0.30)E-1	3.46E-01	1.78(0.22)E-01	1.94(0.28)E-1
11	28	3.55(0.30)E-2	4.90E-02	1.62(0.66)E-02	1.19(0.69)E-2
11	29	7.18(0.68)E-3	5.50E-03	8.1(4.7)E-03	-(-)
11	30	6.97(0.84)E-4	5.04E-04	-(-)	-(-)
11	31	1.21(0.27)E-4	3.86E-05	-(-)	-(-)
12	29	2.56(0.26)E-1	6.54E-01	4.56(0.35)E-01	6.74(1.64)E-2
12	30	7.09(0.65)E-2	1.05E-01	5.08(0.37)E-01	4.36(1.32)E-2
12	31	7.79(0.80)E-3	1.34E-02	2.7(2.7)E-03	-(-)
12	32	1.64(0.19)E-3	1.40E-03	-(-)	-(-)
12	33	1.26(0.19)E-4	1.26E-04	-(-)	-(-)
13	31	6.81(0.81)E-1	1.23E+00	9.61(0.51)E-01	3.61(0.38)E-1
13	32	1.03(0.09)E-1	2.24E-01	2.16(0.76)E-02	2.78(1.05)E-2
13	33	2.74(0.25)E-2	3.32E-02	-(-)	3.97(3.97)E-3
13	34	3.13(0.45)E-3	4.22E-03	-(-)	-(-)
13	35	5.87(0.77)E-4	4.51E-04	-(-)	-(-)
13	36	3.34(0.53)E-5	4.51E-06	-(-)	-(-)
14	33	7.68(0.81)E-1	2.33E+00	4.37(0.34)E-01	4.17(0.41)E-1
14	34	2.13(0.20)E-1	5.08E-01	7.56(1.43)E-02	1.15(0.21)E-1
14	35	1.92(0.28)E-2	9.04E-02	-(-)	3.97(3.97)E-3
14	36	4.24(0.79)E-3	1.21E-02	-(-)	-(-)
15	36	3.55(0.40)E-1	1.18E+00	1.13(0.18)E-01	1.83(0.27)E-1
15	37	1.04(0.10)E-1	2.23E-01	3.24(0.94)E-02	1.03(0.20)E-1
15	38	4.93(0.74)E-3	2.23E-03	-(-)	3.97(3.97)E-3
16	38	1.49(0.18)E+0	3.34E+00	1.54(0.06)E+00	1.05(0.06)E+0
16	41	5.98(0.82)E-3	2.67E-08	-(-)	-(-)

### C.3.2 Parallel Momentum Widths

Table C.10: Parallel momentum widths from the reaction  
of  $^{40}\text{Ar} + ^{181}\text{Ta}$ .

Z	A	Lab Frame				Projectile Frame
		$\sigma(P)$ (MeV/c)	$\sigma(E)$ (MeV)	$\sigma_{dE}$ MeV	${}^1\sigma_N(E)$ MeV	
4	10	292(8)	137(11)	82.1(0.3)	109(14)	234(21)
4	11	384(14)	176(12)	92.3(0.4)	149(14)	327(17)
4	12	349(50)	160(13)	102.6(0.4)	123(17)	268(69)
5	12	336(4)	156(10)	91.2(0.4)	127(12)	273(15)
5	13	340(5)	158(9)	101.4(0.4)	121(12)	260(13)
5	14	372(9)	172(10)	111.7(0.5)	130(13)	282(19)
5	15	379(41)	175(10)	121.9(0.5)	125(14)	272(40)
6	14	398(13)	182(11)	97.8(0.4)	154(13)	335(32)
6	15	385(23)	178(9)	108.0(0.4)	142(12)	307(19)
6	16	423(13)	194(9)	118.2(0.5)	154(11)	336(10)
6	17	419(8)	193(9)	128.5(0.5)	144(12)	313(15)
6	18	405(25)	188(8)	138.7(0.6)	127(12)	273(20)
6	19	432(31)	197(8)	148.9(0.6)	129(13)	283(19)
7	17	420(11)	193(9)	112.0(0.5)	157(11)	342(15)
7	18	387(5)	178(8)	122.3(0.5)	130(10)	282(10)
7	19	425(6)	195(8)	132.5(0.6)	144(11)	313(11)
7	20	428(8)	198(8)	142.7(0.6)	137(11)	296(14)
7	21	445(24)	206(8)	153.0(0.6)	138(12)	298(19)
7	22	407(23)	185(7)	163.2(0.7)	88(14)	193(12)
8	19	413(12)	189(8)	113.6(0.5)	151(10)	330(21)
8	20	427(21)	196(8)	123.8(0.5)	152(10)	331(20)
8	21	403(5)	185(7)	134.0(0.6)	128(10)	279(9)
8	22	436(7)	200(7)	144.3(0.6)	138(10)	301(12)
8	23	446(13)	205(7)	154.5(0.6)	135(11)	294(19)
8	24	449(25)	207(7)	164.7(0.7)	125(12)	272(18)
9	21	460(12)	208(7)	112.5(0.5)	175(9)	387(9)
9	22	450(17)	205(8)	122.8(0.5)	164(9)	360(18)
9	23	377(4)	174(6)	133.0(0.6)	111(9)	242(7)
9	24	420(7)	192(6)	143.2(0.6)	128(9)	280(10)
9	25	426(10)	195(6)	153.5(0.6)	121(10)	263(13)
9	26	481(19)	220(7)	163.7(0.7)	147(11)	321(27)
9	27	474(36)	218(7)	173.9(0.7)	132(12)	287(28)
10	24	427(15)	194(7)	119.2(0.5)	153(8)	337(16)
10	25	374(6)	172(5)	129.5(0.5)	113(8)	245(9)
10	26	374(6)	172(5)	139.7(0.6)	100(9)	218(8)
10	27	416(11)	190(6)	149.9(0.6)	117(9)	256(14)
10	28	407(21)	187(6)	160.2(0.7)	97(11)	211(22)
10	29	439(44)	201(7)	170.4(0.7)	106(13)	232(42)
10	30	484(71)	222(8)	180.6(0.8)	129(14)	281(55)
						250(63)

**Table C.10 – continued from previous page**

Z	A	$\sigma(P)$ (MeV/c)	$\sigma(E)$ (MeV)	$\sigma_{dE}$ MeV	${}^1\sigma_N(E)$ MeV	${}^1\sigma_N(P)$ (MeV/c)	$\sigma_N(P)$ (MeV/c)
11	26	443(11)	200(6)	113.2(0.5)	165(7)	365(5)	326(7)
11	27	404(10)	184(5)	123.4(0.5)	137(7)	299(11)	267(13)
11	28	373(7)	171(5)	133.6(0.6)	106(8)	232(8)	206(10)
11	29	386(8)	177(5)	143.9(0.6)	103(8)	224(11)	199(13)
11	30	412(10)	188(5)	154.1(0.6)	108(9)	236(10)	210(12)
11	31	433(37)	199(6)	164.3(0.7)	111(11)	243(29)	216(33)
12	29	381(11)	173(5)	114.8(0.5)	130(6)	285(11)	254(13)
12	30	349(8)	160(4)	125.1(0.5)	100(7)	218(9)	194(11)
12	31	361(10)	166(4)	135.3(0.6)	95(7)	208(10)	185(12)
12	32	368(12)	168(4)	145.5(0.6)	85(9)	185(13)	165(15)
12	33	394(18)	179(5)	155.7(0.6)	89(9)	196(15)	174(18)
13	31	365(13)	166(4)	103.7(0.4)	130(6)	285(13)	254(15)
13	32	343(7)	156(4)	113.9(0.5)	107(6)	235(7)	209(9)
13	33	332(8)	152(4)	124.2(0.5)	88(6)	191(7)	170(9)
13	34	341(15)	156(4)	134.4(0.6)	79(8)	173(13)	154(16)
13	35	449(19)	204(5)	144.6(0.6)	143(7)	316(13)	282(16)
13	36	355(35)	161(4)	154.9(0.6)	42(16)	94(23)	84(28)
14	33	367(7)	166(4)	90.1(0.4)	140(4)	309(2)	275(3)
14	34	304(7)	139(3)	100.3(0.4)	96(5)	210(6)	187(7)
14	35	333(25)	152(4)	110.5(0.5)	104(6)	229(15)	204(17)
14	36	316(28)	144(4)	120.8(0.5)	79(7)	173(15)	154(18)
15	36	266(9)	121(3)	84.1(0.3)	87(4)	191(9)	170(10)
15	37	277(6)	126(3)	94.4(0.4)	83(4)	183(6)	163(7)
15	38	299(25)	136(3)	104.6(0.4)	87(5)	190(11)	170(13)
16	38	230(7)	104(2)	65.4(0.3)	81(3)	179(7)	159(8)
16	41	282(20)	126(3)	96.1(0.4)	82(4)	183(12)	164(13)

### C.3.3 Parallel Momentum Transfer

Table C.11: Parallel momentum transferred from the reaction of  ${}^{40}\text{Ar} + {}^{181}\text{Ta}$ . All units are in MeV.

Z	A	Lab Frame		Projectile Frame	
		$\langle P \rangle$	${}^1\langle P_{corr} \rangle$	${}^1\langle P_{corr} \rangle$	${}^1\langle P' \rangle$
4	10	4936(18)	4996(39)	-34(50)	-35(51)
4	11	5270(15)	5334(44)	-181(56)	-167(51)

<sup>1</sup> Widths are corrected for the broadening due to energy straggling.

**Table C.11 – continued from previous page**

Z	A	Lab Frame		Projectile Frame	
		$\langle P \rangle$	${}^1\langle P_{corr} \rangle$	${}^1\langle P_{corr} \rangle$	${}^1\langle P' \rangle$
4	12	5663(57)	5729(52)	-277(65)	-234(55)
5	12	5873(14)	5968(42)	-65(55)	-55(46)
5	13	6349(14)	6444(47)	-90(61)	-70(47)
5	14	6787(22)	6884(52)	-146(67)	-105(49)
5	15	7264(48)	7361(59)	-169(76)	-114(51)
6	14	6715(35)	6856(47)	-171(62)	-123(45)
6	15	7300(23)	7438(50)	-101(66)	-68(45)
6	16	7695(12)	7836(54)	-194(71)	-123(45)
6	17	8234(20)	8373(59)	-165(77)	-98(46)
6	18	8766(28)	8905(64)	-140(84)	-79(47)
6	19	9079(28)	9222(69)	-304(90)	-162(48)
7	17	8175(21)	8366(52)	-171(70)	-102(42)
7	18	8710(14)	8899(56)	-145(75)	-81(42)
7	19	9147(16)	9338(60)	-202(81)	-107(43)
7	20	9699(23)	9888(65)	-161(87)	-82(44)
7	21	10195(31)	10383(70)	-168(93)	-81(45)
7	22	10482(20)	10678(74)	-354(98)	-162(45)
8	19	9091(31)	9342(56)	-198(77)	-106(41)
8	20	9618(32)	9867(60)	-180(81)	-91(41)
8	21	10117(15)	10365(62)	-185(85)	-89(41)
8	22	10570(20)	10820(66)	-227(90)	-104(42)
8	23	11100(35)	11348(72)	-205(97)	-90(43)
8	24	11605(34)	11853(76)	-205(102)	-86(43)
9	21	9908(14)	10233(57)	-302(80)	-145(38)
9	22	10505(31)	10823(62)	-225(86)	-103(40)
9	23	11110(14)	11422(63)	-141(89)	-62(39)
9	24	11515(19)	11831(68)	-224(94)	-94(40)
9	25	12029(26)	12344(72)	-216(100)	-87(40)
9	26	12424(54)	12743(80)	-308(109)	-120(42)
9	27	13034(60)	13348(85)	-219(115)	-82(43)
10	24	11419(29)	11813(64)	-240(91)	-101(38)
10	25	12044(18)	12430(66)	-140(93)	-57(38)
10	26	12532(17)	12918(69)	-153(98)	-60(38)
10	27	12928(29)	13318(74)	-245(104)	-92(39)
10	28	13524(48)	13909(81)	-167(112)	-60(40)
10	29	13871(94)	14263(96)	-300(128)	-105(44)
10	30	14404(130)	14794(110)	-275(143)	-93(48)
11	26	12293(11)	12773(65)	-281(94)	-109(37)
11	27	12890(24)	13363(69)	-205(99)	-77(37)
11	28	13462(18)	13929(72)	-150(103)	-54(37)
11	29	13923(25)	14391(76)	-186(108)	-65(38)
11	30	14352(24)	14825(79)	-248(112)	-84(38)
11	31	14921(70)	15388(91)	-195(125)	-64(41)

**Table C.11 – continued from previous page**

Z	A	<b>Lab Frame</b>		<b>Projectile Frame</b>	
		$\langle P \rangle$	${}^1\langle P_{corr} \rangle$	${}^1\langle P_{corr} \rangle$	${}^1\langle P' \rangle$
12	29	13814(24)	14376(72)	-199(104)	-69(36)
12	30	14403(22)	14959(74)	-130(108)	-44(36)
12	31	14890(25)	15446(78)	-145(112)	-47(37)
12	32	15347(32)	15904(82)	-184(118)	-58(37)
12	33	15749(40)	16312(87)	-268(124)	-82(38)
13	31	14717(32)	15379(77)	-203(111)	-66(36)
13	32	15254(18)	15912(77)	-178(113)	-56(36)
13	33	15835(19)	16486(80)	-116(117)	-35(36)
13	34	16283(35)	16937(85)	-161(123)	-48(37)
13	35	16593(36)	17259(89)	-322(128)	-93(37)
13	36	17009(62)	17680(98)	-394(138)	-111(39)
14	33	15614(5)	16384(78)	-205(115)	-63(35)
14	34	16203(15)	16964(80)	-138(118)	-41(35)
14	35	16732(41)	17489(87)	-118(126)	-34(36)
14	36	17210(43)	17968(90)	-140(130)	-39(36)
15	36	17134(25)	18006(85)	-107(126)	-30(35)
15	37	17620(16)	18492(87)	-122(128)	-33(35)
15	38	18068(33)	18944(92)	-168(134)	-45(36)
16	38	18042(19)	19035(89)	-88(132)	-23(35)
16	41	19197(36)	20219(100)	-376(147)	-93(36)

---

<sup>1</sup> Corrected for the broadening due to energy straggling.

### C.3.4 Asymmetric factor

Table C.12: The asymmetric term to the parallel momentum widths from the reaction of  $^{40}\text{Ar} + ^{181}\text{Ta}$ .

<b>Z</b>	<b>A</b>	<b>a</b>	<b>Z</b>	<b>A</b>	<b>a</b>
4	10	609.46(234.91)	10	26	523.33(95.48)
4	11	-(-)	10	27	-(-)
4	12	1186.08(693.7)	10	28	839.03(846.29)
5	12	-(-)	10	29	-(-)
5	13	577.63(117.67)	10	30	-(-)
5	14	658.15(191.9)	11	26	-(-)
5	15	788.19(305.11)	11	27	426.47(231.32)
6	14	-(-)	11	28	478.96(91.95)
6	15	757.4(249.9)	11	29	325.04(157.37)
6	16	-(-)	11	30	-(-)
6	17	392.27(104.25)	11	31	722.16(586.97)
6	18	669.35(163.74)	12	29	386.93(265.73)
6	19	-(-)	12	30	720.43(126.34)
7	17	-(-)	12	31	542.68(127.55)
7	18	427.05(88.61)	12	32	367.31(187.68)
7	19	276.16(81.89)	12	33	-(-)
7	20	734.53(158.51)	13	31	-(-)
7	21	531.58(167.27)	13	32	337.75(108.03)
7	22	-(-)	13	33	529.42(83.78)
8	19	-(-)	13	34	604.33(279.51)
8	20	456.32(267.28)	13	35	-(-)
8	21	300.94(73.73)	13	36	-(-)
8	22	359.74(128.79)	14	33	-(-)
8	23	290.1(226.3)	14	34	292.28(93.83)
8	24	-(-)	14	35	341.01(191.36)
9	21	-(-)	14	36	200.69(382.35)
9	22	332.65(434.98)	15	36	562.19(169.6)
9	23	530.87(72.64)	15	37	205(78.43)
9	24	128.81(86.19)	15	38	-(-)
9	25	519.03(187.15)	16	38	-(-)
9	26	467.84(450.33)	16	41	-(-)
9	27	-(-)	15	37	700.16(202.09)
10	24	-(-)	16	41	-(-)
10	25	570.05(108.59)			

### C.3.5 Angular Transmission

Table C.13: The angular transmission of fragments in percent as predicted by LISE.

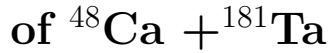
		target					target		
Z	A	<sup>9</sup> Be	<i>nat</i> Ni	<sup>181</sup> Ta	Z	A	<sup>9</sup> Be	<i>nat</i> Ni	<sup>181</sup> Ta
4	10	0.14	0.25	0.25	10	28	0.73	0.73	0.73
4	11	0.19	0.27	0.27	10	29	0.74	0.73	0.72
4	12	0.21	0.31	0.31	10	30	0.76	0.75	0.75
5	12	0.21	0.31	0.30	11	26	0.68	0.71	0.70
5	13	0.24	0.33	0.33	11	27	0.72	0.74	0.73
5	14	0.27	0.37	0.37	11	28	0.74	0.75	0.73
5	15	0.28	0.40	0.40	11	29	0.76	0.76	0.75
6	14	0.27	0.36	0.36	11	30	0.77	0.78	0.76
6	15	0.28	0.40	0.40	11	31	0.79	0.79	0.78
6	16	0.31	0.42	0.42	11	32	0.79	-	-
6	17	0.35	0.46	0.45	11	33	0.82	-	-
6	18	0.42	0.49	0.49	12	28	0.75	0.75	-
6	19	0.45	-	0.50	12	29	0.77	0.78	0.76
7	16	0.35	-	-	12	30	0.80	0.80	0.78
7	17	0.35	0.45	0.45	12	31	0.80	0.81	0.79
7	18	0.41	0.49	0.48	12	32	0.79	0.82	0.80
7	19	0.44	0.52	0.51	12	33	0.82	0.82	0.81
7	20	0.47	0.53	0.53	12	34	-	0.83	-
7	21	0.51	0.56	0.55	12	35	-	0.84	-
7	22	0.54	-	0.57	13	31	0.81	0.83	0.81
8	19	0.45	0.52	0.51	13	32	0.79	0.83	0.82
8	20	0.48	0.54	0.54	13	33	0.84	0.83	0.82
8	21	0.51	0.57	0.57	13	34	0.84	0.83	0.83
8	22	0.55	0.60	0.60	13	35	0.87	0.85	0.85
8	23	0.58	0.62	0.61	13	36	0.87	0.86	0.85
8	24	0.62	0.74	0.61	14	33	0.85	0.85	0.84
9	21	0.52	0.57	0.56	14	34	0.84	0.86	0.85
9	22	0.55	0.59	0.59	14	35	0.87	0.86	0.85
9	23	0.57	0.63	0.62	14	36	0.89	0.89	0.87
9	24	0.61	0.65	0.65	14	37	0.96	0.89	0.87
9	25	0.63	0.67	0.66	14	38	-	0.91	0.87
9	26	0.67	0.67	0.68	15	35	0.90	0.89	0.89
9	27	0.69	0.69	0.69	15	36	0.89	0.89	0.92
10	24	0.61	0.66	0.66	15	37	0.91	0.91	-
10	25	0.66	0.69	0.68	15	38	0.92	-	-
10	26	0.68	0.70	0.69	16	41	-	0.93	0.91
10	27	0.71	0.72	0.70					

# Appendix D

## Data from the Fragmenation $^{48}\text{Ca}$ with $^{181}\text{Ta}$

The following tables list the isotropic cross sections in mb for the reaction of a~128 MeV/nucleon  $^{48}\text{Ca}$  projectile with  $^{181}\text{Ta}$  (Table C.9). Only momentum distributions that could be fitted are listed below. The uncertainties quoted for the two simulations are statistical.

### D.1 Fragments produced from the fragmentation



#### D.1.1 Cross Section

Table D.1: Reaction Cross Sections of  $^{48}\text{Ca}+^{181}\text{Ta}$ .

Z	A	$\sigma$	EPAX	DIT+GEMINI	ISABEL+GEMINI
4	10	3.32(0.38)E+0	2.31E+00	1.48(0.02)E+01	2.12(0.03)E+1
4	11	4.36(0.50)E-1	5.38E-01	7.62(0.39)E-01	2.07(0.10)E+0
4	12	2.28(0.29)E-1	8.80E-02	4.50(0.30)E-01	4.32(0.47)E-1
5	12	1.99(0.23)E+0	3.04E+00	2.83(0.08)E+00	1.55(0.03)E+1
5	13	1.55(0.17)E+0	7.76E-01	1.20(0.05)E+00	4.30(0.15)E+0
5	14	1.18(0.11)E-1	1.40E-01	1.16(0.15)E-01	5.09(0.51)E-1
5	15	5.46(0.54)E-2	1.90E-02	4.20(0.92)E-02	1.93(0.31)E-1

Table D.1 – continued from previous page

Z	A	$\sigma$	EPAX	DIT+GEMINI	ISABEL+GEMINI
5	17	4.37(0.57)E-4	1.70E-04	-(-)	-(-)
6	15	7.23(0.79)E-1	1.14E+00	6.74(0.37)E-01	1.57(0.09)E+0
6	16	3.84(0.31)E-1	2.28E-01	1.13(0.05)E+00	1.11(0.08)E+0
6	17	4.62(0.38)E-2	3.45E-02	3.20(0.80)E-02	6.10(1.76)E-2
6	18	1.60(0.14)E-2	4.09E-03	1.40(0.53)E-02	2.03(1.02)E-2
6	19	5.13(0.54)E-4	3.92E-04	-(-)	-(-)
6	20	7.10(0.81)E-5	3.13E-05	-(-)	-(-)
7	18	3.79(0.41)E-1	3.77E-01	1.64(0.06)E+00	7.53(0.62)E-1
7	19	1.52(0.12)E-1	6.38E-02	3.04(0.25)E-01	1.88(0.31)E-1
7	20	1.76(0.16)E-2	8.52E-03	1.04(0.14)E-01	-(-)
7	21	3.27(0.28)E-3	9.26E-04	8.00(4.00)E-03	-(-)
7	22	1.42(0.15)E-4	8.41E-05	4.00(2.80)E-03	-(-)
7	23	5.56(0.75)E-6	6.53E-06	-(-)	-(-)
8	20	5.04(0.56)E-1	6.29E-01	1.57(0.06)E+00	2.12(0.10)E+0
8	21	1.13(0.10)E-1	1.20E-01	1.18(0.15)E-01	2.49(0.36)E-1
8	22	2.36(0.20)E-2	1.81E-02	1.16(0.15)E-01	5.60(1.69)E-2
8	23	1.12(0.12)E-3	2.23E-03	2.00E-03(2.00)	5.09(5.09)E-3
8	24	1.05(0.15)E-4	2.31E-04	-(-)	-(-)
9	23	2.21(0.24)E-1	2.28E-01	2.38(0.22)E-01	5.34(0.52)E-1
9	24	3.12(0.29)E-2	3.89E-02	2.60(0.72)E-02	9.16(2.16)E-2
9	25	4.63(0.57)E-3	5.47E-03	2.00(2.00)E-03	-(-)
9	26	5.42(0.94)E-4	6.50E-04	4.00(2.80)E-03	-(-)
9	27	3.22(0.48)E-5	6.66E-05	-(-)	-(-)
9	29	1.97(0.52)E-7	4.85E-07	-(-)	-(-)
10	25	1.45(1.07)E-1	4.36E-01	3.50(0.27)E-01	3.82(0.44)E-1
10	26	5.15(0.58)E-2	8.48E-02	1.86(0.19)E-01	1.63(0.29)E-1
10	27	1.19(0.65)E-3	1.36E-02	6.00(3.50)E-03	1.53(0.88)E-2
10	28	1.38(0.20)E-3	1.86E-03	-(-)	5.09(5.09)E-3
10	29	7.00(1.10)E-5	2.20E-04	-(-)	-(-)
10	30	1.08(0.20)E-5	2.30E-05	-(-)	-(-)
11	28	6.46(0.74)E-2	1.86E-01	8.60(1.31)E-02	1.07(0.23)E-1
11	29	2.19(0.25)E-2	3.43E-02	1.80(0.60)E-02	1.53(0.88)E-2
11	30	3.63(0.45)E-3	5.39E-03	2.00(2.00)E-03	-(-)
11	31	7.29(1.08)E-4	7.37E-04	-(-)	-(-)
11	32	5.71(0.97)E-5	8.96E-05	-(-)	-(-)
12	30	1.10(0.13)E-1	4.10E-01	4.94(0.31)E-01	2.39(0.35)E-1
12	31	2.55(0.30)E-2	8.69E-02	3.60(0.85)E-02	2.54(1.14)E-2
12	32	9.56(1.12)E-3	1.58E-02	2.80(0.75)E-02	2.54(1.14)E-2
12	33	8.77(1.14)E-4	2.51E-03	-(-)	-(-)
12	34	1.48(0.23)E-4	3.55E-04	-(-)	-(-)
13	34	1.48(0.18)E-2	4.64E-02	4.00(2.80)E-03	1.02(0.72)E-2
13	35	5.81(0.60)E-3	8.58E-03	-(-)	1.53(0.88)E-2
13	36	6.02(0.84)E-4	1.42E-03	-(-)	-(-)
13	37	1.51(0.16)E-4	2.15E-04	-(-)	-(-)

**Table D.1 – continued from previous page**

Z	A	$\sigma$	EPAX	DIT+GEMINI	ISABEL+GEMINI
13	38	1.08(0.29)E-5	3.01E-05	-(-)	-(-)
14	37	7.71(0.96)E-3	2.94E-02	8.00(4.00)E-03	1.02(0.72)E-2
14	40	5.94(1.23)E-5	1.77E-04	-(-)	-(-)

### D.1.2 Parallel Momentum Widths

Table D.2: Parallel momentum widths from the reaction of  $^{48}\text{Ca} + ^{181}\text{Ta}$ . All units are in MeV/c.

Z	A	Lab Frame					Projectile Frame
		$\sigma(P)$ (MeV/c)	$\sigma(E)$ (MeV)	$\sigma_{dE}$ MeV	${}^1\sigma_N(E)$ MeV	${}^1\sigma_N(P)$ (MeV/c)	
4	10	239(4)	112(9)	82.1(0.3)	76(13)	162(13)	143(17)
4	11	268(7)	124(9)	92.3(0.4)	82(14)	178(22)	158(26)
4	12	302(12)	138(9)	102.6(0.4)	92(14)	201(27)	179(32)
5	12	307(5)	146(9)	91.2(0.4)	114(12)	240(13)	211(16)
5	13	351(2)	163(9)	101.4(0.4)	128(12)	275(9)	244(12)
5	14	405(7)	187(10)	111.7(0.5)	150(13)	325(18)	288(22)
5	15	415(11)	191(10)	121.9(0.5)	147(13)	319(19)	284(23)
5	17	394(23)	177(8)	142.4(0.6)	104(14)	233(24)	208(28)
6	15	359(4)	167(8)	108.0(0.4)	128(11)	274(9)	242(12)
6	16	398(4)	184(9)	118.2(0.5)	141(11)	305(11)	271(14)
6	17	428(4)	197(9)	128.5(0.5)	149(12)	324(12)	288(15)
6	18	456(9)	209(9)	138.7(0.6)	156(12)	341(15)	303(18)
6	19	440(10)	201(8)	148.9(0.6)	135(12)	296(17)	263(21)
6	20	484(17)	219(8)	159.2(0.7)	150(12)	332(15)	297(18)
7	18	406(3)	187(8)	122.3(0.5)	142(10)	307(8)	273(10)
7	19	440(4)	201(8)	132.5(0.6)	151(11)	331(10)	294(13)
7	20	454(4)	209(8)	142.7(0.6)	152(11)	331(11)	294(14)
7	21	479(5)	218(8)	153.0(0.6)	155(11)	341(11)	304(14)
7	22	471(10)	216(8)	163.2(0.7)	142(12)	309(18)	275(22)
7	23	581(29)	263(10)	173.4(0.7)	198(13)	437(37)	390(42)
8	20	398(4)	183(7)	123.8(0.5)	135(9)	294(8)	261(10)
8	21	432(6)	198(7)	134.0(0.6)	146(10)	318(13)	283(16)
8	22	442(6)	203(7)	144.3(0.6)	142(10)	311(12)	276(14)
8	23	482(7)	220(8)	154.5(0.6)	157(11)	344(16)	306(19)
8	24	503(12)	230(8)	164.7(0.7)	161(12)	352(25)	313(29)
9	23	436(5)	199(6)	133.0(0.6)	148(9)	324(7)	288(9)

**Table D.2 – continued from previous page**

Z	A	$\sigma(P)$ (MeV/c)	$\sigma(E)$ (MeV)	$\sigma_{dE}$ MeV	${}^1\sigma_N(E)$ MeV	${}^1\sigma_N(P)$ (MeV/c)	$\sigma_N(P)$ (MeV/c)
9	24	442(8)	202(7)	143.2(0.6)	143(9)	312(13)	277(16)
9	25	446(10)	205(7)	153.5(0.6)	135(10)	295(16)	262(19)
9	26	501(16)	229(7)	163.7(0.7)	159(11)	350(24)	312(28)
9	27	511(13)	234(7)	173.9(0.7)	156(11)	341(25)	303(29)
10	25	418(81)	191(11)	129.5(0.5)	140(15)	307(116)	273(133)
10	26	452(6)	206(6)	139.7(0.6)	151(8)	332(9)	295(11)
10	27	468(19)	213(7)	149.9(0.6)	151(9)	333(21)	296(25)
10	28	490(21)	224(7)	160.2(0.7)	156(10)	342(24)	304(28)
10	29	503(22)	229(7)	170.4(0.7)	153(10)	336(27)	300(31)
10	30	476(20)	219(7)	180.6(0.8)	124(12)	269(30)	239(35)
11	28	436(7)	198(5)	133.6(0.6)	146(7)	322(8)	287(9)
11	29	460(8)	209(6)	143.9(0.6)	151(8)	334(10)	298(12)
11	30	471(15)	214(6)	154.1(0.6)	149(8)	328(17)	292(20)
11	31	463(22)	212(6)	164.3(0.7)	134(9)	293(22)	260(25)
11	32	524(29)	238(7)	174.6(0.7)	161(10)	356(34)	317(39)
12	30	409(7)	186(5)	125.1(0.5)	138(6)	304(6)	270(8)
12	31	433(9)	196(5)	135.3(0.6)	143(7)	314(9)	280(11)
12	32	473(10)	214(5)	145.5(0.6)	157(7)	347(11)	309(13)
12	33	497(19)	226(6)	155.7(0.6)	163(8)	360(17)	321(20)
12	34	456(24)	208(5)	166.0(0.7)	125(9)	274(19)	244(22)
13	34	440(12)	199(5)	134.4(0.6)	147(6)	325(11)	290(13)
13	35	535(2)	241(5)	144.6(0.6)	193(6)	428(1)	382(3)
13	36	544(29)	246(6)	154.9(0.6)	191(7)	423(20)	378(23)
13	37	472(6)	215(4)	165.1(0.7)	138(7)	303(3)	270(5)
13	38	491(54)	224(6)	175.3(0.7)	139(10)	306(45)	272(52)
14	37	422(14)	191(4)	131.0(0.5)	139(6)	307(9)	274(11)
14	40	417(40)	190(4)	161.7(0.7)	100(8)	220(21)	196(24)

### D.1.3 Parallel Momentum Transfer

Table D.3: Parallel momentum transferred from the reaction of  ${}^{48}\text{Ca} + {}^{181}\text{Ta}$ . All units are in MeV.

Z	A	Lab Frame		Projectile Frame	
		$\langle P \rangle$	${}^1\langle P_{corr} \rangle$	${}^1\langle P_{corr} \rangle$	${}^1\langle P' \rangle$
4	10	4922(11)	4986(40)	-28(52)	-34(63)

<sup>1</sup> Widths are corrected for the broadening due to energy straggling.

**Table D.3 – continued from previous page**

Z	A	<b>Lab Frame</b>		<b>Projectile Frame</b>	
		$\langle P \rangle$	${}^1\langle P^{corr} \rangle$	${}^1\langle P^{corr} \rangle$	${}^1\langle P' \rangle$
4	11	5343(20)	5409(45)	-98(59)	-107(65)
4	12	5724(26)	5793(51)	-202(65)	-204(66)
5	12	6023(13)	6120(43)	87(58)	88(58)
5	13	6356(10)	6458(48)	-57(64)	-53(59)
5	14	6771(20)	6876(53)	-132(71)	-114(61)
5	15	7238(23)	7343(59)	-163(77)	-131(62)
5	17	7939(30)	8051(69)	-425(90)	-302(64)
6	15	7352(11)	7498(51)	-25(69)	-20(56)
6	16	7748(15)	7898(56)	-115(75)	-87(57)
6	17	8215(16)	8365(60)	-146(81)	-104(58)
6	18	8646(21)	8798(66)	-207(88)	-139(59)
6	19	9085(26)	9238(71)	-261(94)	-166(60)
6	20	9457(22)	9614(75)	-373(100)	-226(61)
7	18	8702(11)	8905(58)	-112(80)	-75(53)
7	19	9112(15)	9319(62)	-190(86)	-121(55)
7	20	9640(18)	9845(67)	-169(92)	-102(55)
7	21	10006(18)	10215(72)	-285(98)	-164(56)
7	22	10573(32)	10779(77)	-230(104)	-126(57)
7	23	10873(64)	11086(85)	-402(113)	-212(60)
8	20	9672(12)	9936(60)	-88(84)	-53(51)
8	21	10085(22)	10353(65)	-163(91)	-94(52)
8	22	10574(20)	10842(69)	-174(96)	-96(53)
8	23	11024(28)	11293(74)	-219(102)	-115(54)
8	24	11512(46)	11781(80)	-231(110)	-116(55)
9	23	11010(13)	11350(66)	-169(95)	-89(50)
9	24	11493(25)	11833(71)	-186(101)	-94(51)
9	25	12022(31)	12360(76)	-163(107)	-79(52)
9	26	12404(48)	12747(82)	-264(114)	-123(53)
9	27	12918(53)	13260(87)	-255(120)	-114(54)
9	29	14024(77)	14359(99)	-170(134)	-71(56)
10	25	11964(227)	12382(147)	-143(181)	-69(88)
10	26	12367(17)	12790(73)	-226(105)	-105(49)
10	27	12865(45)	13287(38)	-230(113)	-103(51)
10	28	13379(52)	13800(85)	-221(119)	-95(52)
10	29	13835(60)	14257(90)	-260(126)	-109(52)
10	30	14486(72)	14899(46)	-136(133)	-55(53)
11	28	13324(16)	13834(75)	-191(110)	-83(48)
11	29	13760(21)	14273(79)	-246(116)	-103(48)
11	30	14287(39)	14797(85)	-226(122)	-91(49)
11	31	14853(53)	15358(91)	-174(129)	-68(50)
11	32	15180(83)	15695(101)	-320(140)	-121(53)
12	30	14286(15)	14890(78)	-144(116)	-58(47)
12	31	14711(22)	15320(82)	-208(121)	-81(47)

**Table D.3 – continued from previous page**

Z	A	Lab Frame		Projectile Frame	
		$\langle P \rangle$	${}^1\langle P_{corr} \rangle$	${}^1\langle P_{corr} \rangle$	${}^1\langle P' \rangle$
12	32	15112(27)	15726(86)	-292(127)	-110(48)
12	33	15655(44)	16266(92)	-259(133)	-95(49)
12	34	16242(49)	16845(96)	-190(138)	-68(49)
13	34	16075(29)	16792(89)	-237(132)	-84(47)
13	35	16486(2)	17208(91)	-313(135)	-108(47)
13	36	16993(55)	17713(100)	-310(145)	-104(49)
13	37	17651(77)	18359(46)	-183(143)	-60(47)
13	38	18125(133)	18834(128)	-206(175)	-66(56)
14	37	17464(26)	18296(95)	-239(142)	-78(46)
14	40	19119(64)	19935(110)	-121(160)	-36(48)

#### D.1.4 Asymmetric factor

Table D.4: The asymmetric term to the parallel momentum widths from the reaction of  ${}^{48}\text{Ca} + {}^{181}\text{Ta}$ .

Z	A	a	Z	A	a
4	10	-(-)	10	27	-(-)
4	11	692.48(212.85)	10	28	462.74(369.91)
4	12	833.17(285.72)	10	29	-(-)
5	12	-(-)	10	30	-(-)
5	13	-(-)	11	28	-(-)
5	14	273.31(121.46)	11	29	-(-)
5	15	644.26(152.54)	11	30	603.33(221.82)
5	17	659.97(259.02)	11	31	474.98(273.25)
6	15	-(-)	11	32	-(-)
6	16	229.75(76.76)	12	30	-(-)
6	17	413.53(95.63)	12	31	-(-)
6	18	461.84(112.15)	12	32	-(-)
6	19	425.42(183.43)	12	33	-(-)
6	20	-(-)	12	34	-(-)
7	18	-(-)	13	34	-(-)
7	19	108.03(58.66)	13	35	-(-)
7	20	542.68(142.68)	13	36	-(-)
7	21	243.73(100.53)	13	37	-(-)
7	22	419.63(227.11)	13	38	-(-)

<sup>1</sup>Corrected for the broadening due to energy straggling.

**Table D.4 – continued from previous page**

Z	A	a	Z	A	a
7	23	-(-)	14	37	-(-)
8	20	-(-)	14	40	-(-)
8	21	252.5(105.24)	13	36	-(-)
8	22	301.6(87.66)	14	33	-(-)
8	23	426.79(234.15)	14	34	292.28(93.83)
8	24	354.74(347.35)	14	35	341.01(191.36)
9	23	-(-)	14	36	200.69(382.35)
9	24	267.42(109.99)	15	36	562.19(169.6)
9	25	751.19(315.18)	15	37	205(78.43)
9	26	632.87(454.19)	15	38	-(-)
9	27	-(-)	16	38	-(-)
9	29	-(-)	16	41	-(-)
9	31	-(-)	15	37	700.16(202.09)
10	25	-(-)	16	41	-(-)
10	26	-(-)			

### D.1.5 Angular Transmission

Table D.5: The angular transmission of fragments in percent as predicted by LISE.

Z	A	Transmission	Z	A	Transmission
4	10	0.22	9	26	0.62
4	11	0.25	9	27	0.65
4	12	0.27	9	29	0.68
5	12	0.27	9	31	0.68
5	13	0.29	10	25	0.60
5	14	0.33	10	26	0.63
5	15	0.36	10	27	0.65
5	17	0.41	10	28	0.68
6	15	0.35	10	29	0.70
6	16	0.38	10	30	0.71
6	17	0.41	11	28	0.68
6	18	0.43	11	29	0.70
6	19	0.46	11	30	0.71
6	20	0.49	11	31	0.72
7	18	0.43	11	32	0.72
7	19	0.46	12	30	0.71
7	20	0.49	12	31	0.73
7	21	0.51	12	32	0.75
7	22	0.53	12	33	0.77

**Table D.5 – continued from previous page**

Z	A	Transmission	Z	A	Transmission
7	23	0.55	12	34	0.78
8	20	0.48	13	34	0.78
8	21	0.51	13	35	0.80
8	22	0.53	13	36	0.81
8	23	0.55	13	37	0.82
8	24	0.58	13	38	0.82
9	23	0.55	14	37	0.83
9	24	0.58	14	40	0.85
9	25	0.60			

# Bibliography

- [1] F. Marti, P. Miller, D. Poe, M. Steiner, J. Stetson, and X.Y. Wu. In P. Lucas and S. Webber, editors, *PAC2001 Proceedings of the 2001 Particle Accelerator Conference*, page 2557. (IEEE Operations Center, 2001), 2001. 1
- [2] Z. Dlouhý, J. C. Angélique, R. Anne, G. Auger, D. Baiborodin, C. Borcea, E. Caurier, A. Gillibert, S. Grevy, D. Guillemaud-Mueller, A. S. Lalleman, M. Lewitowicz, S. M. Lukyanov, W. Mittig, J. Mrázek, A. C. Mueller, F. Nowacki, F. de Oliveira, N. Orr, R. D. Page, Yu. E. Penionzhkevich, F. Pougheon, A. T. Reed, Z. Ren, D. Ridikas, P. Roussel-Chomaz, M. G. Saint-Laurent, H. Sakurai, F. Sarazin, H. Savajols, O. Sorlin, O. Tarasov, A. de Vismes, and J. Winfield. *Nucl. Phys. A*, **702**:189, 2002. 1
- [3] M. Theoennessen. *Rep. Prog. Phys.*, **67**:1187, 2004. and reference therein. 1, 2, 3, 34, 35
- [4] D. Guillemaud-Mueller, Yu.E. Penionzhkevich, R. Anne, A.G. Artukh, D. Bazin, V. Borrel, C. Détraz, D. Guerreia, B.A. Gvozdev, H.C. Jacmart, D.X. Jiang, A.M. Kalinin, V.V. Kamanin, V.B. Kutner, M. Lewitowicz, S.M. Lukyanov, A.C. Mueller, N. Hoai Chau, F. Pougheon, A. Pichard, M.G. Saint-Laurent, and W.D. Schmidt-Ott. *Z. Phys. A*, **332**:189, 1989. 1, 33, 34
- [5] D. Bazin, W. Benenson, B.A. Brown, J. Brown, B. Davids, M. Fauerbach, P.G. Hansen, P. Mantica, D.J. Morrissey, C.F. Powell, B.M. Sherrill, and M. Steiner. Probing the halo structure of  $^{19,17,15}\text{C}$  and  $^{14}\text{B}$ . *Phys. Rev. C*, **57**, 1998. 1
- [6] K. Süümmerer, W. Brüchle, D.J. Morrissey, M. Schädel, B. Szweryn, and Y. Weifan. *Phys. Rev. C*, **42**:2546, 1990. 2, 6, 8, 9, 75
- [7] K. Süümmerer and B. Blank. *Phys. Rev. C*, **61**:034607, 2000. 2, 6, 8, 9, 12, 13, 75
- [8] D. Bazin, O.B. Tarasov, M. Lewitowicz, and O. Sorlin. *Nucl. Inst. and Meth. A*, **482**:307, 2001. 2, 6, 17, 38, 56
- [9] M. Hencheck, R.N. Boyd, M. Hellström, D.J. Morrissey, M.J. Balbes, F.R. Chloupek, M. Fauerbach, C.A. Mitchell, R. Pfaff, C.F. Powell, G. Raimann, B.M. Sherrill, M. Steiner, J. Vandegriff, and S.J. Yennello. *Phys. Rev. C*, **50**:2219, 1994. 3

- [10] H. Sakurai, S.M. Lukyanov, M. Notani, N. Aoi, D. Beaumel, N. Fukuda, M. Hirai, E. Ideguchi, N. Imai, M. Ishihara, H. Iwasaki, T. Kubo, K. Kusaka, H. Kumagai, T. Nakamura, H. Ogawa, Yu.E. Penionzhkevich, T. Teranishi, Y.X. Watanabe, K. Yoneda, and A. Yoshida. *Phys. Lett. B*, **448**:180, 1999. 3, 33, 83
- [11] S.M. Lukyanov, Yu.E. Penionzhkevich, R. Astabatyan, S. Lovastov, Yu. Sobolev, D. Guillemaud-Mueller, G. Faivre, F. Ibrahim, A.C. Mueller, F. Pougheon, O. Perru, O. Sorlin, I. Matea, R. Anne, C. Cauvin, R. Hue, G. Oliveira, Santos, D. Verney, Z. Dlouhý, J. Mrázek, D. Baiborodin, F. Negeita, C. Borcea, and A. Buta. *J. Phys. G*, **28**:L41, 2002. 3, 83
- [12] H. Geissel, P. Armbruster, K.H. Behr, A. Brnle, K. Burkard, M. Chen, H. Folger, B. Franczak, H. Keller, O. Klepper, B. Langenbeck, F. Nickel, E. Pfeng, M. Pfützner, E. Roeckl, K. Rykaczewski, I. Schall, D. Schardt, C. Scheidenberger, K.-H. Schmidt, A. Schröter, T. Schwab, K. Smmerer, M. Weber, and G. Mnzenberg. *Nucl. Instr. and Meth. B*, **70**:286, 1992. 3
- [13] K.S. Krane. *Introductory Nuclear Physics*. John Wiley & Sons, Inc., 1987. 3, 27
- [14] Y.P. Viyogi, T.J.M. Symons, P. Doll, D.E. Greiner and H.H. Heckman, D.L. Hendrie, P.J. Lindstrom, J. Mahoney, D.K. Scott, K. Van Bibber, G.D. Westfall, H. Wienman, H.J. Crawford, C. McParland, and C.K. Celbke. *Phys. Rev. Lett.*, **42**:33, 1979. 4
- [15] J. Gosset, H.H. Gutbrod, W.G. Meyer, A.M. Poskanzer, A. Sandoval, R. Stock, and G.D. Westfall. *Phys. Rev. C*, **16**:629, 1977. 4, 14
- [16] H. Feshbach and K. Huang. *Phys. Lett. B*, **47**:300, 1973. 5, 63
- [17] J.D. Bowman, W.J. Swiatecki, and C.E. Tsang. Lawrence Berkeley Laboratory Report No. LBL-2908, 1973 (unpublished). 5, 9, 14
- [18] L.F. Oliveira, R. Donangelo, and J.O. Rasmussen. *Phys. Rev. C*, **19**:826, 1979. 5, 9, 16
- [19] Y. Yariv and Z. Fraenkel. *Phys. Rev. C*, **20**:2227, 1979. 5, 9, 17, 20, 71
- [20] Y. Yariv and Z. Fraenkel. *Phys. Rev. C*, **24**:488, 1981. 5, 9, 17, 20, 71
- [21] J. Cugnon. *Nucl. Phys. A*, **387**:191c, 1982. 5
- [22] M. Lefort and C. Ngo. *Ann. Phys. (Paris)*, **3**:5, 1978. 5
- [23] L. Tassan-Got and C. Stépan. *Nucl. Phys. A*, **524**:121, 1991. 5, 9, 24, 71
- [24] J.A. Winger, B.M. Sherrill, and D.J. Morrissey. *Nucl. Instr. and Meth. B*, **70**:380, 1992. 6

- [25] K. Chen, Z. Fraenkel, G. Friedlander, J.R Grover, J.M. Miller, and Y. Shimamoto. *Phys. Rev.*, **166**:949, 1968. 6, 9, 17
- [26] C. Wong and K. Van Bibber. *Phys. Rev. C*, **25**:2990, 1982. 6
- [27] B.G. Harvey. *Nucl. Phys. A*, **444**:498, 1985. 7
- [28] <http://www.nscl.msu.edu/aud/exp/propexp/beamlist.php>. 7
- [29] D. Guerreau. *Nucl. Phys. A*, **447**:37c, 1985. 7, 37
- [30] G.D. Westfall, P.J. Johansen, A.M. Poskanzer, W.G. Meyer, H.H. Gutbrod, A. Sandoval, and R. Stock. *Phys. Rev. Lett.*, **37**:1202, 1976. 8
- [31] W.U. Schröder and J.R. Huizenga. *Annu. Rev. Nucl. Part. Sci.*, **27**:465, 1977. 8
- [32] B. Grabez. *Phys. Rev. C*, **64**:057601, 2001. 8
- [33] J.-J Gaimard and K.-H. Schmidt. *Nucl. Phys. A*, **531**:709, 1991. 9, 17
- [34] D.J. Morrissey, W.R. Marsh, R.J. Otto, W. Loveland, and G.T. Seaborg. *Phys. Rev. C*, **18**:1267, 1978. 9, 14, 15
- [35] G. Rudstam. *Z. Naturforsch*, **21**:1027, 1966. 10
- [36] G. D. Westfall, T.J.M. Symons, D.E. Greiner, H.H. Heckman, P.J. Lindstrom, J. Mahoney, A.C. Shotter, and D.K. Scott. *Phys. Rev. Lett.*, **43**:1859, 1973. 13
- [37] M. Weber, C. Donzaud, J.P. Dufour, H. Geissel, A. Grewe, D. Guillemaud-Mueller, H. Keller, M. Lewitowicz, A. Magel, A.C. Mueller, G. Müzenberg, F. Nickel, M. Pfützner, A. Piechaczek, M. Pravikoff, E. Roeckl, K. Rykaczewski, M.G. Saint-Laurent, I. Shall, C. Stéphan, K. Sümmeler, L. Tassan-Got, D.J. Vieira, and B. Voss. *Nucl. Phys. A*, **578**:659, 1994. 13, 65
- [38] R. Serber. *Phys. Rev.*, **72**:1114, 1947. 14, 67
- [39] D.J. Morrissey, L.F. Oliveira, J.O. Rasmussen, G.T. Seaborg, Y. Yariv, and Z. Fraenkel. *Phys. Rev. Lett.*, **43**:1139, 1979. 16, 20, 29, 30
- [40] J.W. Wilson, L.W. Townsend, and F.F. Badavi. *Nucl. Instr. and Meth. B*, **18**:225, 1987. 17
- [41] R. Charity. *Nucl. Phys. A*, **483**:391, 1988. 23, 27, 71
- [42] S.K. Samaddar, J.N. De, and K. Krishan. *Phys. Rev. C*, **31**:1053, 1985. 24
- [43] G.A. Souliotis, M. Veselsky, G. Chubarian, L. Trache, A. Keksis, E. Martin, D.V. Shetty, and S.J. Yennello. *Phys. Rev. Lett.*, **91**:022701, 2003. 26
- [44] H. C. Ohanian. *Principles of Quantum Mechanics*. Prentice Hall, 1990. 26
- [45] F. Pühlhofer. *Nucl. Phys. A*, **280**:267, 1977. 27

- [46] A. Gavron. *Phys. Rev. C*, **21**:230, 1980. 27
- [47] Charles L. Critchfield and Sophie Oleksa. *Phys. Rev.*, **82**:243, 1951. 27
- [48] S. I. Al-Quraishi, S. M. Grimes, T. N. Massey, and D. A. Resler. *Phys. Rev. C*, **63**:065803, 2001. 27
- [49] H. A. Bethe. *Phys. Rev.*, **50**:332, 1936. 27
- [50] A. S. Iljinov, M. V. MebelN. Bianchi, E. De Sanctis, C. Guaraldo, V. Lucherini, V. Muccifora, E. Polli, A. R. Reolon, and P. Rossi. *Nucl. Phys. A*, **543**:517, 1992. 27
- [51] J. Toke and W. J. Swiatecki. *Nucl. Phys. A*, **374**:141, 1981. 28
- [52] P.G. Hansen and B.M. Sherrill. *Nucl. Phys. A*, **693**:133, 2001. 31
- [53] G.A. Lalazissis, D. Vretenar, W. Pöschl, and P. Ring. *Phys. Lett. B*, **379**:13, 1996. 31
- [54] G.Audi, A.H.Wapstra, and C.Thibault. *Nucl. Phys. A*, **729**:337, 2003. 32, 33, 36
- [55] T. Tachibana, M. Uno, and M. Yamada S. Yamada. *At. Data and Nucl. Data Tables*, **39**:251, 1988. 34
- [56] B.A Brown and W.A. Richter. *Phys. Rev. C*, **72**:057301, 2005. 32
- [57] M. Fauerbach. *Study of Neutron Rich Nuclei*. PhD thesis, Michigan State University, 1997. 33
- [58] A. Schiller, T. Baumann, J. Dietrich, S. Kaiser, W. Peters, and M. Thoennessen. *Phys. Rev. C*, **72**:037601, 2005. 33
- [59] H. Sakurai, S.M. Lukyanov, M. Notani, N. Aoi, D. Beaumel, N. Fukuda, M. Hirai, E. Ideguchi, N. imai, M. Ishihara, H. Iwasaki, T. Kubo, K. Kusaka, H. Kumagai, T. Nakamura, H. Ogawa, Yu.E. Penionzhkevich, T. Teranishi, Y.X. Watanabe, K. Yoneda, and A. Yoshida. In B.M. Sherrill, D.J. Morrissey, and C. N. Davids, editors, *ENAM98:Exotic Nuclei and Atomic Masses*, pages 233–238. The American Institute of Physics, 1998. 33
- [60] O Tarasov, R. Allatt, J.C. Angélique, R. Anne, C. Borcea, Z. Dlouhy, C. Donzaud, S.Grévy, D. Guillemaud-Mueller, M. lewitowicz, S. Lukyanov, A.C. Mueller, F. Nowacki, Yu. Oganessian, N.A. Orr, A.N. Ostrowski, R.D. Page, Yu. Penionzhkevich, F. Pougheon, A. Reed, M.G. Saint-Laurent, W. Schwab, E. Sokol, O. Sorlin, W. Trinder, and J.S. Winfield. *Phys. Lett. B*, **409**:64, 1997. 33
- [61] D. Bazin, B.A. Brown, J. Brown, M. Fauerbach, M. Hellström, S.E. Hirzebruch, J.H. Kelley, R.A. Kryger, D.J. Morrissey, R. Pfaff, C.F. Powell, B.M. Sherrill, and M. Thoennessen. *Phys. Rev. Lett.*, **74**:18, 1995. 33

- [62] M. Langevin, E. Quiniou, M. Bernas, J. Galin, J. C. Jacmart, F. Naulin, F. PougheonR. Anne, C. Dtraz, D. Guerreau, D. Guillemaud-Mueller, and A. C. Mueller. *Phys. Lett. B*, **150**:71, 1985. 33
- [63] Y. Utsuno, T. Otsuka, T. Mizusaki, and M. Honma. *Phys. Rev. C*, **64**:011301(R), 2001. 33
- [64] P. Möller, J.R. Nix, and K. L. Kratz. *At. Data and Nucl. Data Tables*, **66**:131, 1997. 34, 35, 36
- [65] B.A. Brown. *Prog. Part. Nucl. Phys*, **47**:517, 2001. 34, 35, 36
- [66] Subcommittee on Performance Measures. Report submitted by the subcommittee on performance measures. <http://www.sc.doe.gov/np/nsac/nsac.html>, 2003. 35
- [67] V. Borrel, B. Gatty, D. Guerrau, J. Galin, and D. Jacquet. *Z. Phys. A*, **324**, 1986. 37
- [68] D.J. Morrissey, B.M. Sherrill, M. Steiner, A. Stolz, and I. Wiedenhover. *Nucl. Instr. and Meth. B*, **204**:90, 2003. 38
- [69] C. Scheidenberger and H. Geissel. *Nucl. Instr. and Meth. B*, **135**:25, 1998. 44, 60
- [70] H. Geissel and C. Scheidenberger. *Nucl. Instr. and Meth. B*, **136**:114, 1998. 44, 60
- [71] <http://www-linux.gsi.de/~weick/atima/>. 44
- [72] *Nucl. Instr. and Meth. B*, **126**:284, 1997. 50
- [73] O. Tarasov. *Nucl. Phys. A*, **734**:536, 2004. 56
- [74] M. Notani. *Projectile Fragmentation Reactions and Production of Nuclei near the Neutron Drip-line*. PhD thesis, University of Tokyo, 2000. 56, 72, 73, 74
- [75] M. Mocko. private communications. 56, 72, 73, 74, 79
- [76] R. Pfaff. *Projectile Fragmentation of Krypton Isotopes at Intermediate Energies*. PhD thesis, Michigan State University, 1996. 57
- [77] G.F. Knoll. *Radiation Detection and Measurement*. John Wiley & Sons, Inc., third edition edition, 2000. 58
- [78] N. Tsoulfanidis. *Measurement and Detection of Radiation*. Taylor and Francis, second edition, 1995. 59
- [79] R.D. Evens. *The Atomic Nucleus*. Robert E. Krieger Publishing Co., 1982. 59
- [80] H.A. Bethe. *Ann. Physik*, **5**:325, 1930. 60

- [81] F. Bloch. *Ann. Physik*, **77**:287, 1932. 60
- [82] J. Ziegler, J. Biersack, and U. Littmark. In *The Stopping and Ranges of Ions in Matter*. Pergamon Press, New York, 1985. 60
- [83] F. Hubert, R. Bimbot, and H. Gauvin. *At. Data and Nucl. Data Tables*, **46**:1, 1990. 60, 61
- [84] J.P. Dufour, R. Del Moral, H. Emmermann, F. Hubert, D. Jean, C. Poinot, M.S. Pravikoff, A. Fleury, H. Delagrange, and K.-H. Schmidt. *Nucl. Instr. and Meth. A*, **248**:267, 1986. 60, 61
- [85] H.H. Heckman et al. In G. Tibell, editor, *High Energy Physics and Nuclear Structure, Proceedings of the Fifth International Conference on High-Energy Physics and Nuclear Structure*, pages LBL-2052 (unpublished). North-Holland, Amsterdam/American Elsevier, New York, 1973. 63
- [86] A. S. Goldhaber. *Phys. Lett. B*, **53**:306, 1974. 64
- [87] E.J. Moniz, I. Sick, R.R. Whitney, J.R. Ficenec, R.D. Kephart, and W. P. Trower. *Phys. Rev. Lett.*, **26**:445, 1971. 64
- [88] W.A. Friedman. *Phys. Rev. C*, **27**:569, 1983. 65, 66
- [89] G. Bertsch. *Phys. Rev. Lett.*, **46**:472, 1981. 65
- [90] M.J. Murphy and R.G. Stokstad. *Phys. Rev. C*, **28**:428, 1983. 65
- [91] B.G. Harvey. *Phys. Rev. Lett.*, **47**:454, 1981. 65
- [92] C. Egelhaaf, G. Bohlen, H. Fuchs, A. Gamp, H. Homeyer, and H. Kluge. *Phys. Rev. Lett.*, **46**:813, 1981. 65
- [93] D.E. Greiner, P.J. Lindstrom, H.H. Heckman, B. Cork, and F.S. Bieser. *Phys. Rev. Lett.*, **35**:152, 1975. 65
- [94] F. Rami, J.P. Coffin, G. Guillaume, B. Heusch, P. Wagner, A. Fahli, and P. Fintz. *Nucl. Phys. A*, **444**:325, 1985. 65
- [95] C. Vincent-Donnet, M. Stern, E. Gerlic, M.T. Magda, B. Chambon, A. Chevarier, N. Chevarier, B. Drain, C. Pastor, A. Giorni, D. Heuer, A. Lleres, and J.B. Viano. *J. Phys. G*, **22**:397, 1996. 65
- [96] G. Farès, R. Bimbot, S. Hachem, M. Mirea, R. Anne, T. Benfoughal, C. Cabot, F. Clapier, P. Delbourgo-Salvador, T. Ethvignot, A. Lefebvre, M. Lewitowicz, P. Roussel-Chomaz, M.G. Saint-Laurent, J.E. Sauvestre, J.L. Sida, and Yang Yong Feng. *Eur. Phys. J. A*, **19**:105, 2002. 65
- [97] C. Stéphan, L. Tassan-Got, D. Bachelier, C.O. Bacri, R. Rimbot, B. Borderie, J.L. Boyard, F. Clapier, C. Donzaud, T. Hennino, M.F. Rivet, P. Roussel, D. Bazin, C. Grunber, D. Dissier, and B. Lott. *Phys. Lett. B*, **262**:6, 1991. 65

- [98] J. Mougey, R. Ost, M. Buenerd, A. J. Cole, C. Guet, D. Lebrun, J. M. Loiseaux, P. Martin, M. Maurel, E. Monnand, H. Nifenecker, P. Perrin, J. Pinston, C. Ristori, P. de Saintignon, F. Schussler, L. Carlén, B. Jakobsson A. Oskarsson, I. Otterlund, B. Schroder H. A. Gustafsson, T. Johansson, H. Ryde, J. P. Bondorf, O. B. Nielsen, and G. Tibell. *Phys. Lett. B*, **105**:25, 1981. 65
- [99] R. Pfaff, D.J. Morrissey, M. Fauerbach, M. Hellström, J.H. Kelley, R.A. Kryger, B.M. Sherrill, M. Steiner, J.S. Winfield, J.A. Winger, S.J. Yennello, and B.M. Young. *Phys. Rev. C*, **51**:1348, 1995. 65
- [100] D.J. Morrissey. *Phys. Rev. C*, **39**:460, 1989. 66
- [101] A. Abul-magd, J. Hüfner, and B. Schürmann. *Phys. Lett. B*, **60**:327, 1976. 68
- [102] J. B. Cumming, P. E. Haustein, and H. C. Hseuh. *Phys. Rev. C*, **24**:2162, 1981. 68
- [103] M.V. Ricciardi, P. Armbruster, J. Benlliure, M. Bernas, A. Boudard, S. Czajkowski, T. Enqvist, A. Kelić, S. Leray, R. Legrain, B. Mustapha, J. Pereira, F. Rejmund, K.-H. Schmidt, C. Stéphan, L. Tassan-Got, C. Volant, and O. Yordanov. *Phys. Rev. C*, **73**:041607, 2006. 69
- [104] L. Shi, P. Danielewicz, and R. Lacey. *Phys. Rev. C*, **64**:034601, 2001. 70
- [105] M. Notani, H. Sakurai, N. Aor, Y. Yanagisawa, A. Saito, N. Imai, T. Gomi, M. Miura, S. Michimasa, H. Iwasaki, N. Fukada, M. Ishihara, T. Kubo, S. Kubono, H. Kumagai, S.M. Lukyanov, T. Motobayashi, T.K. Onishi, Yu.E. Penionzhkevich, S. Shimoura, T. Teranishi, K. Ue, V. Uglyumov, and A. Yoshida. *Phys. Lett. B*, **542**:49, 2002. 70, 83
- [106] *Genie 2000 Customization Tools Manual*, 2000. 74, 92
- [107] G. Audi and A.H. Wapstra. *Nucl. Phys. A*, **565**:1, 1993. 82